# Simultaneous measurement of soil electrical conductivity and dielectric permittivity using high-frequency electromagnetic induction

**Špikić, Dorijan**

**Doctoral thesis / Disertacija**

**2024**

*Degree Grantor / Ustanova koja je dodijelila akademski / stručni stupanj:* **University of Zagreb, Faculty of Electrical Engineering and Computing / Sveučilište u Zagrebu, Fakultet elektrotehnike i računarstva**

*Permanent link / Trajna poveznica:* https://urn.nsk.hr/urn:nbn:hr:168:471739

*Rights / Prava:* In copyright/Zaštićeno autorskim pravom.

*Download date / Datum preuzimanja:* **2024-12-05**

University of Zagreb

FACULTY OF ELECTRICAL ENGINEERING AND COMPUTING

Dorijan Špikić

# SIMULTANEOUS MEASUREMENT OF SOIL ELECTRICAL CONDUCTIVITY AND DIELECTRIC PERMITTIVITY USING HIGH-FREQUENCY ELECTROMAGNETIC INDUCTION

DOCTORAL THESIS

Zagreb, 2024

University of Zagreb

FACULTY OF ELECTRICAL ENGINEERING AND COMPUTING

Dorijan Špikić

# SIMULTANEOUS MEASUREMENT OF SOIL ELECTRICAL CONDUCTIVITY AND DIELECTRIC PERMITTIVITY USING HIGH-FREQUENCY ELECTROMAGNETIC INDUCTION

DOCTORAL THESIS

Supervisor: Professor Darko Vasić, Ph.D.

Zagreb, 2024

Sveučilište u Zagrebu

FAKULTET ELEKTROTEHNIKE I RAČUNARSTVA

Dorijan Špikić

# ISTOVREMENO MJERENJE ELEKTRIČNE VODLJIVOSTI I DIELEKTRIČNE PERMITIVNOSTI TLA PRIMJENOM VISOKOFREKVENCIJSKE ELEKTROMAGNETSKE INDUKCIJE

DOKTORSKI RAD

Mentor: prof. dr. sc. Darko Vasić

Zagreb, 2024.

Supervisor: Professor Darko Vasić, Ph.D.

The doctoral thesis has 132 pages.

Doctoral thesis number: _____

# About the supervisor

**Darko Vasić** is a full professor at the University of Zagreb, Faculty of Electrical Engineering and Computing in Zagreb, Croatia in the field of electronic instrumentation and measurement. He earned his Ph.D. in electrical engineering from the University of Zagreb in 2010. He was awarded for his doctaral thesis with the Silver Plaque Josip Lončar and the Končar award. Darko Vasić has over 20 years of research, educational and industrial experience in electromagnetic modelling and sensorics, electronic instrumentation and electronic systems. His research interests primarily focus on eddy current non-destructive testing and soil sensing. He has coauthored more than 60 journal and conference papers. He serves as co-editor in chief of the journal Automatika and contributes as a technical reviewer for several high-ranking international journals. He was a program committee chair for the IEEE International Instrumentation Measurement Technology Conference in 2020, and acted as a guest editor for a special issue of IEEE Transactions on Instrumentation and Measurement. He was a principal investigator of eight research projects funded by EU and national funds, and industry collaborations. He participated in the development of commercial industrial systems for geophysical measurements, and automated systems for eddy current inspection in nuclear power plants.

# O mentoru

**Darko Vasić** je redoviti profesor Sveučilišta u Zagrebu Fakulteta elektrotehnike i računarstva u području elektroničke instrumentacije i mjerenja. Doktorirao je elektrotehniku na Sveučilištu u Zagrebu 2010. Za rezultate doktorskog rada nagrađen je srebrenom plaketom "Josip Lončar" FER-a i nagradom "Končar". Darko Vasić ima preko 20 godina istraživačkog, obrazovnog i industrijskog iskustva u području elektromagnetskog modeliranja i senzorike, te elektroničke instrumentacije i elektroničkih sustava. Njegovi istraživački interesi su posebno usmjereni na nerazorno ispitivanje vrtložnim strujama i ispitivanje tla. Koautor je više od 60 radova u časopisima i konferencijama. Djeluje kao glavni suurednik časopisa Automatika i recenzent za nekoliko uglednih međunarodnih časopisa. Bio je predsjednik programskog odbora za IEEE International Instrumentation Measurement Technology Conference 2020. i gost urednik za posebno izdanje IEEE Transactions on Instrumentation and Measurement. Bio je voditelj osam istraživačkih projekata financiranih iz EU i nacionalnih fondova te projekata u suradnji s industrijom. Sudjelovao je u razvoju komercijalnih industrijskih sustava za geofizička mjerenja, te automatiziranih sustava za inspekciju vrtložnim strujama u nuklearnim elektranama.

# Acknowledgements

*Firstly, I would like to thank my supervisor, Darko Vasić, for giving me this opportunity, for his guidance and encouragement through my doctoral journey, extensive discussions about everything research-related or unrelated, and for steering me in the right direction and helping me become an independent researcher.*

*Thank you, Professor Vedran Bilas, Dr. Michael O'Toole, and Professor Ratko Magjarević, for being on my thesis committee.*

*I want to thank my colleagues from ZESOI, especially Davorin Ambruš for his invaluable bits of engineering wisdom, Marijan Kuri for his help with the mechanical construction of the experimental setup, and Matija Švraka for helping me with numerical simulations.*

*Thanks to my former and current colleagues in D-136, Marko, Marko, Ivan, Fran, Dinko, Dora, and Niko, for making the work environment enjoyable. Thank you, Tin, Ivan and Kristijan for our discussions during lunch.*

*Thanks to Ivana for always listening to my problems and giving me good advice.*

*A big thanks to my friends, Andrej and Bruno, for always being there for me and reminding me to have fun in life. Thanks to Matej, Tin, Nikola, Ana, Matea, Dajana, Tena, and Anja for being part of my life.*

*Thanks to my family, grandparents baka Ruža, baka Franca, and deda Ugo for believing in me, and my brother Matija and sister-in-law Ana for always cheering for me.*

*Most importantly, I am grateful to my parents, Damir and Vesna, who supported me through each stage of my life; this wouldn't have been possible without them.*

# Summary

Soil is a heterogeneous medium consisting of solid particles, liquid, air, and organic matter with a pronounced variability over the area. Mapping a within-field variability of soil properties provides valuable information for soil management in precision agriculture applications. The soil electromagnetic parameters (electrical conductivity, magnetic permeability, and dielectric permittivity) depend on the physical and chemical properties of the soil, such as water content or salinity, and can be related through empirical and theoretical models. Proximal soil sensing techniques are well suited for mapping within-field variability as they provide high temporal and spatial resolution of soil data. The electromagnetic modalities used are direct current resistivity measurement, capacitively coupled resistivity measurement, electromagnetic induction, and ground penetrating radar. These modalities are complementary as their sensitivity to electromagnetic parameters differs due to different frequency ranges. This doctoral thesis researches high-frequency electromagnetic induction (HFEMI) sensing modality, operating in the frequency range from 3 MHz to 30 MHz through the analytical model, finite element method analysis, and experimental verification. The main hypothesis is that the modality is sensitive to electrical conductivity and dielectric permittivity in this frequency range. It is possible to sense both electromagnetic effective parameters of the soil simultaneously using the portable sensor design, and this was shown through analytical and laboratory analysis.

The analytical model derived from Maxwell's equations for a two-layer homogeneous medium shows that the sensitivity to conductivity and permittivity increases with the frequency, while the sensitivity to magnetic susceptibility is unaffected by frequency increase. The proposed HFEMI soil sensor consists of an electrostatically shielded printed circuit board transmitter and receiver coil, battery-powered proprietary electronics, and a commercial vector network analyzer. The electrostatic patterned PCB shields were used on both sides of each coil

to minimize the capacitive coupling between the coils and through the medium. A method to evaluate the effectiveness of the shield spacing and patterns was derived, and proper shielding was chosen accordingly by comparing measured sensor response in the air with the FEM analysis of the unshielded coils. The proposed sensor geometry has separated the transmitter and receiver coils, which are mutually perpendicular to control the primary inductive coupling.

The HFEMI soil sensor was evaluated in the laboratory above the container filled with 61 l of deionized water, to which salt or sucrose was added to change electrical conductivity and dielectric permittivity. The results agreed quantitatively with the FEM model, demonstrating the possibility of simultaneous determination of electrical conductivity and dielectric permittivity at a single frequency. The measurement results of field tests with the soil irrigated with deionized and saline water showed that the sensor response is in accordance with laboratory findings.

**Keywords:** electrical conductivity, dielectric permittivity, high-frequency, electromagnetic induction, shielding, sensor, soil, precision agriculture

# Sažetak

**Istovremeno mjerenje električne vodljivosti i dielektrične permitivnosti tla primjenom visokofrekvencijske elektromagnetske indukcije**

Tlo je heterogene strukture i sastoji se od krutih čestica, tekućine, zraka i organskih tvari, a sastav se može značajno razlikovati i na manjem području kao što je poljoprivredno polje. Mapiranje značajki tla na nekom području daje vrijedne informacije koje se mogu iskoristiti za bolje upravljanje tlom u preciznoj poljoprivredi. Elektromagnetski parametri tla (električna vodljivost, dielektrična permitivnost, magnetska susceptibilnost) ovise o fizikalnim i kemijskim svojstvima tla kao što su udio vode u tlu i salinitet te se mogu povezati empirijskim i teorijskim modelima. Blizinska ispitivanja tla prikladna su za mapiranje značajki tla na manjem prostoru jer imaju visoku vremensku i prostornu razlučivost podataka. Elektromagnetski modaliteti korišteni u ispitivanju značajki tla su kontaktno mjerenje otpornosti, kapacitivno spregnuto mjerenja otpornosti, elektromagnetska indukcija i georadar. Zbog rada u različitim frekvencijskim područjima, ti modaliteti se mogu smatrati komplementarnim. Kontaktna otporna i kapacitivna metoda su osjetljive na električnu vodljivost (otpornost) tla, elektromagnetski induktivni senzori su osjetljivi na električnu vodljivost i magnetsku susceptibilnost, a georadar na dielektričnu permitivnost i električnu vodljivost.

U ovom doktorskom radu istražuje se mogućnost istovremenog određivanja električne vodljivosti i dielektrične permitivnosti tla korištenjem visokofrekvencijske elektromagnetske indukcije u frekvencijskom području od 3 MHz do 30 MHz. U tom frekvencijskom području raste osjetljivost na električnu vodljivost i dielektričnu permitivnost, te je pokazano da je moguće prijenosnim senzorom tla uz odgovarajuću geometriju i potiskivanje neželjene elektromagnetske sprege odrediti oba parametra na jednoj frekvenciji.

Glavne hipoteze istraživanju su: 1.) Visokofrekvencijski elektromagnetski induktivni modalitet prikladan je za određivanje električne vodljivosti i dielektrične permitivnosti tla, i može se implementirati koristeći geometriju senzora i elektroničku instrumentaciju pogodne za prijenosnu upotrebu; 2.) Moguće je razdvojiti i odrediti utjecaje električne vodljivosti i dielektrične permitivnosti tla usporedbom podataka dobivenih visokofrekvencijskom elektromagnetskom induktivnom metodom i rezultata modela senzora; 3.) Neželjeni mehanički, temperaturni i elektromagnetski utjecaji mogu se kontrolirati i potisnuti prikladnom geometrijom senzora ili izvedbom elektroničke instrumentacije.

Znanstveni doprinos istraživanja sastoji se od tri dijela: 1.) Na modelu zasnovana metoda mjerenja električne vodljivosti i dielektrične permitivnosti tla primjenom visokofrekvencijske elektromagnetske indukcije, 2.) Analiza neželjene elektromagnetske sprege i tehnike za potiskivanje smetnji, 3.) Geometrija senzora i elektronička instrumentacija za istovremeno mjerenje električne vodljivosti i dielektrične permitivnosti tla primjenom visokofrekvencijske elektromagnetske indukcije.

U prvom poglavlju disertacije (Chapter 1 Introduction) opisana je motivacija za mapiranje tla u preciznoj poljoprivredi upotrebom blizinskih ispitivanja te su definirani efektivni elektromagnetski parametri tla i njihova veza s fizikalnim i kemijskim svojstvima tla. Dan je opsežan pregled istraživanja o elektromagnetskim senzorima tla te su detaljnije opisane metode kontaktnog mjerenja otpornosti tla, kapacitivno spregnutog mjerenja otpornosti, elektromagnetskog induktivnog mjerenja i georadara. Također, dan je pregled stanja tehnologije za visokofrekvencijske elektromagnetske induktivne senzore tla. Definirane su glavne hipoteze istraživanja i znanstveni doprinos disertacije.

U drugom poglavlju (Chapter 2 Analytical model) opisan je analitički model senzora izveden iz Maxwellovih jednadžbi i jednadžbi elektromagnetskih potencijala u punovalnom obliku. Izveden je model vektorskog magnetskog potencijala odašiljačke zavojnice iznad dvoslojnog tla (svaki sloj je homogeni i izotropni materijal s definiranom vodljivošću, permeabilnošću i permitivnošću) i induciranog napona prijemne zavojnice u obliku Sommerfeldova integrala. Model uključuje jednu odašiljačku i jednu prijemnu zavojnicu kvadratnog presjeka, a pretpostavljeno je da je odašiljačka zavojnica mala u odnosu na valnu duljinu pobude te je struja uniformna. Inducirani napon prijemne zavojnice sastoji se od primarne komponente zbog induktivnog vezanja u slobodnom prostoru te sekundarne komponente zbog doprinosa tla. Na temelju Lorentzovog teorema recipročnosti i Bornove aproksimacije pokazano je da osjetljivost omjera sekundarnog i primarnog napona ovisi linearno s frekvencijom za električnu vodljivost, kvadratno s frekvencijom za dielektričnu

permitivnost, dok je za magnetsku permeabilnost neovisna o frekvenciji. Rezultati modela prikazali su primjenjivost visokofrekvencijske elektromagnetske induktivne metode za istovremeno određivanje vodljivosti i permitivnosti tla neovisno o permeabilnosti.

U trećem poglavlju (Chapter 3 Sensor design and electronic instrumentation) opisana je elektronička instrumentacija i mjerni postav predloženog senzora temeljenog na visokofrekvencijskoj elektromagnetskoj indukciji. Za pobudu i akviziciju signala korišten je vektorski analizator mreže spojen na projektirano elektroničko sučelje koje se sastoji od nekoliko pojačala ukupnog pojačanja 40 dB i niskopropusnog filtra gornje granične frekvencije 35 MHz. Zavojnice s elektrostatskim oklopom izvedene u tehnologiji tiskanih veza. Odašiljačka zavojnica ima 3 zavoja, a prijemna zavojnica 4 zavoja, a vanjski promjer obiju zavojnica je 7 cm. Kako bi se smanjio kapacitet zavojnice korištene su odabrane dimenzije i mali broj zavoja čime je postignuta rezonantna frekvencija oko 70 MHz, a uz korištenje oklopa smanjuje se ispod 40 MHz zbog dodatnih parazitnih kapaciteta. Elektrostatski oklop je dimenzija 87.5 x 87.5 mm, a postavlja se s gornje i donje strane svake zavojnice te je spojen na referentni potencijal. Isprobana su 2 različita uzorka oklopa češljaste strukture kako bi se smanjila količina bakra čime se smanjuju inducirane strujne petlje u oklopu i induktivni gubitci.

Laboratorijski mjerni postav se sastoji od baterijski napajanog senzorskog sustava postavljenog na drvenu konstrukciju ispod koje se postavlja plastična posuda dimenzija 58.3 cm x 37.2 cm x 28.3 cm. Maksimalni volumen medija u posudi je 61 litra, a korištena je deionizirana voda u koju je dodavana sol ili šećer čime se mijenjaju elektromagnetska svojstva medija. Opisane su postavke simulacije te geometrija modela senzora i laboratorijske konstrukcije za numeričku analizu metodom konačnih elemenata (FEM) koji je korišten za usporedbu s laboratorijskim mjerenjima. Opisana je mjerna procedura korištena u laboratorijskim i terenskim ispitivanjima. U prvom koraku izmjeren je odziv senzora u zraku bez prisutnosti medija, a zatim odziv senzora kad je ispod prisutan medij. Odziv senzora u zraku je primarno induktivno vezanje, a odziv iznad medija superpozicija primarnog vezanja i sekundarnog vezanja zbog utjecaja medija. Iz tih mjerenja dobiven je omjer sekundarnog i primarnog napona te je eliminirana prijenosna funkcija instrumentacije čime se rezultati mogu usporediti s analitičkim i numeričkim modelom.

U četvrtom poglavlju rada (Chapter 4 Analysis of unwanted electromagnetic coupling and interference rejection techniques) analiziran je utjecaj neželjene elektromagnetske sprege, temperature, mehaničkog pomaka i promjene udaljenosti senzora od tla. Pokazano je da na višim frekvencija oklop uspješno smanjuje kapacitivnu spregu između zavojnica i medija te je opisana metoda odabira oklopa. Za odabir odgovarajućeg oklopa razvijena je metoda estimacije

parametara direktnog vezanja između zavojnica dobivenih iz lineariziranog nadomjesnog modela senzora i izmjerenog odziva senzora u zraku. Korištena je činjenica se okretanjem odašiljačke zavojnice mijenja smjer magnetskog momenta i time predznak induktivnog vezanja dok kapacitivno vezanje ostaje isto. Isprobano je 36 kombinacija različitih uzoraka oklopa i udaljenosti oklopa od zavojnica te je odabran oklop češljastog uzorka udaljen od zavojnice 4 mm s obje strane.

Utjecaj visine senzora iznad tla (liftoff) je analiziran koristeći analitički model i laboratorijski iznad spremnika s različitim vodljivostima slane otopine. U uvjetima konstante permitivnosti moguće je istovremeno mjeriti vodljivost tla i udaljenost od tla. Pokazano je da u slučaju valjanosti Bornove aproksimacije, utjecaj udaljenosti je neovisan od elektromagnetskih značajki tla. Utjecaj temperature analiziran je eksperimentalno u uvjetima konstantne i promjenjive temperature okoliša. Terenski eksperiment pokazuje da postoji temperaturni pomak kad je senzor izložen sunčevom svjetlu te postoji potreba za kompenzacijom temperaturnog pomaka elektronike. Utjecaj mehaničkog pomaka zavojnica analiziran je koristeći FEM simulacije i pokazano je da su najznačajnija odstupanja u slučaju nagiba odašiljačke zavojnice i promjene vertikalnog posmaka zavojnica.

U petom poglavlju (Chapter 5 Results) predstavljeni su mjerni rezultati laboratorijskih eksperimenata i terenskog ispitivanja. U laboratorijskom dijelu istraživanja, analiziran je odziv senzora na električnu vodljivost i dielektričnu permitivnost u rasponu tipičnom za većinu tla (10 mS/m do 300 mS/m za vodljivost te 1 do 78 za permitivnost). Senzor je postavljen iznad spremnika napunjenog sa 61 l deionizirane vode u koju je dodana sol u određenim koracima kako bi se promijenila električna vodljivost homogenog medija. Dielektrična permitivnost je mijenjanja dodavanjem šećera u deioniziranu vodu. S obzirom na potrebnu količinu šećera, relativnu permitivnost je bilo moguće smanjiti od 78 do 62. U drugom pristupu korišten je dvoslojni medij, gdje je promjenom razine vode efektivna permitivnost mijenjana u rasponu od 1 do 78. Rezultati eksperimenta su uspoređeni s numeričkim rezultatima dobivenim metodom konačnih elemenata. Rezultati se kvantitativno dobro poklapaju te je pokazano da je moguće istovremeno odrediti električnu vodljivost i dielektričnu permitivnost iz mjerenja na jednoj frekvenciji. U terenskim mjerenjima ispitan je laboratorijski prototip tako da je u prvom eksperimentu senzor postavljen je na tlo prethodno zalijevano deioniziranom ili slanom vodom. Rezultati terenskih ispitivanja pokazali su trendove koji se poklapaju s laboratorijskim ispitivanjima, ali ih nije bilo moguće dodatno kvantitativno interpretirati zbog nedostatka rezultata iz drugih senzorskih modaliteta. Također, identificirani su temperaturni i mehanički utjecaji koji nisu bili prisutni u laboratoriju.

U šestom poglavlju disertacije (Chapter 6 Conclusions) dani su glavni zaključci iz svih poglavlja. Opisani su glavni izazovi u istraživanju te su iznesena postignuća koja su povezana sa znanstvenim doprinosima. Također, dane su smjernice za nastavak istraživanja u području visokofrekvencijske elektromagnetske indukcije za određivanje značajki tla.

Frekvencijsko područje razvijenog senzora je između klasičnih induktivnih senzora na nižim frekvencijama te georadara na višim frekvencijama te može pružiti komplementarne informacije drugim senzorskim modalitetima. Predložen senzor je osjetljiv na električnu vodljivost i dielektričnu permitivnost u rasponu tipičnom za tla. Pokazano je da je visokofrekvencijski elektromagnetski induktivni senzor izvediv uz korištenje elektrostatskog oklopa, ali za terenski prototip je također potrebno kompenzirati utjecaj temperature i promjene visine senzora od tla. Analitički model te rezultati FEM simulacija i laboratorijskih mjerenja pokazuju da je moguće istovremeno mjeriti električnu vodljivost i dielektričnu permitivnost uz kalibraciju senzora.

Istraživanje se može nastaviti u više smjerova. Za uspješno terensko ispitivanje potrebno je razviti novu generaciju senzora što uključuje razvoj elektroničkog sklopovlja, kompenzaciju temperature te sklopovlja za pobudu i akviziciju signala. Nadalje, moguće je optimirati dimenzije zavojnica i oklopa. Također, potrebno je implementirati kompenzaciju promjene visine senzora od tla što je moguće višefrekvencijskom pobudom ili korištenjem dodatnog modaliteta za mjerenje udaljenosti. Razvijeni prototip u kombinaciji s kalibracijom zasnovanom na analitičkom modelu otvara vrata multidisciplinarnom pristupu jer bi se mogao koristiti u kontekstu geoznanosti i precizne poljoprivrede.

Rezultati ovog rada su obećavajući te potiču daljnja istraživanja visokofrekvencijskog elektromagnetskog induktivnog modaliteta u kontekstu mjerenja i mapiranja značajki tla.

**Ključne riječi:** električna vodljivost, dielektrična permitivnost, visoke frekvencije, elektromagnetska indukcija, oklapanje, senzor, tlo, precizna poljoprivreda

# Contents

# Contents

# Chapter 1

# Introduction

## 1.1 Soil sensing

Soil is an essential component of the environment and has a critical role in sustaining life on Earth. It provides necessary nutrients and water for plant growth, oxygen for root respiration, acts as a plant support structure, and is a habitat for many microorganisms and animals that are vital to the ecosystem [1]. Also, soil acts as a filter for groundwater and provides a foundation for the built environment. Soil is also a limited resource, and human-induced degradation poses a major ecological concern [2]. It is necessary to monitor the properties of the soil to improve agricultural production, preserve natural resources, and manage the soil sustainably [3]. Soil sensing measures and monitors physical and chemical soil properties such as water content, salinity, nutrients, pH value, and mechanical density. It is used in research areas such as precision agriculture, inspecting buried infrastructure, archeology, environmental science, and humanitarian demining [4]–[7].

Soil properties change over time, and due to soil heterogeneity, they can also vary from point to point over a relatively small area. Soil sensing approaches differ in spatial and time data density. Sensing approaches are also classified by measurement distance from the soil into proximal and remote soil sensing. Remote sensing is non-invasive and done using sensors mounted on aerial vehicles or satellites, while in proximal soil sensing, sensors operate near the soil, usually less than 2 meters from the ground [8].

Remote soil sensors map larger soil areas with lower spatial resolution, usually a few meters and above [9]. Temporal resolution is also low, typically from a day to a few months, as

they are constrained by price and satellite availability. Remote sensors can be passive or active: passive sensors measure radiation from natural sources in the visible, infrared, thermal, or microwave electromagnetic spectrum, while active sensors generate electromagnetic waves and measure the reflection from the surface, usually using the microwave spectrum, for example, radar or lidar [10][11]. Passive remote sensors are further classified into multispectral and hyperspectral imaging modalities. Multispectral modality utilizes selected discrete electromagnetic bands in the nanometer wavelength region, providing information about soil degradation or biomass yield. In contrast, the hyperspectral modality captures information over a wide range of wavelengths, providing more detailed information about changes in the soil cover, such as leaf area, crop biomass, or leaf nitrogen content [12].

Considering the measurement location, proximal soil sensing (PSS) can be done in the laboratory or field. Laboratory measurements are carried out on the soil samples obtained in the field. They give the most accurate results and are used to calibrate other methods. The drawback is that the soil samples must be transported to the laboratory and prepared for analysis, making it expensive and time-consuming [13]. Proximal soil sensors in the field obtain real-time information about soil properties, and depending on the sensor modality, they can be in contact with the soil or contactless [8]. The proximal soil sensors differ in the spatial density of the obtained data. They can be point sensors that measure the small volume of the soil, sensor networks that combine more point sensors over the area, or mobile sensors that can be moved across the measured field. Laboratory sensors are point measurements as the samples are taken from arbitrary locations, and field sensors enable all approaches to sensing.

Point measurement is a method for measuring soil properties, where the soil samples are taken randomly or in predefined locations. Point measurements provide temporal and spatially sparse information about soil moisture, salinity, pH value, temperature, and physical density. Soil moisture is determined indirectly with capacitive probes consisting of electrodes inserted in the soil. The soil between the electrodes is a dielectric, and the impedance is measured at a high excitation frequency, typically from 5 to 150 MHz [14]. Soil water content and salinity can be measured using a time-domain reflectometry (TDR) probe. Electrodes are placed in the ground, representing a transmission line along which rectangular pulses of the frequency spectrum from 20 kHz to 2.5 GHz are transmitted. The measured signal propagation speed depends on the permittivity, and the attenuation of the signal depends on the conductivity of the soil [15]. Electrochemical sensors measure the pH value of the soil and the presence of chemical elements, the most important of which are nitrogen, potassium, sodium, and calcium.

Mechanical sensors measure the forces and sounds that occur due to the probe's contact with the ground and are used to determine the mechanical resistance and compactness of the soil [8].

Wireless sensor networks (WSN) consist of sensor nodes scattered in the field, measuring soil properties and communicating with each other. The basic components of a sensor node are a microcontroller, communication module, memory, power source, and sensors. The limitations of WSNs are energy consumption, processing power, and limited memory for data storage. Each sensor node is an autonomous unit with limited available energy, typically battery-powered. The research places a large emphasis on methods to extend the lifespan of sensor nodes. Various methods of reducing node consumption and collecting energy from the environment (solar, thermal, wind) are being explored. Most of the energy is consumed by communication between nodes, making it important to choose the correct communication protocol to optimize consumption, the amount of data transmitted, and the transmission distance [16]. Sensors can measure properties related to the soil, plants, and environment. Many prototypes and commercially available sensor nodes measure multiple features simultaneously [17], [18]. Nodes are scattered over the area of interest in which the properties are measured. While using more nodes increases the spatial density of data, it is still insufficient for mapping features [19], and more nodes increase the network cost [20]. The temporal density depends on the measurement frequency, and more frequent measurements increase energy consumption. Measuring with sensor networks provides spatially sparse but temporally dense information [21].

The soil usually has a heterogeneous structure and significant spatial variability over the given area, so the properties of the soil samples can vary depending on the location where they are taken. From this fact, detailed maps of soil properties are needed to better utilize the resources in soil management. Electromagnetic proximal soil sensors are a good option for mapping electromagnetic soil properties from which the pedological soil properties can be derived. Their advantage is that they can be contactless as they transmit electromagnetic waves into the soil, providing fast data acquisition and dense spatial information about the soil. The cost of surveys is usually less than remote sensing, so the measurements can be conducted as needed to obtain the trends in changes in soil parameters.

## 1.2 Electromagnetic properties of soil

Electromagnetic soil properties (electrical conductivity, dielectric permittivity, magnetic susceptibility) depend on physical and chemical properties such as salinity, water content, organic matter content, density, and temperature. Soil consists of different-sized solid particles, liquid, air and organic matter. Because of the heterogeneous soil structure, the apparent electrical properties are measured, i.e., the average values across the soil volume determined by the sensor spatial sensitivity. Also, due to the different polarization mechanisms and various conductive paths in the soil, the electrical conductivity $\sigma$, dielectric permittivity $\varepsilon$ and magnetic susceptibility $\mu$ are complex, frequency-dependent values represented with real and imaginary parts as [22]:

$$\sigma^*(\omega) = \sigma'(\omega) + j\sigma''(\omega) \ , \tag{1}$$

$$\varepsilon^*(\omega) = \varepsilon'(\omega) + j\varepsilon''(\omega) \ , \tag{2}$$

$$\mu^*(\omega) = \mu'(\omega) + j\mu''(\omega) \ . \tag{3}$$

The Maxwell's equation for rotation of the magnetic field **H,** with the harmonic excitation $\exp(j\omega t)$ can be written as

$$\nabla \times \vec{H} = \left(\sigma^*(\omega) + j\omega\varepsilon^*(\omega)\right)\vec{E} \ , \tag{4}$$

considering the complex values of electromagnetic properties given in equations (1), (2) and (3), this can be rewritten in form of

$$\nabla \times \vec{H} = \left(\sigma_{eff} - j\omega\varepsilon_{eff}\right)\vec{E} \tag{5}$$

with effective values of electrical conductivity and dielectric permittivity $\sigma_{eff}$ and $\varepsilon_{eff}$ being

$$\sigma_{eff} = \sigma' + \omega\varepsilon'' \ , \tag{6}$$

$$\varepsilon_{eff} = \varepsilon' + \frac{\sigma''}{\omega} \ . \tag{7}$$

In practice, it is difficult to determine both real and imaginary parts of electromagnetic properties, so the effective measured properties are defined as real numbers consisting of real and imaginary parts of $\sigma^*$ and $\varepsilon^*$ [23]. Standard laboratory measurements of prepared samples obtain direct current (DC) electrical conductivity at lower frequencies $\sigma_{eff}$, which is dominantly the real part of electrical conductivity $\sigma'$, and dielectric permittivity at higher frequencies $\varepsilon_{eff}$ dominantly affected by the real part of permittivity $\varepsilon'$. In low-frequency measurements, soil electromagnetic parameters can also be written in terms of effective alternating current (AC)

conductivity as the imaginary part of permittivity is in phase with the real part of conductivity [24]:

$$\sigma_{eff} = \sigma_{real} + \omega\varepsilon_{imag}\,. \tag{8}$$

An example of frequency-independent measured electromagnetic property is the apparent electrical conductivity ($EC_a$), the average electrical conductivity of bulk soil volume. The soil has 3 distinct conductive paths: through solid particles in direct contact, a liquid pathway via dissolved solid particles, and a solid-liquid pathway via dissolved ions [25]. Other electromagnetic properties of the soil (dielectric permittivity and magnetic susceptibility) can also be considered as averaged across the soil volume.

Empirical relations connect physical and chemical soil properties with the measurements of its electromagnetic properties. The Archie's law is an example of an empirical formula that relates soil porosity and $EC_a$ in saturated rocks and sand soils:

$$EC_a = a\sigma_w\Phi^m\,, \tag{9}$$

where $a$ and $m$ are empirical constants that depend on specific properties of rocks and fluids, $\Phi$ is the porosity of a medium, and $\sigma_w$ pore water electrical conductivity [25], [26].

An extension of Archie's law is the Waxman-Smits model, which considers the influence of clay minerals on soil $EC_a$ and is given as:

$$EC_a = a(\sigma_r + \sigma_w)\Phi^m\,, \tag{10}$$

with $a$ and $m$ being geometrical constants, $\sigma_w$ pore water conductivity, and $\sigma_r$ is electrical conductivity due to the cation exchange [27]. The Hannai-Bruggeman-Bussian equation presented in [27] applies to a model of a conductive rock matrix immersed in conductive water. For low-frequency measurements where the influence of dielectric permittivity is negligible, the equation is:

$$EC_a = \sigma_w\Phi^m\left(\frac{1 - \dfrac{\sigma_w}{\sigma_r}}{1 - \dfrac{\sigma_w}{EC_a}}\right)^m\,, \tag{11}$$

where $EC_a$ is the conductivity of the mixture, $\sigma_r$ conductivity of dispersed particles, $\sigma_w$ conductivity of the continuous medium, $m$ cementation factor and $\Phi = 1 - \Phi_r$, with $\Phi_r$ being the fractional volume of dispersed particles. In the case of conductive soils, in which the majority of water conductivity is much larger than the conductivity of solid particles, the equation can be approximated as

$$EC_a \cong m\sigma_r(1 - \Phi^m) + \Phi^m\sigma_w\,. \tag{12}$$

An example of empirical relation that connects dielectric permittivity with physical properties is Topp's equation used for the estimation of soil water content $\theta_v$ as the permittivity of water (≈80) is much larger than soil [28]:

$$\theta_v = -5.3 \cdot 10^{-2} + 2.92 \cdot 10^{-2} \varepsilon - 5.5 \cdot 10^{-4} \varepsilon^2 + 4.3 \cdot 10^{-6} \varepsilon^3 \ . \tag{13}$$

The equation is fitted to laboratory measurements in the frequency range from 1 MHz for four different soil types but approximates most unsaturated mineral soils well. It is usually used in time-domain reflectometry and ground penetrating radar (GPR) measurements to estimate water content and provides good estimation for coarse and medium-textured soils [29].

The frequency characteristics of material dielectric permittivity on a macroscopic scale can be described by several empirical relations describing polarization mechanisms (resonance and relaxation), with the most known being the Debye model and the Cole-Cole model, given as:

$$\varepsilon = \varepsilon'_\infty + \frac{\varepsilon_{real,0} - \varepsilon_{real,\infty}}{1 + (j\omega\tau)^{(1-\alpha)}} \ , \tag{14}$$

where $\varepsilon_{real,0}$ and $\varepsilon_{real,\infty}$ are static permittivities at frequencies much lower and higher than the characteristic relaxation time of the medium $\tau$, and $\alpha$ is the polarizability of the material. The Cole-Cole model can characterize the spread in relaxation times, and in the case of $\alpha=0$, the model becomes the Debye model that describes one relaxation time [24].

Magnetic susceptibility $\chi$ is the soil's ability to become magnetized by an external magnetic field. Considering the magnetization properties, the material can be diamagnetic, paramagnetic and ferromagnetic [24]. Diamagnetic materials, such as water and copper, have a small repulsion from a magnetic source when placed in a magnetic field, resulting in a magnetic susceptibility that is a small negative number ( $\chi \approx - 10^{-6}$ SI). Paramagnetic materials, such as granite, aluminum and magnesium, have a small positive magnetic susceptibility ($\chi \approx +10^{-5}$ SI) and are slightly attracted to a magnetic source when put into a magnetic field. Ferrimagnetic materials, such as iron, nickel and cobalt, can be strongly magnetized.

Due to the different magnetization mechanisms, the magnetic susceptibility of homogeneous materials is complex and frequency dependent, given as:

$$\chi^* = \chi' - j\chi'' \ , \tag{15}$$

where $\chi'$ is the real part representing magnetizability, and $\chi''$ is the imaginary part representing material losses, i.e., magnetic viscosity. Both real and imaginary parts of magnetic susceptibility of homogeneous material are also frequency dependent:

$$\chi' = \chi_0' \frac{1 - \left(\dfrac{\omega}{\omega_s}\right)^2}{\left(1 - \dfrac{\omega^2}{\omega_s^2}\right)^2 + \left(\dfrac{\omega}{\omega_x}\right)^2} \quad , \tag{16}$$

$$\chi'' = \chi_0' \frac{\dfrac{\omega}{\omega_x}}{\left(1 - \dfrac{\omega^2}{\omega_s^2}\right)^2 + \left(\dfrac{\omega}{\omega_x}\right)^2} \quad , \tag{17}$$

with $\chi_0'$ being magnetic susceptibility at zero frequency, and angular frequencies $\omega_s$ and $\omega_x$ depend on material properties [24].

## 1.3 Approaches to electromagnetic proximal soil sensing

Electromagnetic proximal soil sensors are instruments used to measure soil properties and map soil characteristics. They can be in contact with the soil, such as direct current (DC) resistivity measurement, or contactless, such as capacitively coupled resistivity (CCR) measurement, ground-penetrating radar (GPR), and electromagnetic induction (EMI). Mobile proximal soil sensors are handheld devices or devices mounted on a vehicle, making them ideal for mapping soil properties on a smaller scale, such as agricultural fields or archaeological sites, which can give detailed maps of soil properties at a finer scale.

### 1.3.1 Direct current resistivity measurement

Contact measurement of soil electrical resistivity, i.e., direct current resistivity (DC), was the first electromagnetic sensing method for measuring electromagnetic soil properties [30]. A direct or low-frequency current is injected into the soil using a pair of electrodes, and the voltage drop is measured by one or more pairs of receiver electrodes to determine the electrical resistivity $\rho$. The measured soil volume depends on the electrode spacing, and the large measurement volume reduces the influence of local-scale variability. The electrodes must be in good physical contact with the soil to mitigate the errors due to the poor galvanic contact, making this method less reliable on stony or dry and dense soils [25].

For the basic 4-point measurement and soil modeled as homogeneous isotropic half-space, the apparent electrical resistivity $\rho$ averaged over specified soil volume is defined as:

$$\rho = \frac{U}{I} \cdot K \tag{18}$$

where $U$ is the measured voltage, $I$ is the injected current, and $K$ is the geometry coefficient. The geometry coefficient for the configuration with 2 current electrodes denominated A and B and 2 voltage electrodes M and N is:

$$K = \frac{2\pi}{\dfrac{1}{r_{MA}} + \dfrac{1}{r_{NA}} + \dfrac{1}{r_{MB}} + \dfrac{1}{r_{NB}}} , \tag{19}$$

with $r_{MA}$, $r_{MB}$, $r_{NA}$, and $r_{NB}$ as distances between the electrodes.

Several different electrode configurations differ in certain features, including sensitivity to horizontal structures, sensitivity to vertical structures, probing depth, probing surface, and signal-to-noise ratio [31]. Wenner's configuration, Schlumberger's, dipole-dipole, pole-dipole, and pole-pole configurations are most often used, **Figure 1**.
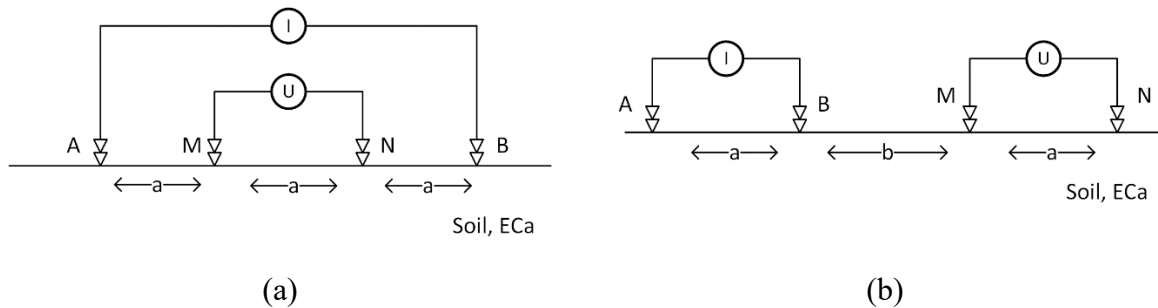


**Figure 1**. Electrode array configuration for DC resistivity: (a) Wenner array, (b) Dipole-dipole array

In Wenner's configuration, the distance between the electrodes is equal, where the outer pair consists of current electrodes and the inner pair consists of voltage electrodes. In the Schlumberger configuration, the distance between the outer current electrodes is further than between the inner voltage electrodes. Changing the current electrodes' spacing makes measuring the resistance at different soil depths possible. In the dipole-dipole configuration, the current and voltage electrodes are separated, and it is possible to achieve a greater depth of examination [31].

## 1.3.2 Capacitively coupled resistivity measurement

The capacitive coupled resistivity (CCR) measurement is a contactless method in which the alternating current is injected into the soil by electrodes using capacitive coupling. The measurement procedure is similar to the direct-resistivity method, but due to the capacitive coupling of electrodes and soil, the CCR is suitable for measuring stony soils, roads, pavements, ice, or frozen ground [32]. Sensor electrode configurations are similar to the ones used in DC measurements, and the dipole-dipole configuration is usually used. The measurement results can be interpreted using techniques like DC resistivity measurements if the quasi-stationary

approximation is valid and the excitation signal wavelength is much larger than the sensor dimensions. Low-frequency excitation signals, up to 50 kHz, are used. Two types of electrodes are used: line electrodes made with coaxial cables and point electrodes made from metal sheets galvanically isolated from the soil [33].

The basic case of 4-point capacitive measurement, i.e., electrostatic quadrupole, is discussed in [34]. The model of the electrostatic quadrupole is shown in **Figure 2**. The soil is modeled as a homogeneous half-space, and the poles are in the air. The electrodes represented by poles $C_1$ and $C_2$ carry electrical charges $Q$ and $-Q$, representing the current source, and the poles $P_1$ and $P_2$ measure the voltage. The electrostatic potential of the poles $C_1$ and $C_2$ in points $P_1$ and $P_2$ is calculated using the electrical images approach.
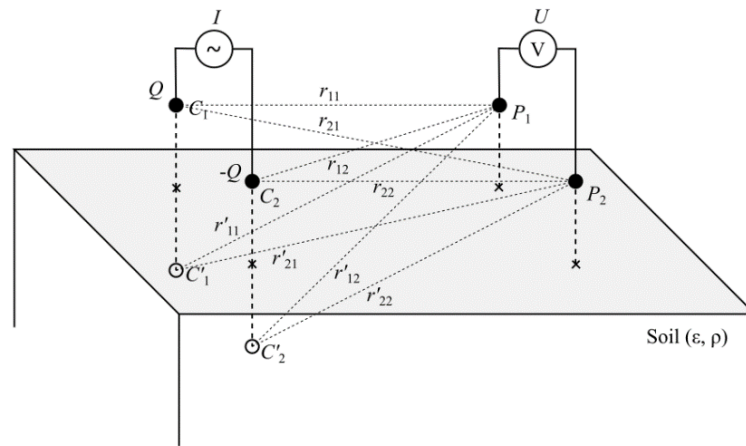


**Figure 2**. Quadripole geometry in quasi-stationary approximation. Excitation alternating current *I* is injected into the soil through C₁ and C₂. Voltage *U* is measured across P₁ and P₂. The charges in C'₁ i C'₂ are mirrored across the half-space border.

The charge Q in point C is mirrored symmetrically in relation to the half-space border to the charge Q' at point C' (20), where α is the coefficient depending on the properties of the medium (21).

$$Q' = -\alpha Q \tag{20}$$

$$\alpha = \frac{\varepsilon - 1}{\varepsilon + 1} \tag{21}$$

The potential of electrode *P* in the air at the distances *r and r'* from the original and mirrored charge is given in (22).

$$U(P) = \frac{Q}{4\pi\varepsilon_0 r}\left(\frac{1}{r} - \frac{\alpha}{r'}\right) \tag{22}$$

The quadrupole voltage is a superposition of all charge contributions (23), where $C_0$ is the characteristic capacitance of the quadrupole (24), and $K_S$ is the sensor geometry factor that depends on location and orientation to the ground (25).

$$U = \frac{Q}{C_0}(1 - K_S \alpha) \tag{23}$$

$$C_0 = \frac{4\pi\varepsilon_0}{\dfrac{1}{r_{11}} + \dfrac{1}{r_{22}} - \dfrac{1}{r_{12}} - \dfrac{1}{r_{21}}} \tag{24}$$

$$K_S = \frac{\dfrac{1}{r'_{11}} + \dfrac{1}{r'_{22}} - \dfrac{1}{r'_{12}} - \dfrac{1}{r'_{21}}}{\dfrac{1}{r_{11}} + \dfrac{1}{r_{22}} - \dfrac{1}{r_{12}} - \dfrac{1}{r_{21}}} \tag{25}$$

In the case of harmonic excitation signal where the quasi-stationary approximation is valid for slow varying charges with time:

$$Q(t) = \frac{1}{j\omega}I(t), \tag{26}$$

the formulation for potential is:

$$U = \frac{I}{j\omega C_0}(1 - K_S \alpha), \tag{27}$$

and the complex permittivity $\varepsilon$:

$$\varepsilon = \varepsilon_0 \varepsilon_r - j\frac{1}{\rho\omega}. \tag{28}$$

The factor $\alpha$ from (21) is then a complex number:

$$\alpha = \frac{\omega\varepsilon_0\rho(\varepsilon_r - 1) - j}{\omega\varepsilon_0\rho(\varepsilon_r + 1) - j}. \tag{29}$$

Capacitively coupled resistivity measurements have been the subject of scientific studies, and commercial devices are available. Authors in [35] present the device for soil impedance measurement based on an electrostatic quadrupole model, consisting of a transmitting dipole with an excitation frequency of 14.2 kHz and several receiver dipoles that are mutually galvanically isolated. A device with a similar configuration using excitation frequency from 2 mHz to 100 kHz is presented in [36]. Authors in [37] examine the influence of the distance between the electrodes and the ground. Small changes in height affect changes in the phase angle of the impedance. They conclude that it is necessary to know the exact height of the

electrodes to determine the soil parameters. They use a system consisting of a pair of current and voltage electrodes and excitation frequency from 100 Hz to 100 kHz. The design of the active capacitive probe working in a frequency range from 0.1 Hz to 1 kHz is given in [38]. The theoretical analysis of line electrodes and geometric factors was done in [32] and expanded in [39]. The commercially available device OhmMapper by Geometrics uses line electrodes and an excitation frequency of 16.5 kHz. The distances between the transmitter and receiver dipole are 5,10,15, and 20 meters, and the measurements are taken every 0.5 s. Another commercial device is CORIM, Iris instruments [40], with plate electrodes consisting of one transmitter and 6 receiver dipoles. The excitation frequency is 12 kHz, the device is towed on the ground, and the data is sampled at fixed intervals of 0.2 m.

The CCR modality is suitable for 3D mapping and soil depth profiling because it is possible to deploy sensor geometries with multiple pairs of receiver electrodes at different distances from the transmitter electrodes. The excitation frequency is in the audio range in which the electrodes are still dominantly capacitive, and the low-induction number approximation is valid. The excitation frequency is constrained with the electrode dimensions, as the inductive effects become dominant with the frequency increase and the low-induction number approximation, which must be satisfied to use inversion algorithms similar to the DC method. It is possible to sense dielectric permittivity only when the resistivity is large enough, such as frozen soils or ice. In other cases, the sensitivity is not high enough due to the soil conductivity [40].

## 1.3.3 Ground-penetrating radar

Ground-penetrating radar (GPR) is a contactless method for high-resolution subsurface exploration and mapping based on electromagnetic wave propagation and reflection [41]. GPR use is well-documented in various research areas, such as environmental science, geology, engineering, archeology, and forestry [42]. Some of the main applications are, for example, determining the composition of layers of soil and rock [43], measuring soil water content [44], plant root mapping [45], detection of groundwater contamination, and detecting buried objects and structures [46].

A typical GPR  operates in the very and ultra-high frequency range (30 MHz to 2.5 GHz) and consists of a transmitter antenna transmitting high-frequency pulses into the ground and one or more receiver antennae that detects the reflected wave, and they can have fixed or variable separation. GPR can work in the frequency or time domain, with the latter most widely

used in commercially available devices due to the simpler data acquisition and signal processing requirements [47].

GPR can determine soil dielectric permittivity and electrical conductivity by measuring two-way travel times, phase velocity, and attenuation of the electromagnetic waves reflected from soil heterogeneities. From Maxwell's equations and constitutional terms, the electrical field E for sinusoidal excitation and homogeneous isotropic material with A as the maximum wave amplitude, ω angular frequency, $\alpha$ wave attenuation, and $\beta$ phase is given as [48]

$$E(\beta,t) = Ae^{-j\left(\frac{\beta}{v} - \omega t\right)} e^{-\alpha\beta} . \tag{30}$$

The attenuation term $\alpha$ and phase $\beta$ are:

$$\alpha = \omega \sqrt{\frac{\mu\varepsilon}{2}\left(\sqrt{\left(1 + \frac{\sigma^2}{\varepsilon^2 \omega^2}\right)} - 1\right)} , \tag{31}$$

$$\beta = \omega \sqrt{\frac{\mu\varepsilon}{2}\left(\sqrt{\left(1 + \frac{\sigma^2}{\varepsilon^2 \omega^2}\right)} + 1\right)} . \tag{32}$$

From these expressions, the phase velocity $v$ can be derived as

$$v = \frac{\omega}{\beta} , \tag{33}$$

the skin depth $\delta$ of the wave as

$$\delta = \frac{1}{\alpha} , \tag{34}$$

and loss tangent as

$$\tan\theta = \frac{\sigma}{\omega\varepsilon} . \tag{35}$$

The wave attenuation α and velocity $v$ depend on the soil's electrical conductivity $\sigma$ and permittivity ε, and for most soil cases, the relative permeability is considered 1 [48]. Typical GPR operates under the assumption of low-loss approximation in which the energy dissipation due to the conduction currents is small compared to the energy storage due to the displacement currents [46]. Higher excitation frequency provides better measurement resolution, and the lower frequencies can penetrate deeper into the soil. Skin depth is decreased in the lossy soil with relatively large electrical conductivity (above 0.4 S/m), which makes the measurement unsuitable for clay-rich soils and soils mixed with saline or mineral-rich soils [49].

Estimating volume water content (VWC) is widely used in GPR soil studies, as the relative permittivity of dry soil particles ranges from 3 to 8, and the permittivity of water is 80,

so the presence of water represents a significant contrast in permittivity [28], [41]. The standard approach in acquiring VWC is using GPR, which works in common-offset profiling mode by measuring wave travel times, where the transmitter and receiver antennae are at the fixed spacing. This approach is suitable for large-scale mapping, but the reflector is needed at the known depth, either natural or buried, to estimate the wave travel times [44]. The alternative approach suggests techniques like common-midpoint and wide-angle reflection and refraction measurements in which spacing between the transmitter and receiver is varied or multiple receivers are used, but this complicates the design and signal processing [44], [50].

## 1.3.4 Low-frequency electromagnetic induction

Low-frequency electromagnetic induction (LFEMI) sensors are used in geophysical, archaeological and agricultural surveys for measuring electromagnetic soil properties (electrical conductivity $\sigma$ and magnetic susceptibility $\mu$). Precision agriculture applications of LFEMI include estimating soil salinity, soil texture, water content, and organic matter [51]. They operate in a low-frequency range, below 300 kHz, as defined by ITU [52].

The sensor consists of a transmitter coil and one or more receiver coils, separated by a distance, typically up to a few meters. A transmitter coil (TX) is excited by alternating current that generates the primary magnetic field $H_P$, which in turn induces the eddy currents in the soil. The induced eddy currents generate the secondary magnetic field $H_S$ proportional to the excitation frequency $f$ and dependent on the soil electromagnetic properties, which then induces voltage in the receiver (RX) coil. The most common coil configurations are vertical and horizontal coplanar dipoles [7], [53], but they can also be mutually perpendicular [54].

LFEMI soil sensors operate under the assumption of low-induction number $B$, in which the skin depth $\delta$ of the wave propagating in a homogeneous half-space is much larger than the sensor's dimensions, defined as the distance when the wave amplitude attenuates to 1/e of the surface amplitude:

$$\delta = \sqrt{\frac{2}{\omega\mu\sigma}} \ .$$ (36)

Low induction number approximation is valid if $B<<1$, defined as the ratio of transmitter and receiver coil distance $d$ and skin depth $\delta$:

$$B = \frac{d}{\delta} \approx d\sqrt{\omega\mu\sigma} \ .$$ (37)

This can be achieved if the coil separation $d$ is much smaller than skin depth $\delta$, and as $d$ is fixed by sensor design, excitation frequency $f$ has to be adequately chosen:

$$f << \frac{1}{\pi\mu\sigma d^2} \tag{38}$$

Under these conditions, the ratio of the secondary and primary magnetic fields for transmitter-receiver configuration above the isotropic homogeneous medium is:

$$\frac{H_S}{H_P} = \frac{j\omega\mu_0\sigma d^2}{4} \tag{39}$$

where $\mu_0$ is the permeability of free space, $\sigma$ soil conductivity, and d is intercoil spacing. The quadrature component of the magnetic field ratio is linearly proportional to the soil's electrical conductivity, and the in-phase component is proportional to the soil's magnetic susceptibility. No magnetic coupling exists between the eddy currents induced in different soil layers, and displacement currents do not affect sensor response[53]. The low-induction number approximation is valid for excitation frequencies in the kilohertz range for typical sensors with intercoil separation up to a few meters and typical soils with electrical conductivity below 1 S/m. Under these conditions, the tested soil volume depends on the sensor geometry, intercoil separation and orientation [55].

The use of low-frequency EMI soil sensors is widely spread, and there are commercially available devices [7][56][57][58]. The most used device is the EM-38 manufactured by Geonics [59]. The basic version of the device consists of a transmitter and receiver coil with an intercoil separation of 1 m and an excitation frequency of 14.6 kHz. It can be used in a vertical or horizontal dipole configuration, where the effective depth of exploration is 1.5 m and 0.75 m, respectively. The newer device, EM38DD, consists of a horizontal and vertical coplanar dipole, which enables the measurement of soil properties at different depths. Version EM38-MK2 consists of one transmitter coil, and two receiver coils with intercoil distances of 0.5 m and 1 m from the transmitter, which enables simultaneous effective investigation depths of 0.75 m and 1.5 m for the vertical dipole and 0.375 m and 0.75 m for the horizontal dipole orientations. The sensor output is given as an in-phase and quadrature component of the ratio of secondary-to-primary magnetic field and enables the measurement of soil magnetic susceptibility and electrical conductivity [6], [53], [55].

The EMI devices produced by DUALEM [60] operate at a frequency of 9 kHz and measure both electrical conductivity and magnetic susceptibility simultaneously. They utilize sensor geometry consisting of coils in coplanar horizontal dipole and configuration with mutually perpendicular coils. The standard model DUALEM-1 has an intercoil separation of 1 m, resulting in an effective depth of exploration of 0.5  when used in a horizontal dipole

configuration and 1.5 m when used as a vertical dipole. Additionally, devices with multiple pairs of dipoles exist, with intercoil separation set at 2, 4, and 6 m, which enables soil properties to be measured at different depths and profiling. The device GEM-2 made by Geophex [61] is an example of a sensor with a multi-frequency excitation signal in the frequency range from 90 Hz to 22 kHz. It consists of a transmitter and receiver coil with 1.68 m intercoil separation and an additional receiver coil used to measure the primary magnetic field and compensation.

The research on electromagnetic induction soil sensors has focused on the development of new devices [56], [62], [63] and data interpretation [64]–[66]. A device for measuring electrical conductivity with an exploration depth of up to 10 m for detecting underground pollution is presented in [63]. It consists of a transmitter coil with a diameter of 32 cm, and two receiver coils at a 1.5 m and 2.5 m distance from the transmitter. The current probe measures the transmitter current, and 14 excitation frequencies are used from 2.5 kHz to 250 kHz. The primary magnetic field is compensated by subtracting the sensor response in the air from the response above the soil. The analysis of different coil orientations and geometries was done in [62], and the authors concluded that varying the coil angles improved imaging capabilities. Standard coplanar configurations have a non-linear sensitivity, and the vertical configuration where the TX coil is below the RX coil gives a better lateral resolution. A device with multiple receiver coils and multiple excitation frequencies of up to 250 kHz is presented in [56], with the transmitter coils located at different heights from the ground to improve primary field compensation. Authors in [67] describe a device with an inductive source and capacitive receiver for measuring the electric field and mapping resistive contrast in the soil. The excitation frequency is 5 kHz, and the transmitter-receiver spacing can be up to 30 m, depending on the desired exploration depth.

The device presented in [68][69] consists of a transmitter and receiver coil with an intercoil separation of 7.92 m mounted on a helicopter. Although an excitation frequency range from 380 Hz to 105 kHz is used, due to the large dimensions and mutual distance of the coils, the condition of a small inductive number is not satisfied, and therefore, the low-induction approximation is not valid. The influence of dielectric permittivity and magnetic susceptibility can be seen in the reduction of the real and the increase of the imaginary component of the magnetic field, leading to a wrong electrical conductivity estimation. The approach of using the lowest frequency for measuring magnetic susceptibility and the highest frequency for dielectric permittivity is proposed in [69], and with these measurements, the electric conductivity could be estimated on all used frequencies.

Another use of electromagnetic induction is in well-logging applications to obtain the properties of subsurface formations and fluids, such as oil, gas, or water, in stones and rocks [70]. These sensors consist of transmitter and receiver coils that are lowered into the borehole and measure electrical conductivity and magnetic permeability[71].

## 1.3.5 High-frequency electromagnetic induction

Increasing the operating frequency of the EMI sensor to a high-frequency range from 300 kHz to 30 MHz would increase sensitivity to electrical conductivity [72]. In addition, the sensitivity to dielectric permittivity becomes significant, making simultaneous measurement of the two parameters possible [73]. High-frequency EMI (HFEMI) modality could provide additional information about the soil properties and fill the gap between low-frequency EMI sensors working under low-induction number approximation and GPR measurements working under low-loss approximation [48].

The applicability of HFEMI sensors was analyzed for the detection of low-conductivity materials in which the response at the lower frequencies is too weak for detection. An example is detecting explosive devices with a small proportion of metal parts or materials with electrical conductivity below 0.1 MS/m, such as depleted uranium and carbon fiber objects [74]. Another application is a spectroscopic or tomographic inspection of biological tissue with conductivity less than 10 S/m [75], [76]. A theoretical approach to the simultaneous measurement of soil electrical conductivity and dielectric permittivity in the high-frequency range using EMI was discussed in [73]. The high-frequency EMI (HFEMI) modality was used for shallow subsurface profiling and mapping [72], [77]. However, these systems are impractically large for precision agriculture soil mapping, as they are designed for large and deep targets in the subsurface up to 50 m. Their construction involves multiple coils at different separations and orientations, making them susceptible to mechanical and temperature effects and potentially leading to inadequate data quality.

Another direction was proposed in [78] with shorter, fixed coil separation and construction resembling commercial LFEMI instruments for soil mapping [59]. The analysis in [78] was conducted at frequencies below 5 MHz, and the results indicated the possibility of simultaneous determination of conductivity and permittivity. At these frequencies, permittivity can be dominated by spatial polarization effects, complicating the relationship between soil water content and permittivity [78]. The device has an intercoil separation of 1.2 m, an excitation frequency of 1.56 MHz, and the exploration depth of up to 2.5 m. Although the test

showed good qualitative agreement with a laboratory and contact resistivity measurements, they could not quantitatively interpret the data.

Another attempt at high-frequency measurements in a similar frequency range was presented in [79] using off-the-shelf instrumentation. Soil impedance was calculated as the ratio of the measured electric and magnetic fields. The magnetic field was measured with a receiver coil, the electric field with an antenna, and the transmitter coil was spaced 4 to 16 m apart. A device consisting of a loop antenna array spaced 2 to 6 m apart and with an excitation frequency of 30 MHz is presented in [80]. The system measures the mutual impedance, electrical conductivity, and dielectric permittivity of ground, mainly river embarkments, but the large coil separation makes it unsuitable for mobile use. The measurement results were compared with the direct resistivity method, and the conclusion is that the results agree well.

An HFEMI sensor described in [81], [82] had horizontally overlapped transmitter and receiver coils to reduce primary coupling. The sensor operation was evaluated in the frequency range from 10 kHz to 20 MHz using a container filled with sand at varying water saturation levels as an inspected medium. The results were inconclusive because of the poor sensitivity of the proposed configuration. Both prototypes of [78] and [82] operate in the lower half of the high frequency range, and the studies do not consider capacitive coupling effects and electrostatic shielding of the coils, which is essential at high frequencies [83].

From the review of the state-of-the-art HFEMI sensors, it can be concluded that this modality is suitable for determining soil electrical conductivity and dielectric permittivity, but there are still challenges in designing such a device suitable for mobile use. The influence of both electromagnetic properties on sensor response requires more complicated data processing. The influential factors, such as mechanical construction, temperature drift and sensor lift-off, must also be considered as they affect the useful signal. With the increased frequency, the sensor becomes more sensitive to nearby metallic objects and the surroundings, and the capacitive coupling between the coils and the soil becomes comparable to inductive coupling. There is a need for mobile and handheld HFEMI sensors designed so that the unwanted coupling with surroundings is rejected, using adequate electronic instrumentation to measure induced voltage due to the electrical conductivity and dielectric permittivity, opening a possibility of the method for simultaneous measurement of these parameters.

## 1.4 Summary of the electromagnetic soil sensors in mapping applications

For mapping the electromagnetic properties of the soil at the field scale, the sensing modalities must have a volume of sensitivity and mobility to capture within-field soil variability. The appropriate modalities are direct current resistivity (DCR) measurement, capacitively coupled resistivity (CCR) measurement, ground-penetrating radar (GPR), and electromagnetic induction (EMI) measurement. They differ in their sensitivity to the electromagnetic parameters as they operate in different frequency ranges, but they all are sensitive to the electromagnetic parameters as averages over the volume of sensitivity, which is spatially dependent [58].

The DCR measurements require good mechanical contact with the soil, making it less reliable in dry, dense, or stony soils. The CCR technique avoids the contact issue inherent in the DCR technique while employing identical resistivity inversion algorithms, provided that the quasi-static approximation holds. The DCR and CCR measurements are only sensitive to electrical conductivity as the excitation is in the audio frequency range, usually a few hundred Hz.

GPR can be used to determine soil dielectric permittivity and electrical conductivity. It operates in the very and ultra-high frequency ranges, measuring two-way travel times and the attenuation of the electromagnetic waves from the soil heterogeneities. However, its effectiveness is limited to areas with relatively low electrical conductivity and requires either laborious data acquisition and processing or the presence of well-identifiable and continuous GPR reflections[44], [50].

Low-frequency electromagnetic induction (LFEMI) soil sensors operate in the low-frequency range (below 300 kHz) and are sensitive to magnetic susceptibility and electrical conductivity. They typically consist of one transmitter coil and one or more receiver coils. The depth and, consequently, the volume of sensitivity to the soil parameters corresponds to the intercoil separation, typically less than 2 m. In the low-frequency range, the in-phase component (relative to the transmitter voltage) of the receiver coil voltage depends on the magnetic susceptibility and the primary coupling between the coils. The quadrature component is linearly proportional to the soil electrical conductivity (typically below 1 S/m) but smaller by a few orders of magnitude than the in-phase component, which can be challenging from an instrumentation design perspective [84].

High-frequency electromagnetic induction (HFEMI) soil sensors operate in the frequency range from 3 MHz to 30 MHz. With the increasing excitation frequency, the sensitivity to electrical conductivity and dielectric permittivity increases, and the sensitivity to magnetic susceptibility remains constant. The geometry can be similar to the commercial LFEMI, with the inspection depth adequate for mapping the topsoil layer. With the increased excitation frequency, parasitic coupling within the sensor and the environment becomes noticeable, so special care must be taken in electrostatic shielding. Also, the low-induction number approximation is no longer valid, and the electrical conductivity affects both in-phase and quadrature components of the signal, complicating the signal analysis. Nevertheless, increased sensitivity to conductivity and permittivity allows simultaneous sensing of both electromagnetic parameters.

**Table 1** provides an overview of the contactless electromagnetic soil sensors operating in the frequency range below 30 MHz, including their most important features, frequency range, and measured electromagnetic parameters. Contactless modalities are capacitively coupled resistivity sensors and low-frequency and high-frequency EMI sensors. There are commercially available CCR and low-frequency EMI sensors, but no high-frequency EMI soil sensors are available for commercial use.

**Table 1.** Overview of the state-of-the-art proximal electromagnetic soil sensors operating below 30 MHz.

| Reference | Status | Modality | Frequency range | Measured parameters | Characteristics |
|---|---|---|---|---|---|
| Kuras2002[85] | Research | CCR | 14.2 kHz | Resistivity | Point electrodes, 1.5 m separation, measurement depth up to 3 m. |
| Flageul2013 [86] | Research | CCR | 122 Hz - 31 kHz | Resistivity | Point electrodes, 1 m and 2 m separation, measurement depth up to 10 m. |
| OhmMapper[33] | Commercial | CCR | 16.5 kHz | Resistivity | Line electrodes with lengths of 10 m to 20 m |
| Corim[33] | Commercial | CCR | 12 kHz | Resistivity | Point electrodes, 1.5 m separation |
| Manstein2015[63] | Research | Low-frequency EMI | 2.5 - 250 kHz | Conductivity | One transmitter and 2 receiver coils, intercoil separation of 1.5 m and 2.5 m, measurement depth up to 10 m. |
| EM38.MK2 [59] | Commercial | Low-frequency EMI | 14.6 kHz | Conductivity, susceptibility | One transmitter and 2 receiver coils, intercoil separation of 0.5 m and 1 m, measurement depth up to 1.5 m, depending on the orientation. |
| DUALEM[60] | Commercial | Low-frequency EMI | 9 kHz | Conductivity, susceptibility | One transmitter and multiple receiver coils, intercoil separation 1 to 8 m, measurement depth 0.3 to 8 m, depending on the configuration. |
| GEM-2[61] | Commercial | Low-frequency EMI | 90 Hz - 22 kHz | Conductivity, susceptibility | Intercoil separation 1.68 m, multi-frequency excitation. |
| Stewart1994[72], [77] | Research | High-frequency EMIo | 300 kHz - 30 MHz | Conductivity, permittivity | Variable intercoil separation between 0.5 and 5 m, measurement depth up to 10 m. |
| Kessouri2014[78] | Research | High-frequency EMIo | 1.56 MHz | Conductivity, permittivity | One transmitter and 1 receiver coil, 1.2 m intercoil separation, measurement depth up to 2.6 m. |
| Glaser2023[82] | Research | High-frequency EMI | 10 kHz to 20 MHz | Conductivity, permittivity | Overlapped transmitter and receiver coil. |

# 1.5 Contribution

The research deals with the determination of soil electromagnetic parameters (electrical conductivity and dielectric permittivity) using electromagnetic induction in the high-frequency range (from 3 MHz to 30 MHz). Low-frequency EMI sensors operate in the audio-frequency range and have high sensitivity to magnetic susceptibility and, to a lesser extent, electrical conductivity. In contrast, on the other side of the electromagnetic spectrum, from higher megahertz to low-gigahertz range, GPR is used to determine dielectric permittivity and, in rarer cases, electrical conductivity. High-frequency EMI sensors are sensitive to electrical conductivity and dielectric permittivity, which could bridge the gap between low-frequency EMI and GPR sensors, which are considered complementary modalities.

The objective of the research is to develop and experimentally verify a high-frequency electromagnetic induction method for the simultaneous determination of soil electrical conductivity and dielectric permittivity. The main research hypotheses are: 1) The high-frequency electromagnetic induction modality is suitable for the determination of soil electrical conductivity and dielectric permittivity, and it can be implemented using sensor geometry and electronic instrumentation suitable for portable use; 2.) It is possible to separate and determine the effects of soil electrical conductivity and dielectric permittivity by comparison of the high-frequency electromagnetic induction data and the results of a sensor model; 3.) Unwanted mechanical, temperature, and electromagnetic effects can be controlled and rejected by appropriate sensor geometry or the electronic instrumentation design.

The original scientific contribution of the dissertation is:

1.) Model-based method for measurement of electrical conductivity and dielectric permittivity of soil using high-frequency electromagnetic induction.

2.) Analysis of unwanted electromagnetic coupling and interference rejection techniques.

3.) Sensor geometry and electronic instrumentation for simultaneous measurement of soil electrical conductivity and dielectric permittivity using high-frequency electromagnetic induction.

## 1.5.1 Outline of the thesis

The thesis is structured as follows. Chapter 1 of the doctoral thesis ("Introduction") gives an overview of the soil sensing application and motivation. The heterogeneity of the soil is discussed, together with the relationship between the physical and chemical properties of the soil and soil electromagnetic properties (magnetic susceptibility, electrical conductivity, and dielectric permittivity). Extensive literature on the main approaches of electromagnetic soil sensing modalities for soil mapping is presented. This includes direct current resistivity, capacitively coupled resistivity, ground penetrating radar, and electromagnetic induction in low-frequency and high-frequency ranges. The chapter concludes with the objective, hypotheses, contribution, and outline of the thesis.

In Chapter 2 ("Analytical model") of the thesis, the analytical model of the high-frequency electromagnetic induction sensing approach is derived from the governing Maxwell's equations. The model includes a horizontal transmitter and perpendicular receiver coil above the two-layer homogeneous medium with electrical conductivity, dielectric permittivity, and magnetic susceptibility as parameters.

A design of the proposed high-frequency electromagnetic induction sensor is given in Chapter 3 ("Sensor design and electronic instrumentation"). For the generation of the excitation and the acquisition of a signal, the commercial vector network analyzer Keysight N991A was used. A printed circuit board coils with electrostatic shielding and the mutual perpendicular geometry were proposed. Furthermore, proprietary analog front-end electronics are described with the schematic and transfer functions of both transmitter and receiver filtering stages. Last, the laboratory measurement setup is described, together with the measurement procedure in which the sensor response was measured with and without the presence of the medium.

The analysis of the electromagnetic coupling, temperature, and mechanical influences was presented in Chapter 4 ("Analysis of unwanted electromagnetic coupling and interference rejection techniques"). Different factors were discussed theoretically or shown either experimentally or using the finite element method (FEM) model. The literature overview for the lift-off and temperature influences on the commercially available low-frequency EMI sensors was presented. The influence of the lift-off on the proposed HFEMI geometry was analyzed by the analytical model and experimentally in the laboratory for different electrical conductivity values and the lift-off. The influence of the temperature on the proposed HFEMI sensor was presented for measurements in the laboratory setting with the stable ambient temperature and for the field experiments when the sensor was under direct sunlight. The

influence of the mechanical misalignment was analyzed by FEM to obtain accurate small tilt angle changes and variations in both horizontal and vertical positions for the transmitter and receiver coil.

In the last part of Chapter 4, the literature overview of electrostatic shielding in high-frequency EMI applications was given, and the necessity of electrostatic shielding in HFEMI soil sensing was discussed. The method to evaluate the effectiveness of the electrostatic shielding of HFEMI soil sensor was proposed and demonstrated for several designs of PCB shields. The method is based on the fact that the inductive and capacitive coupling are out of phase. By measuring the primary coupling of the sensor and using a linearized equivalent circuit model, it is possible to estimate the inductance and the capacitance between the transmitter and receiver. From this approach, the configuration of a shielded PCB transmitter and receiver was chosen for further experimental validation.

The measurement results of the proposed HFEMI sensor are presented in Chapter 5 ("Results"). The sensor was evaluated in the laboratory and in two separate field experiments. In the laboratory part of the study, sensitivities to electrical conductivity and dielectric permittivity were analyzed for the range typical for soils. A container filled with deionized water was used, and salt was added to control electrical conductivity. Dielectric permittivity was varied by adding sucrose to the deionized water in the first experiment and by varying the water volume in the container in the second experiment.

Additionally, FEM analysis was made to compare the results. The FEM model was similar to the experimental setup, with the difference that the coils were modeled without the shields. Both laboratory measurements and FEM results agreed quantitatively and demonstrated the possibility of simultaneous sensing of electrical conductivity and dielectric permittivity. In the field part of the study, the sensor was placed on two similar soil patches. One was irrigated with deionized water and the other with saline water.

In Chapter 6 ("Conclusions"), the conclusions of each chapter were summarized together with the notes for future work.

# Chapter 2

# Analytical model

The analytical model of the high-frequency electromagnetic induction sensing approach is derived from the governing Maxwell's equations, in differential form given as:

$$\nabla \cdot \mathbf{D} = \rho, \tag{40}$$

$$\nabla \cdot \mathbf{B} = 0, \tag{41}$$

$$\nabla \times \mathbf{E} = -\frac{\partial \mathbf{B}}{\partial t}, \tag{42}$$

$$\nabla \times \mathbf{H} = \mathbf{J} + \frac{\partial \mathbf{D}}{\partial t}, \tag{43}$$

where $\mathbf{E}$ is the electric field intensity (V/m), $\mathbf{B}$ is the magnetic flux density (T), $\mathbf{D}$ is the dielectric displacement (C/m$^2$), $\mathbf{H}$ is the magnetic field intensity in (A/m), and $\mathbf{J}$ is the current density (A$^2$/m). For the homogeneous, isotropic and linear media, the above equations are coupled through the constitutive equations:

$$\mathbf{D} = \varepsilon \mathbf{E}, \tag{44}$$

$$\mathbf{B} = \mu \mathbf{H}, \tag{45}$$

$$\mathbf{J} = \sigma \mathbf{E}, \tag{46}$$

with $\varepsilon$, $\mu$, and $\sigma$ being dielectric permittivity, magnetic permeability, and electrical conductivity, respectively.

The above equations can be solved in the form of magnetic vector potential $\mathbf{A}$. The scalar potential $\Phi$ is set to $\Phi=0$, as there is no charge accumulation in the source, the characteristic dimensions of the problem are still much smaller than the wavelength of the excitation

frequency, and the propagation can be considered instantaneous [87]. The magnetic and electric field strength can be expressed as:

$$\mathbf{B} = \nabla \times \mathbf{A}, \tag{47}$$

$$\mathbf{E} = -\frac{\partial \mathbf{A}}{\partial t}. \tag{48}$$

For the case when the propagation is neglected, the Coulomb gauge is used in which the divergence of the magnetic potential is zero:

$$\nabla \cdot \mathbf{A} = 0, \tag{49}$$

and $\mathbf{E}$ can then be separated by Helmholtz decomposition into the irrotational component $\mathbf{E}_{irr}$ and rotational component $\mathbf{E}_{rot}$ as $\mathbf{E}=\mathbf{E}_{irr}+\mathbf{E}_{rot}$ with satisfied conditions $\nabla \times \mathbf{E}_{irr} = 0$ and $\nabla \cdot \mathbf{E}_{rot} = 0$. The both parts of $\mathbf{E}$ are defined as:

$$\mathbf{E}_{irr} = -\nabla \Phi, \tag{50}$$

$$\mathbf{E}_{rot} = -\frac{\partial \mathbf{A}}{\partial t}. \tag{51}$$

Since the scalar potential is zero, in further discussion, only the rotational part of the $\mathbf{E}$ is considered, i.e. $\mathbf{E} = \mathbf{E}_{rot}$.

The wave equation for $\mathbf{A}$ is

$$\nabla^2 \mathbf{A} - \mu \varepsilon \frac{\partial^2 \mathbf{A}}{\partial t^2} = -\mu \mathbf{J}, \tag{52}$$

and for the case without free sources

$$\mathbf{J} = \sigma \mathbf{E} = -\sigma \frac{\partial \mathbf{A}}{\partial t}. \tag{53}$$

In the frequency domain with $\partial/\partial t = j\omega$

$$\nabla^2 \mathbf{A} + \omega^2 \mu \varepsilon \mathbf{A} = j\omega\mu\sigma \mathbf{A}, \tag{54}$$

$$\nabla^2 \mathbf{A} = k^2 \mathbf{A}, \tag{55}$$

With $k$ being the wave number defined as

$$k^2 = -\omega^2 \mu \varepsilon + j\omega\mu\varepsilon = j\omega\mu(\sigma + j\omega\varepsilon). \tag{56}$$

The equation in the cylindrical coordinate system is

$$\mathbf{A}(r,\varphi,z) = A_r \hat{r} + A_\varphi \hat{\varphi} + A_z \hat{z}. \tag{57}$$

As the coil is circular and symmetrical, there are no $\hat{r}$ and $\hat{z}$ components, but only $\varphi$ component, the vector Laplacian $\nabla^2 \mathbf{A}(r,\varphi,z)$ comes down to scalar form

$$\nabla^2 A(r,z)\varphi = \frac{1}{r}\frac{\partial}{\partial r}\left(r\frac{\partial A}{\partial r}\right)+\frac{1}{r^2}\frac{\partial^2 A}{\partial \varphi^2}+\frac{\partial^2 A}{\partial z^2}, \tag{58}$$

and the Helmholtz equation is then

$$\frac{1}{r}\frac{\partial}{\partial r}\left(r\frac{\partial A}{\partial r}\right)+\frac{1}{r^2}\frac{\partial^2 A}{\partial \varphi^2}+\frac{\partial^2 A}{\partial z^2}-k^2 A = 0. \tag{59}$$

By introducing the separation of the variables

$$A(r,z) = R(r)\cdot Z(z), \tag{60}$$

the equation (59) becomes

$$\frac{1}{R}\frac{1}{r}\frac{\partial}{\partial r}\left(r\frac{\partial R}{\partial r}\right)-\frac{1}{r^2} = -\frac{1}{Z}\frac{\partial^2 Z}{\partial z^2}+k^2. \tag{61}$$

Both sides of the equation (61) are equal to $\alpha^2$, leading to

$$\frac{1}{R}\frac{1}{r}\frac{\partial}{\partial r}\left(r\frac{\partial R}{\partial r}\right)-\frac{1}{r^2} = -\alpha^2, \tag{62}$$

$$-\frac{1}{Z}\frac{\partial^2 Z}{\partial z^2}+k^2 = -\alpha^2, \tag{63}$$

which, after arranged, becomes

$$\frac{\partial^2 R}{\partial r^2}+\frac{1}{r}\frac{\partial R}{\partial r}+\left(\alpha^2-\frac{1}{r^2}\right)R = 0, \tag{64}$$

$$\frac{\partial^2 Z}{\partial z^2}-\beta^2 Z = 0, \tag{65}$$

with

$$\beta^2 = \alpha^2 +k^2. \tag{66}$$

The equation (64) is Bessel's differential equation, whose general form is

$$R(r) = A\cdot J_\nu(\alpha r)+B\cdot Y_\nu(\alpha r) \tag{67}$$

where $J_\nu(\alpha r)$ and $Y_\nu(\alpha r)$ are Bessel's functions of the first and second kind, respectively.

The general solution of the differential equation (65) is

$$Z(z) = C\cdot \exp(-\beta z)+D\cdot \exp(\beta z). \tag{68}$$

By substituting equations (67) and (68) into (60), the expression for magnetic potential is

$$A(r,z) = C\cdot \exp(-\beta z)+D\cdot \exp(\beta z)\cdot J_1(\alpha r), \tag{69}$$

The total solution for A is obtained for each $\alpha$, which is a continuous variable, and $i$ denominate material region

$$A_i(r,z,r_0,z_0) = \int_0^\infty D_i \cdot \exp(\beta_i z) + C_i \cdot \exp(-\beta_i z) \cdot J_1(\alpha r) d\alpha. \tag{70}$$

For the circular symmetrical coil in the air above the double-layer medium, the problem is divided into 4 regions, **Figure 3**.
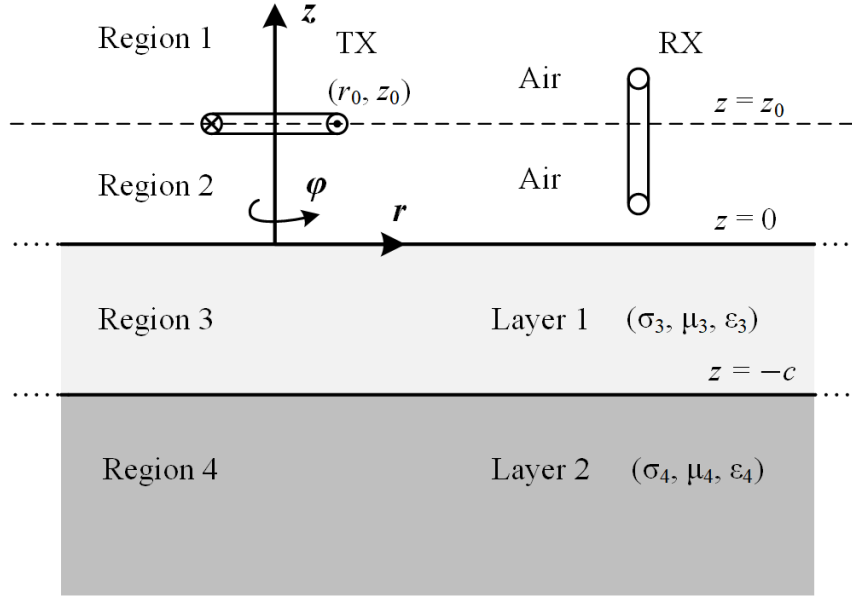


**Figure 3.** Analytical model of the transmitter (TX) and receiver (RX) coil above double-layered medium.

The integral solutions of A for each region are

$$A_1(r,z) = \int_0^\infty C_1 \cdot \exp(-\beta z) \cdot J_1(\alpha r) \cdot d\alpha, \tag{71}$$

$$A_2(r,z) = \int_0^\infty C_2 \cdot \exp(-\beta z) + D_2 \cdot \exp(\beta z) \cdot J_1(\alpha r) \cdot d\alpha, \tag{72}$$

$$A_3(r,z) = \int_0^\infty C_3 \cdot \exp(-\beta_3 z) + D_3 \cdot \exp(\beta_3 z) \cdot J_1(\alpha r) \cdot d\alpha, \tag{73}$$

$$A_4(r,z) = \int_0^\infty D_4 \cdot \exp(\beta_4 z) \cdot J_1(\alpha r) \cdot d\alpha. \tag{74}$$

The coefficients $C_1$, $C_2$, $D_2$, $C_3$, $D_3$, and $D_4$ are determined from the boundary conditions

$$\hat{n} \times (\mathbf{H}_{i+1} - \mathbf{H}_i) = \mathbf{J}, \tag{75}$$

$$(\mathbf{B}_{i+1} - \mathbf{B}_i) \cdot \hat{n} = 0, \tag{76}$$

with $\hat{n} = -\hat{z}$. Combining boundary conditions with (47), (57) gives

$$\nabla \times \mathbf{A} = \nabla \times (A\hat{\varphi}) = -\frac{\partial A}{\partial z}\hat{r} + \frac{1}{r}\frac{\partial(rA)}{\partial r}\hat{z}, \tag{77}$$

and with

$$\mathbf{B} = \mu_i \mathbf{H}, \tag{78}$$

provides general boundary conditions equations as

$$\frac{1}{\mu_{i+1}} \frac{\partial A_{i+1}}{\partial z} - \frac{1}{\mu_i} \frac{\partial A_i}{\partial z} = \begin{cases} 0, \\ \mu_0 I \delta(r - r_0) \delta(z - z_0) \end{cases}, \tag{79}$$

$$\frac{\partial A_{i+1}}{\partial r} + \frac{A_{i+1}}{r} - \frac{\partial A_i}{\partial r} - \frac{A_i}{r} = 0. \tag{80}$$

The coil is at the boundary 1-2 at the height z = $z_0$ with the uniform excitation current, so the right side of the equation (79) is $\mu_0 I \delta(r - r_0) \delta(z - z_0)$. The boundary 2-3 is at height z=0, and 3-4 is at height z=−c, and there is no current, so the right side of the equation (79) is 0. From these, the equations to determine coefficients are:

$$\exp(-\beta z_0) C_1 - \exp(-\beta z_0) C_2 - \exp(\beta z_0) D_2 = 0, \tag{81}$$

$$\beta \exp(-\beta z_0) C_1 - \beta \exp(-\beta z_0) C_2 + \beta \exp(\beta z_0) D_2 = \mu_0 I \alpha r_0 J_1(\alpha r_0), \tag{82}$$

$$C_2 + D_2 - C_3 - D_3 = 0, \tag{83}$$

$$\beta C_2 - \beta D_2 - \frac{\beta_3}{\mu_3} C_3 + \frac{\beta_3}{\mu_3} D_3 = 0, \tag{84}$$

$$\exp(\beta_3 c) C_3 + \exp(-\beta_3 c) D_3 - \exp(-\beta_4 c) D_4 = 0, \tag{85}$$

$$\frac{\beta_3}{\mu_3} \exp(\beta_3 c) C_3 - \frac{\beta_3}{\mu_3} \exp(-\beta_3 c) D_3 + \frac{\beta_4}{\mu_4} \exp(-\beta_4 c) D_4 = 0. \tag{86}$$

The coefficients $C_1$, $C_2$, $D_2$, $C_3$, $D_3$, and $D_4$ are

$$C_1 = RD_2 + \frac{1}{2\beta} \mu_0 I \alpha r_0 J(\alpha r_0) \exp(\beta z_0), \tag{87}$$

$$C_2 = RD_2, \tag{88}$$

$$D_2 = \frac{1}{2\beta} \mu_0 I \alpha r_0 J_1(\alpha r_0) \exp(-\beta z_0), \tag{89}$$

$$C_3 = \frac{2\mu_3 \beta \ \mu_4 \beta_3 - \mu_3 \beta_4 \ \exp(-2\beta_3 c)}{Q} D_2, \tag{90}$$

$$D_3 = \frac{2\mu_3 \beta \ \mu_4 \beta_3 + \mu_3 \beta_4}{Q} D_2, \tag{91}$$

$$D_4 = \frac{4\mu_3 \mu_4 \beta \beta_3 \exp(-\beta_3 c) \exp(\beta_4 c)}{Q} D_2, \tag{92}$$

$$R = \frac{P}{Q} = \frac{\mu_3\beta - \beta_3 \quad \mu_4\beta_3 + \mu_3\beta_4 \ + \ \mu_3\beta + \beta_3 \quad \mu_4\beta_3 - \mu_3\beta_4 \ \exp(-2\beta_3 c)}{\mu_3\beta + \beta_3 \quad \mu_4\beta_3 + \mu_3\beta_4 \ + \ \mu_3\beta - \beta_3 \quad \mu_4\beta_3 - \mu_3\beta_4 \ \exp(-2\beta_3 c)}, \qquad (93)$$

and R is the total reflection coefficient.

In the above expressions, the coil excitation is a delta function for the single $r$ and $z$ coordinates. A coil with the real cross-section is approximated by the superposition of the delta-function excitations. The coil with a square cross-section is shown in **Figure 4**.
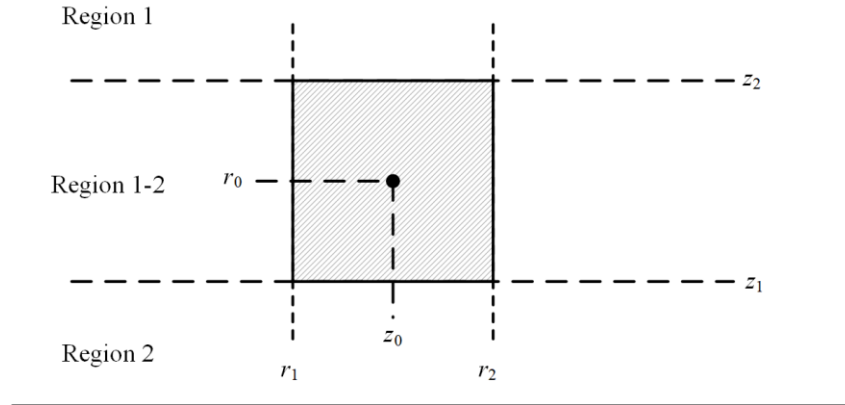


**Figure 4**. Square cross-section of the TX coil Transmitter coil.

The current density $i_T$ is assumed to be constant over the coil dimensions, given as

$$i_T = \frac{NI}{(r_2 - r_1)(z_2 - z_1)} \qquad (94)$$

where $N$ is the number of coil turns. As the coefficients depend on $r$ and $z$, the total coefficient $D_2$ is then integrated over r and z, and the $D_2$' is given as:

$$D_2^{'} = \int_{r_1}^{r_2}\int_{z_1}^{z_2} \frac{1}{2\beta}\mu_0 I\alpha r_0 J_1(\alpha r_0)\exp(-\beta z_0)dr_0 dz_0. \qquad (95)$$

That becomes

$$D_2^{'} = \frac{1}{2}\mu_0 i_T \frac{\chi(\alpha r_1, \alpha r_2)}{\beta^2\alpha} \ \exp(-\beta z_1) - \exp(-\beta z_2) \ , \qquad (96)$$

and $\chi(\alpha r_1, \alpha r_2)$ is a finite integral of the Bessel function, expressed as

$$\chi(x_1, x_2) = \int_{x_1}^{x_2} xJ_1(x)dx = x\frac{\pi}{2} \ J_0(x)\mathbf{H}_1(x) - J_1(x)\mathbf{H}_0(x) \ \Big|_{x_1}^{x_2}, \qquad (97)$$

with $\mathbf{H}_n$ denoting the Struve function of the order $n$ [88].

The coefficient $C_1$ becomes $C_1$'

$$C_1^{'} = RD_2^{'} + \frac{1}{2}\mu_0 i_T \frac{\chi(\alpha r_1, \alpha r_2)}{\beta^2\alpha} \ \exp(\beta z_2) - \exp(-\beta z_1) \ . \qquad (98)$$

The rest of the coefficients from (87) to (93) can be expressed through $D_2$'.

The magnetic potential $A_{12}$ at the border of regions 1 and 2 is the sum of all sources in the coil, given that the current through the cross section is uniform:

$$A_{12}(r,z) = \int_0^\infty \left( \int_{r_1}^{r_2} \int_{z_1}^{z} A_1\left(r,z,r_0,z_0\right) dr_0 dz_0 + \int_{r_1}^{r_2} \int_{z}^{z_2} A_2\left(r,z,r_0,z_0\right) dr_0 dz_0 \right) d\alpha, \tag{99}$$

$$A_{1-2}\left(r,z\right) = \int_0^\infty RD_2' \exp(-\beta z)J_1\left(\alpha r\right) d\alpha +$$

$$\int_0^\infty \frac{1}{2} \mu_0 i_T \frac{\chi(\alpha r_1, \alpha r_2)}{\beta^2 \alpha} \left(2 - \exp(\beta z_1)\exp(-\beta z) - \exp(-\beta z_2)\exp(\beta z)\right) J_1\left(\alpha r\right) d\alpha. \tag{100}$$

The induced voltage $U$ in the coil is obtained by solving a line integral of the electric field $\mathbf{E}$ over the length of the transmitter and receiver coil, respectively:

$$U = -\oint \mathbf{E} d\mathbf{l}, \tag{101}$$

and $\mathbf{E}$ is

$$\mathbf{E} = -\frac{d\mathbf{A}}{dt}. \tag{102}$$

In the frequency domain, the induced voltage is

$$U = j\omega \oint \mathbf{A} d\mathbf{l}, \tag{103}$$

and in the cylindrical coordinates, $A$ has only $\hat{\varphi}$ component, while $d\boldsymbol{l}$ is

$$d\mathbf{l} = \hat{r}dr + r\hat{\varphi}d\varphi + \hat{z}dz. \tag{104}$$

For the sake of more convenient implementation, the expressions were transformed from cylindrical to cartesian coordinates, and $\hat{\varphi}$ component of $A$ was transformed into $\hat{x}$ and $\hat{y}$ so the expression for the induced voltage of the receiver becomes

$$U = j\omega \oint A\left( -\frac{A\cos\varphi}{r}dx + \frac{A\sin\varphi}{r}dy \right), \tag{105}$$

in which $A$ depends on the region in which the coil is positioned. The integral is calculated as the sum of the discrete linear segments which approximate the loop. The induced voltage is calculated for a single closed loop, and for the multi-turn coil, the total induced voltage is the superposition of each single closed loop.

The sensor output is expressed as the secondary to primary induced voltage ratio. In free space, i.e., in the absence of the soil, the primary coupling between the coils of an EMI sensor induces the primary voltage in the receiver coil:

$$U_P = Z_T I_{TX} = j\omega M_P I_{TX}, \tag{106}$$

where $Z_T$ is the transimpedance of the transmit-receive pair of coils, $M_P$ is the primary mutual inductance, and $I_{TX}$ is the transmitter current. In the presence of the soil, the receiver voltage is a superposition of $U_P$ and the secondary component $U_S$ due to the coupling with the soil and the change in the transimpedance $\Delta Z_T$:

$$U_S = \Delta Z_T I_{TX}. \tag{107}$$

It can be shown by using the Lorentz reciprocity theorem that the change $\Delta Z_T$ due to the presence of the soil is

$$\Delta Z_T = \frac{j\omega}{I_{TX}^2} \int_V \left( (\mu - \mu_0) \mathbf{H}_a \mathbf{H}_b - \left( \varepsilon - \varepsilon_0 + \frac{\sigma}{j\omega} \right) \mathbf{E}_a \mathbf{E}_b \right) dV, \tag{108}$$

where the integration is over the entire measured soil volume $V$. In (108), magnetic field $\mathbf{H}_a$ and electric field $\mathbf{E}_a$ are the fields for the case without the soil, i.e., the sensor in free space, and $\mathbf{H}_b$ and $\mathbf{E}_b$ are the fields for the case with the soil. Assuming that the electromagnetic parameters are small enough, the Born approximation can be used to make the assumptions $\mathbf{H}_b \approx \mathbf{H}_a$ and $\mathbf{E}_b \approx \mathbf{E}_a$. The spatially dependent $\mu$, $\sigma$, and $\varepsilon$ can be replaced with effective or apparent electromagnetic properties of equivalent homogenous medium $\mu_{eff}$, $\sigma_{eff}$, and $\varepsilon_{eff}$, defined in (6) and (7) . These simplifications and the quasi-stationary relationship between the electric field and vector magnetic potential, $\mathbf{E} = -j\omega\mathbf{A}$, result in

$$\Delta Z_T = \frac{j\omega}{I_{TX}^2} \left( (\mu_{eff} - \mu_0) \int_V |\mathbf{H}_a|^2 \, dV - \left( \varepsilon_{eff} - \varepsilon_0 + \frac{\sigma_{eff}}{j\omega} \right) \omega^2 \int_V |\mathbf{A}_a|^2 \, dV \right). \tag{109}$$

From (106), (107) and (109) the ratio of the secondary component to the primary component of the total induced receiver voltage is:

$$\frac{U_S}{U_P} = \frac{\Delta Z_T}{Z_T} = \frac{1}{M_P} \left( (\mu_{eff} - \mu_0) \int_V \left| \frac{\mathbf{H}_a}{I_{TX}} \right|^2 dV - j\sigma_{eff}\omega \int_V \left| \frac{\mathbf{A}_a}{I_{TX}} \right|^2 dV - (\varepsilon_{eff} - \varepsilon_0)\omega^2 \int_V \left| \frac{\mathbf{A}_a}{I_{TX}} \right|^2 dV \right). \tag{110}$$

The quantities $M_P$, $\mathbf{H}_a / I_{TX}$, and $\mathbf{A}_a / I_{TX}$ are computed for the sensor in free space and are solely determined by the sensor's geometry. Being unaffected by the soil properties and the excitation frequency, they determine the sensor sensitivities to the soil electromagnetic parameters [89], [90]. Sensitivity to soil permeability (or susceptibility) is frequency-independent, whereas sensitivities to soil conductivity and permittivity increase linearly and quadratically, respectively, with the excitation frequency. This distinction is crucial, as high frequencies render sensitivity to permeability negligible, while it becomes a dominant factor at lower frequencies.

## 2.1 Results of the analytical model

The analytical model results were calculated in Matlab as the induced voltage $U$ of the receiver coil in the air and above the medium. The characteristic dimensions of the setup, coil dimensions, and position were chosen to be the same as in the experimental setup explained in Chapter 3. The results are shown in the complex plane as the secondary to primary induced voltage $U_S/U_P$ ratio. The thickness of the first layer (region 3), **Figure 3**, was set to 5 cm to obtain the sensor response in the order of magnitude similar to laboratory measurements and FEM due to the smaller inspected volume, and the second layer (region 4) was set to air. The electrical parameters of the first layer were in the range of 0.01 mS/m to 300 mS/m for electrical conductivity and from 1 to 78 for relative permittivity. Electrical conductivity varied in 11 steps, and dielectric permittivity varied in 10 steps. Each combination of conductivity and permittivity was calculated for a total of 110 points. The results are calculated for the excitation frequency of 5 MHz in **Figure 5**, 20 MHz in **Figure 6**, and 30 MHz in **Figure 7**.
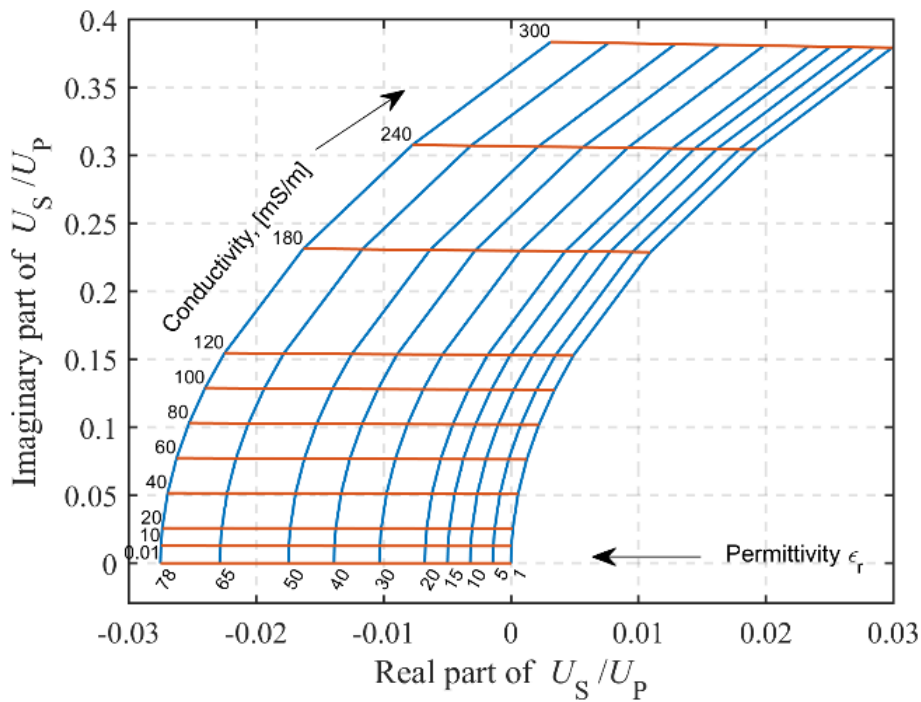


**Figure 5**. Analytical model results for sensor response $U_S/U_P$ depending on the conductivity and permittivity at 5 MHz
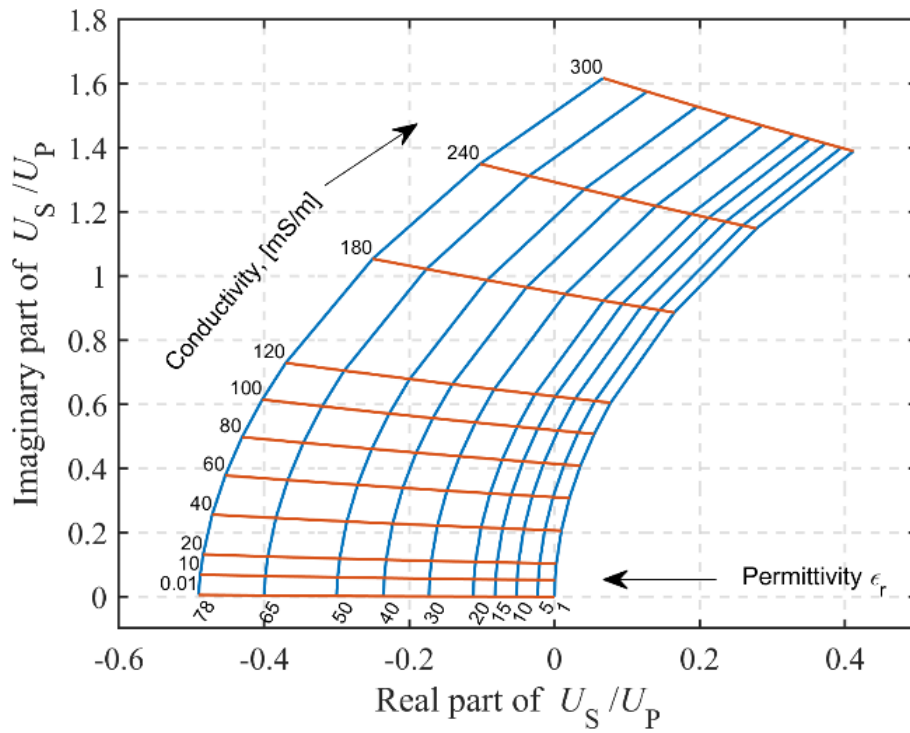
**Figure 6.** Analytical model results for sensor response $U_S/U_P$ depending on the conductivity and permittivity at 20 MHz
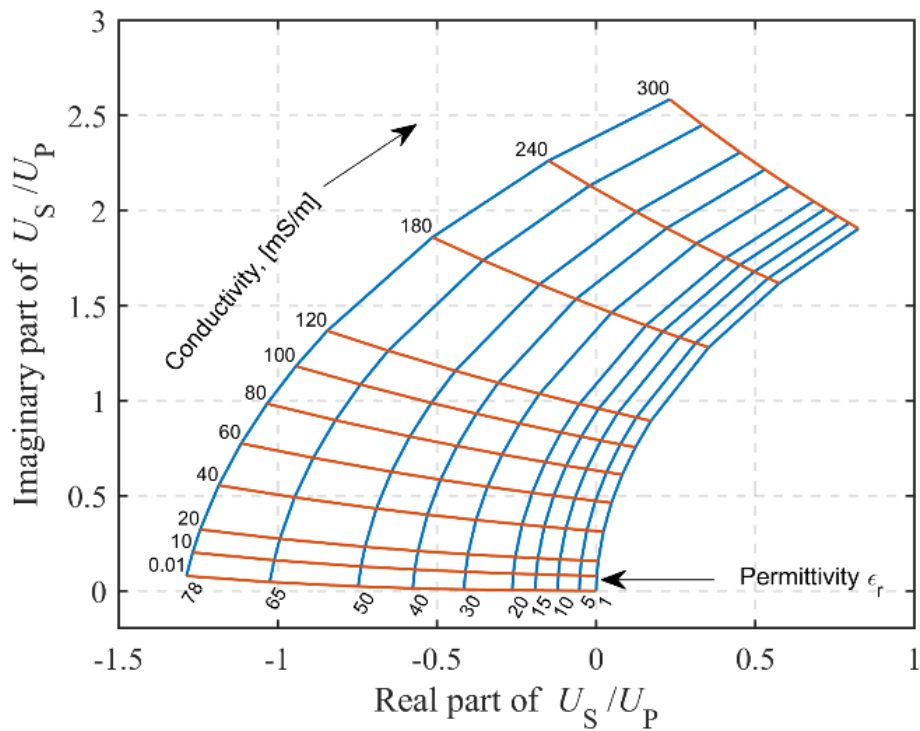


**Figure 7.** Analytical model results for sensor response $U_S/U_P$ depending on the conductivity and permittivity at 30 MHz.

In all cases, red lines show results for constant conductivity with varied permittivity and blue lines for constant permittivity with varied electrical conductivity. The change in dielectric

permittivity dominantly affects the real part of the $U_S/U_P$ for all frequencies. In the case of 5 MHz, **Figure 5**, the influence of electrical conductivity dominantly affects the imaginary part of $U_S/U_P$. For 20 MHz and 30 MHz, **Figure 6** and **Figure 7**, respectively, the imaginary part of $U_S/U_P$ is dominantly changed for low conductivity values (below approximately 100 mS/m). For higher electrical conductivity values both real and imaginary parts of $U_S/U_P$ are affected as the low-induction number approximation is no longer valid.

# Chapter 3

# Sensor design and electronic instrumentation

The designed sensor system consists of a transmitter and receiver, analog electronic circuitry for signal amplification and filtering, and a network analyzer Keysight Fieldfox 9913A. The electronics and the network analyzer are battery-powered and isolated from the ground. The block diagram of the sensor system is shown in **Figure 8**. The vector network analyzer (VNA) is used for generating the excitation signal and the acquisition of the signal, while the rest of the signal processing was done offline on the PC in Matlab.
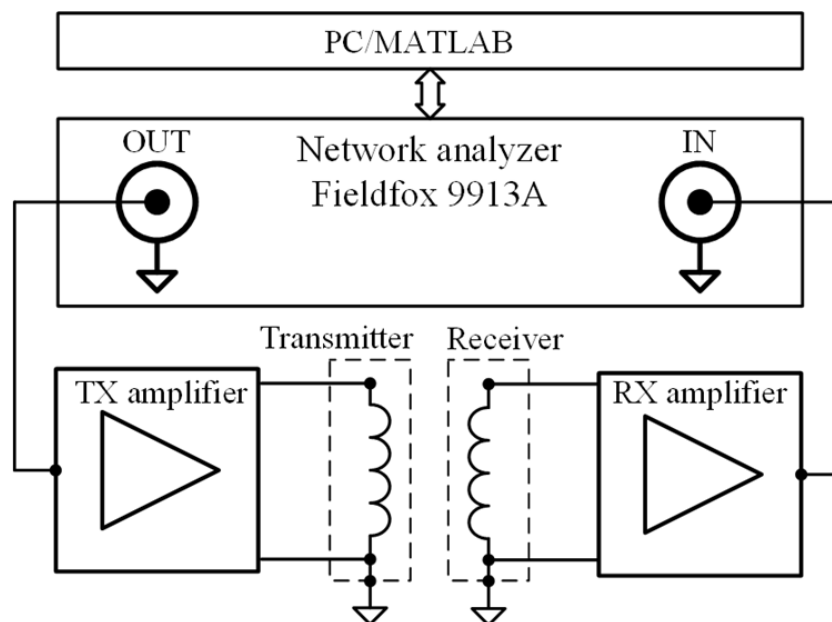


**Figure 8**. Block diagram of the sensor system.

# 3.1 Coils and shielding design

The transmitter and receiver incorporate printed circuit board (PCB) coils and a PCB shield above and below each coil. The thickness of the FR-4 substrate for PCB was 0.8 mm to reduce coil self-capacitance and maintain the mechanical integrity of both coils and shields. The transmitter coil has 3 turns, and the receiver coil has 4 turns, **Figure 9**(a) and **Figure 9**(b). The outer diameter of both coils is 70 mm, with the inter-turn spacing of 3.5 mm and the copper trace width of 0.8 mm. The coil self-capacitance increases with the coil diameter and number of turns, so the needed resonant frequency and sensor geometry determine the dimensions of the coils. With a small number of turns, the obtained resonant frequency of both transmitter and receiver coils is approximately 70 MHz, which is further reduced when shielding is added due to the coil-shield capacitance.

Two different shield patterns were designed and evaluated: C-pattern and X-pattern, **Figure 10**(a) and **Figure 10**(b). Dimensions of both shield designs are 87.5 mm x 77.5 mm, the copper trace width is 0.5 mm, and the spacing between traces is 1.5 mm. The shielding patterns are designed to minimize conductive surface, and the etched PCB traces don't form inductive loops, thus reducing the inductive losses while maintaining the ability to reduce capacitive coupling. All traces have the same potential and are connected to the reference potential of the coil in a star topology. Depending on the configuration, the spacing between the shields and coil can be set to 2 mm, 4 mm, or 6 mm using plastic distancers.



(a)                                                                        (b)

**Figure 9.** PCB coils: (a) Transmitter coil, (b) Receiver coil.

(a)            (b)
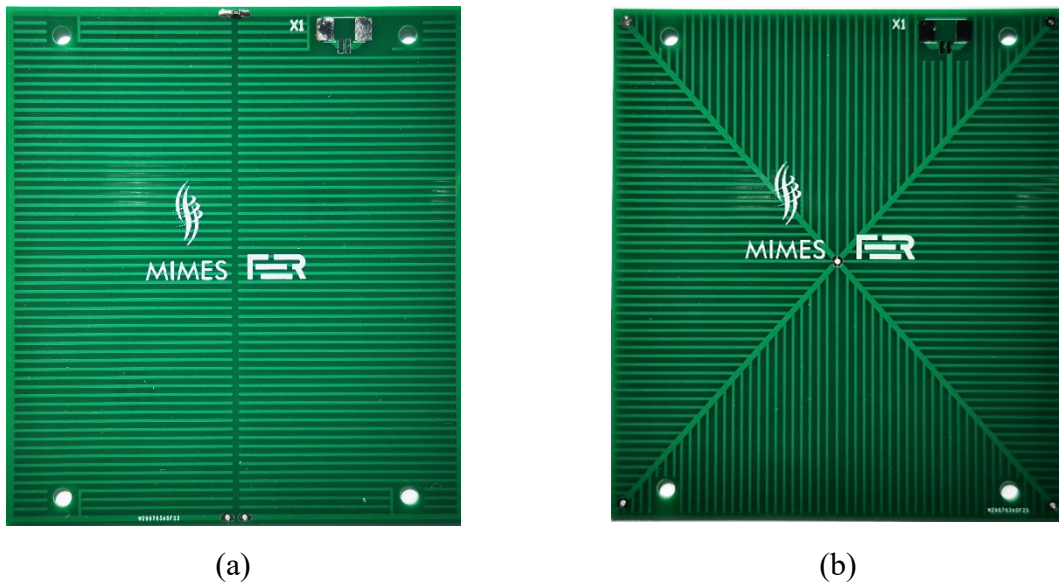
**Figure 10.** PCB shields: (a) C-pattern, (b) X-pattern.

## 3.2 Electronics design

The electronic instrumentation consists of a proprietary analog front-end circuitry connected to the transmitter and receiver, a battery power supply, and the network analyzer Keysight Fieldfox 9913A for signal generation and acquisition. The device is handheld and battery-powered, so it is fully isolated from the ground, like the rest of the circuitry. The excitation signal has a square wave shape, and the acquired signal is digitized with the 14-bit analog-to-digital converter.

The excitation signal from the network analyzer is fed into the transmitter amplifier, which consists of a 4th-order low-pass filter with a cutoff frequency of 35 MHz and the power amplifier. The amplifier and transmitter are connected with a coaxial cable of 20 cm in length. The transmitter low-pass filter filters the square wave excitation signal from the network analyzer so that the higher harmonics will not saturate the receiver amplifier. The schematic of the transmitter circuitry is shown in **Figure 11**, and the transfer function measured with a network analyzer as magnitude and phase is shown in **Figure 12**.
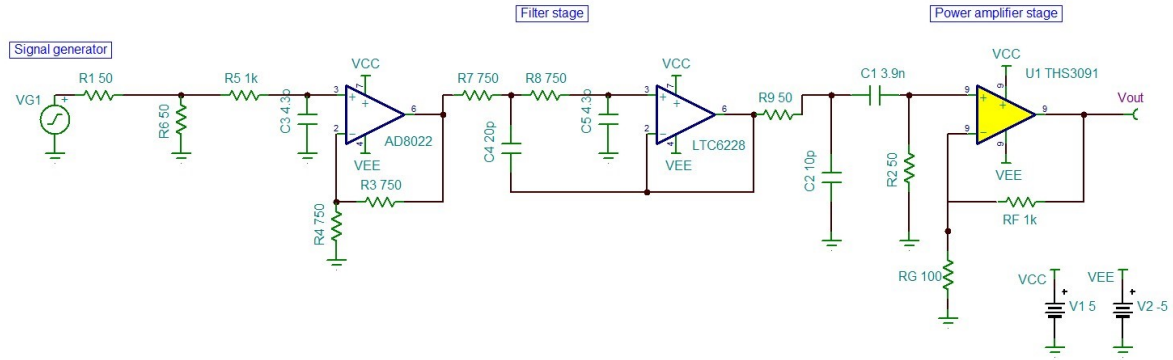
**Figure 11**. Schematic of the transmitter filter.



(a)

(b)
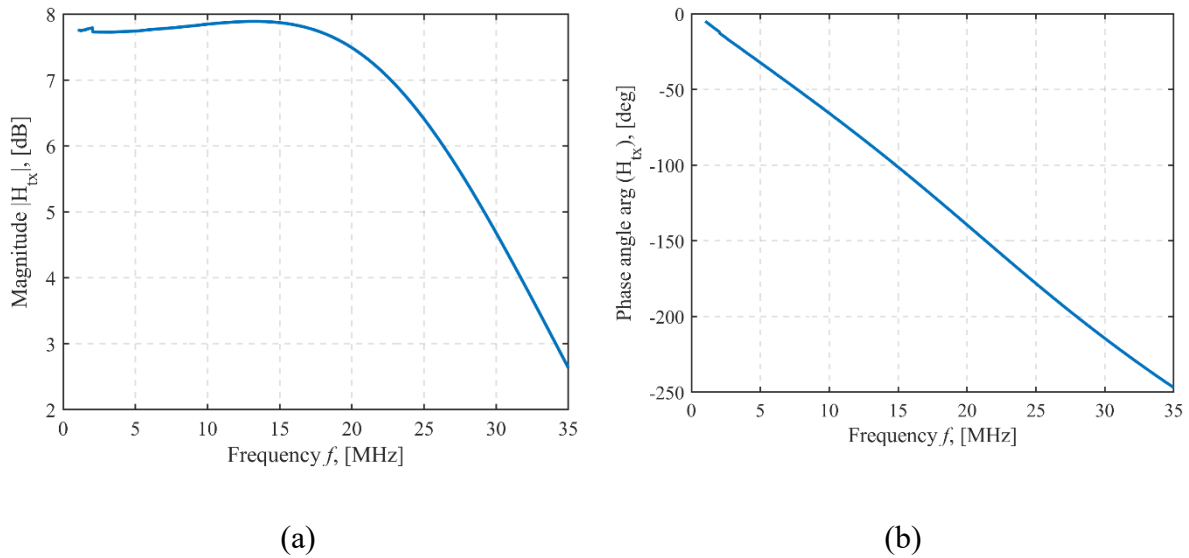
**Figure 12.** Transmitter circuitry measured transfer function: (a) magnitude and (b) phase angle.

The receiver buffer is connected to the receiver coil through the SMA connector to avoid the additional cable capacitance that would lower the coil resonant frequency. The schematic of the receiver buffer is shown in **Figure 13**. The output of the receiver buffer is connected to the second and third amplifier stages, which are positioned further from the transmitter and receiver, as shown in **Figure 14** and **Figure 15**, respectively. The output of the third stage is connected to the vector analyzer. The transfer function of the receiver chain is shown in **Figure 16**. The total gain of the receiver chain is approximately 48 dB with a cutoff frequency of 35 MHz, ensuring that only the induced coil voltage is amplified and high-frequency interference suppressed.
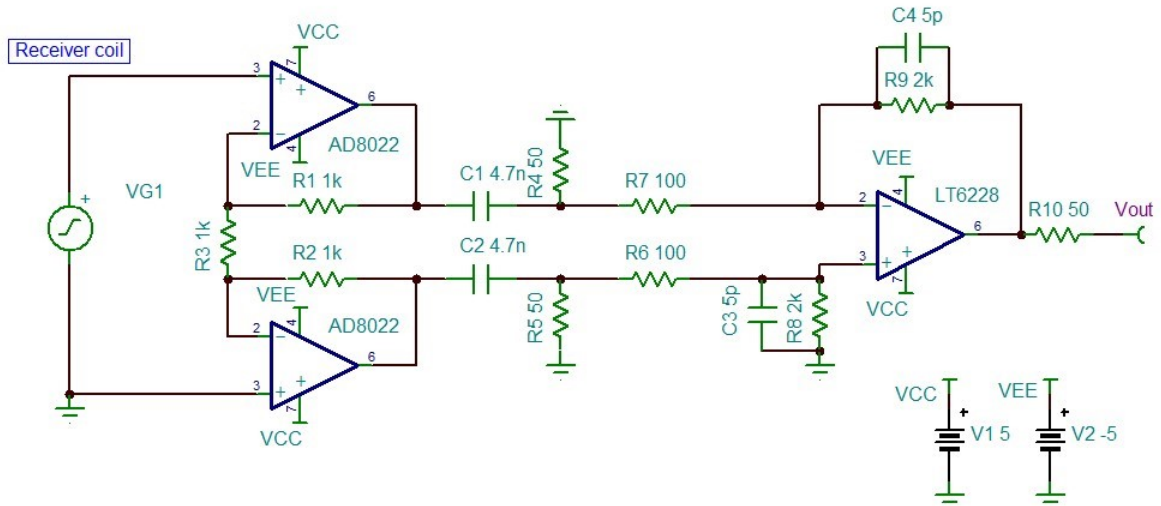
**Figure 13.** Schematics of the receiver buffer board.
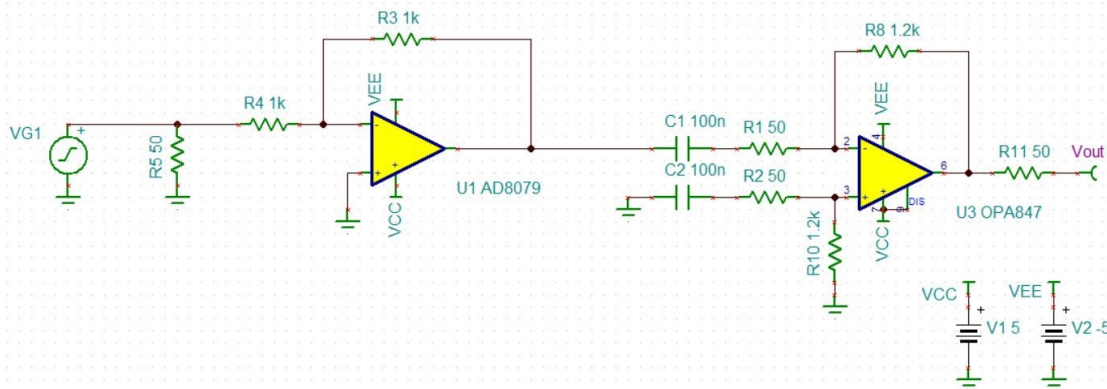
**Figure 14.** Schematic of the second stage receiver amplifier chain.
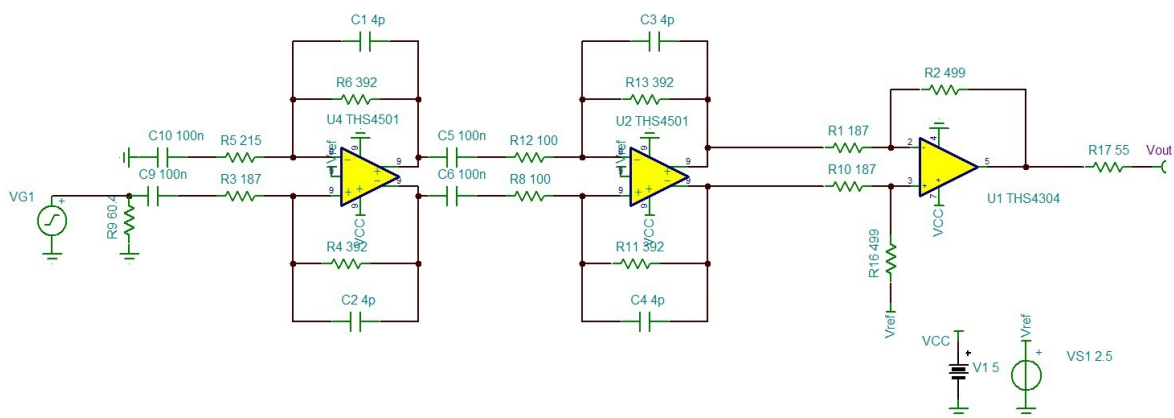
**Figure 15.** Schematic of the third stage receiver amplifier chain.

(a) (b)
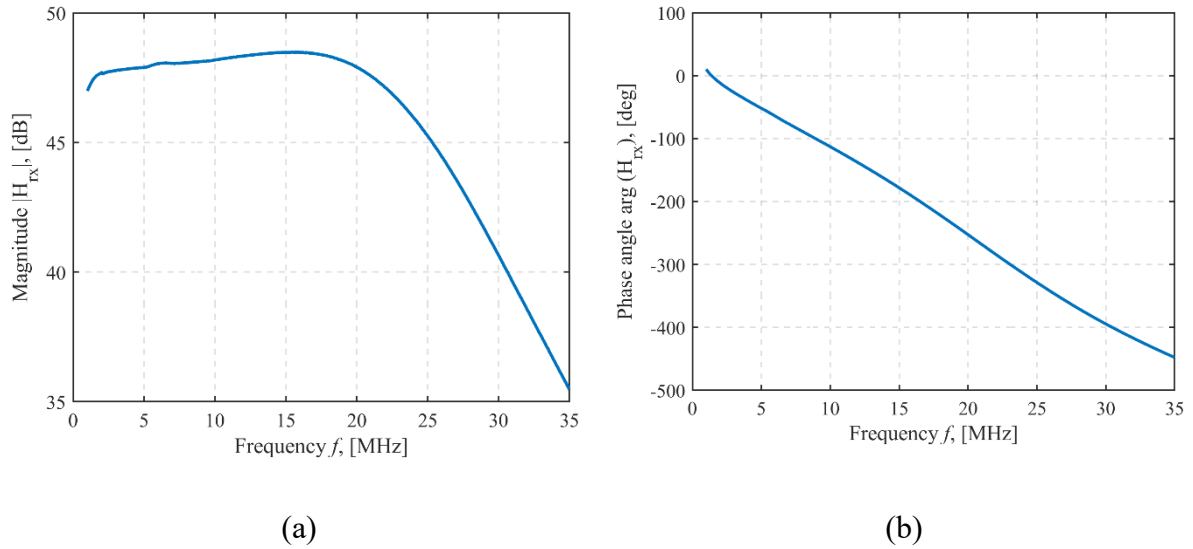
**Figure 16.** Receiver circuitry measured transfer function $H_{rx}$: (a) magnitude and (b) phase

The sensor and electronics are mounted on a wooden stationary stand to avoid the influences of any conductive parts. The intercoil separation, measured from the center of the transmitter coil to the center of the receiver coil, is set to 37 cm and can also be set to 27 cm.

## 3.3 Measurement setup

The photograph of the measurement setup is shown in **Figure 17**. The sensor and electronics are mounted on a wooden stand to keep everything distanced from the conductive surfaces. The setup was also fixed in place so that the residual influences of the background effects could be subtracted from the measurement. The plastic container has dimensions of 58.3cm x 37.2cm x 28.3 cm, filled with up to 61 liters of the medium, emulating soil properties. It is possible to move the container away from the sensor to obtain measurements for the response in the air and then position it below the sensor to obtain measurements of the medium. The container was positioned in the same spot each time to obtain repeatable measurements, and this was done by using markers on the table and the container.
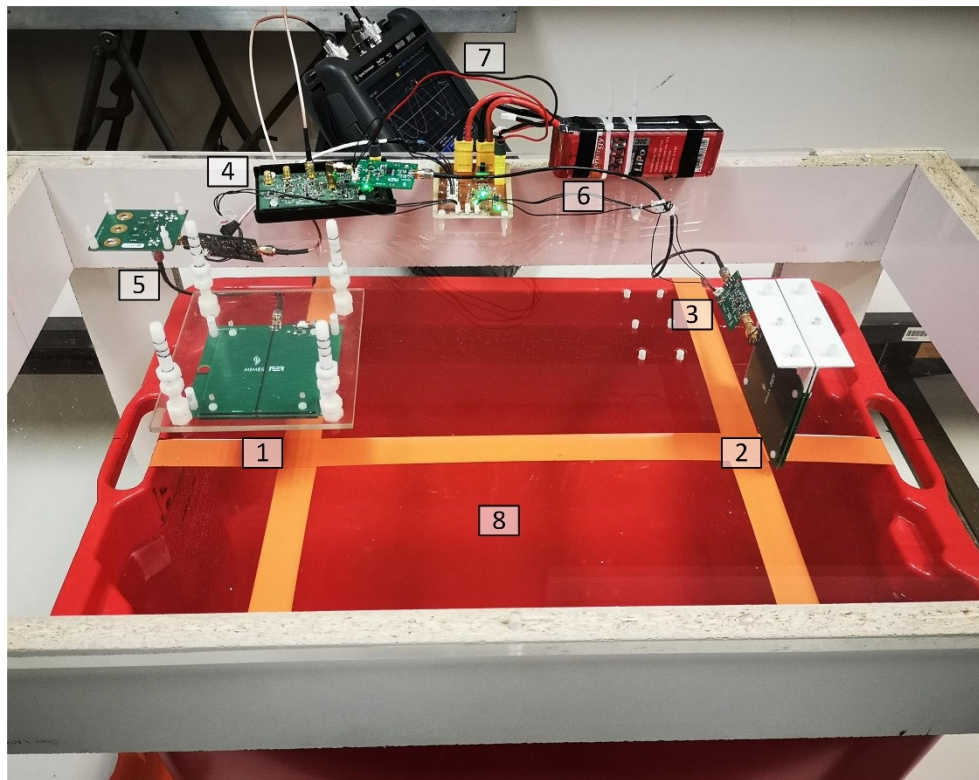
**Figure 17**. Experimental setup: (1) Shielded transmitter coil, (2) Shielded receiver coil, (3) Receiver buffer, (4) Receiver amplifier, (5) Transmitter amplifier, (6) Battery power supply, (7) Keysight Fieldfox N9913A VNA, (8) Container.

The photograph of the sensor is shown in **Figure 18**. The transmitter and receiver are fixed on a rigid plexiglass board. The transmitter is oriented horizontally, with the magnetic moment pointing upwards, and it is fixed in place for all measurements. The transmitter is oriented vertically to the measured medium, with the magnetic moment pointing towards the transmitter. The coils are mutually perpendicular, with the transmitter coil positioned horizontally and the receiver coil vertically with respect to the measured medium. The intercoil separation can be set to 37 cm or 27 cm by moving the receiver coil to pre-drilled spots, measured from the centers of both coils. A mutually perpendicular configuration was chosen to reduce the direct inductive coupling between the coils. The transmitter was offset by 2.08 cm relative to the center of the receiver to obtain a small direct inductive coupling, which gives stable phase lag when measuring sensor response in the air. When the centers of both coils are perfectly aligned, the primary inductive coupling is minimal, and the wrapping of the phase angle complicates the interpretation of measurements. On the other hand, if the primary inductive coupling is too big, the receiver goes to saturation.
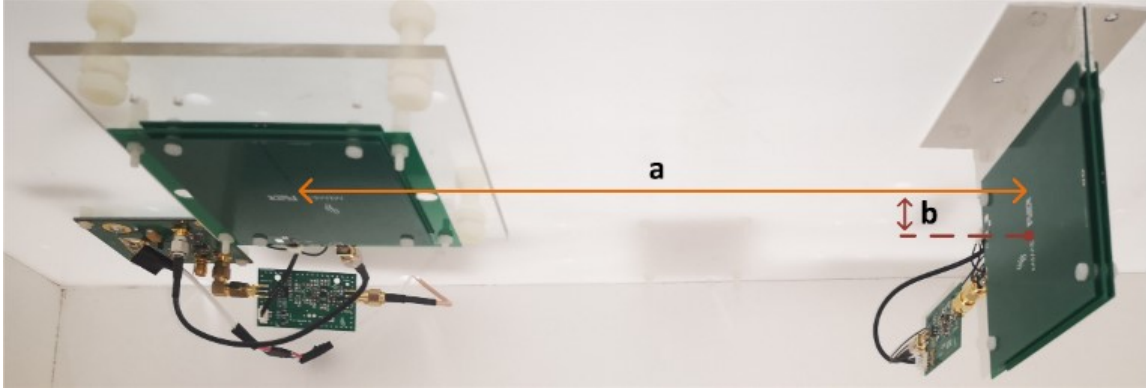
**Figure 18.** Shielded transmitter (TX) and receiver (RX) coils. Intercoil separation $a$ is 37 cm measured from the center of the TX coil to the center of the RX coil. The center of the RX coil is offset for b = 2.08 cm below the center of the TX coil.

## 3.4 Measurement procedure

The sensor response to the medium is represented as the complex ratio of the secondary voltage $U_S$ and the primary induced voltage $U_P$, a standard way of interpreting data from LFEMI soil sensors [53]. The sensor transfer function for the response in the air without the presence of the medium is $H_{air}$, defined as the ratio of the primary coupling $U_P$ and transmitter voltage $U_{TX}$ is measured at the output of the front-end circuitry, which has the transfer function $H_{AFE}$:

$$H_{air} = \frac{H_{AFE} \cdot U_P}{U_{TX}} \ . \tag{111}$$

The transfer function measured with the sensor above the medium is $H_{medium}$, and the receiver voltage is the sum of the primary voltage $U_P$ and the secondary induced voltage due to the coupling through the medium $U_S$:

$$H_{medium} = \frac{H_{AFE} \cdot (U_P + U_S)}{U_{TX}} \tag{112}$$

By subtracting the sensor response in the air from the sensor response above the medium, we obtain the ratio of $U_S/U_P$ and eliminate the effects of the electronics transfer function:

$$\frac{U_S}{U_P} = \frac{H_{medium} - H_{air}}{H_{air}} \ . \tag{113}$$

With this representation, the instrumentation and excitation terms are eliminated, and the measured sensor response can be directly compared to the results of the FEM analysis and other numerical models [91].

## 3.5 FEM model

The FEM analysis of the HFEMI soil sensors was done in CST studio suite 2022 (Dassault Systèmes Simulia) [92]. The FEM model was designed to be equivalent to the measurement setup. The sensor geometry has dimensions similar to the experimental setup used for laboratory measurements. The transmitter coil was modeled with 3 separate loops, the receiver coil had 4 loops, and the total voltage was the superposition of all the transmitter and receiver loops, respectively, except that the shielding was omitted as the parasitic capacitances were not included in the FEM, **Figure 19**.
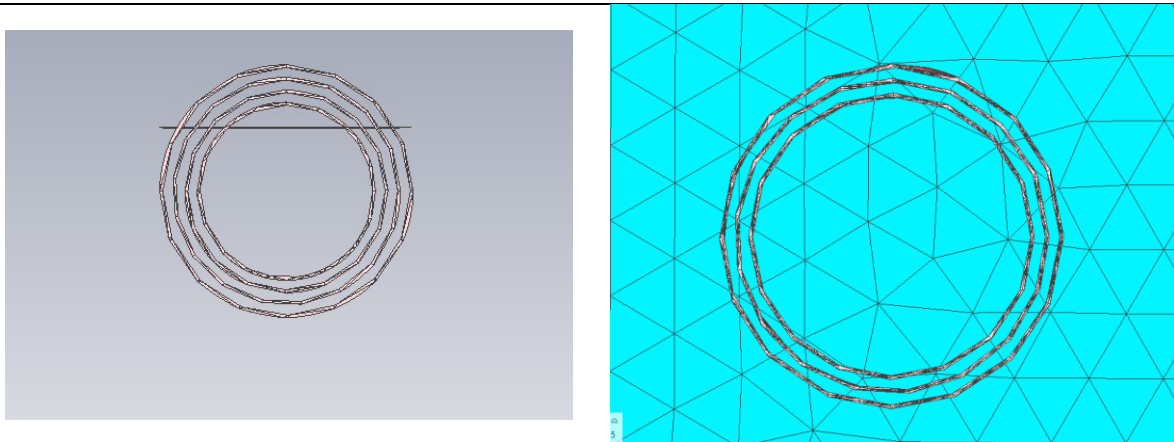


**Figure 19**. FEM model of transmitter coil (left) and receiver coil (right).

The container was modeled as a block structure with dimensions of 59 cm x 37.2 cm x 28.5 cm, the container dimensions used in the laboratory experiments. The domain boundaries were placed 100 cm from the container on each side, with the mesh having 171,068 tetrahedrons and remaining the same throughout all simulations. The homogenous medium was modeled by changing the electromagnetic parameters of the block structure in a range from 0 mS/m to 1 S/m for electrical conductivity and from 1 to 78 for relative permittivity, **Figure 20**(a). The block structure was divided into 17 horizontal sections for the double-layer medium case, **Figure 20**(b). The sections were grouped into two layers: the upper layer was air (light blue) with the height $h_{air}$, and the lower layer was water (dark blue) with the height $h_w$. With this setup, it was possible to vary the height of each layer in discrete steps while the total volume was kept constant. In all measurements, the sensor response in the air was modeled with the medium of zero conductivity and relative permittivity of 1.

(a)                                    (b)
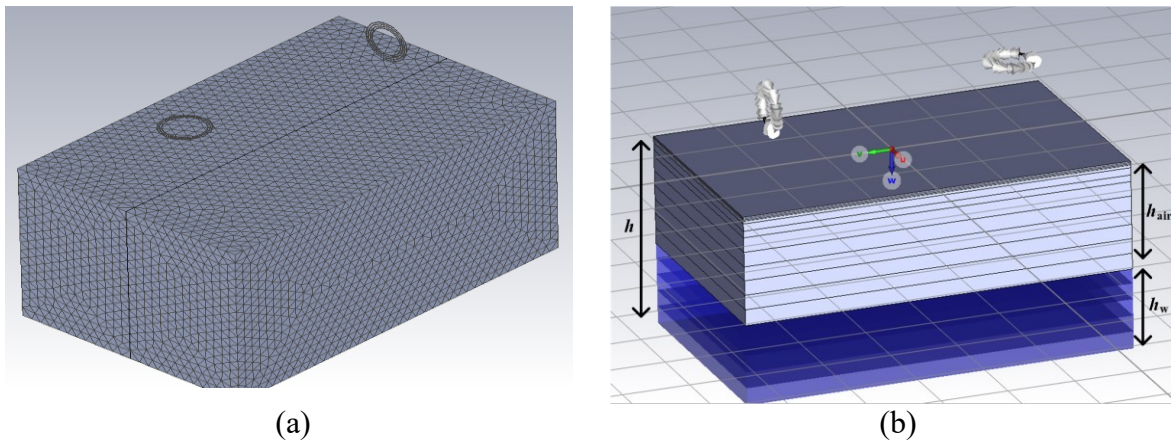
**Figure 20**. FEM model of the container: (a) homogeneous medium, (b) double-layer medium.

The FEM model was used to validate the sensor response to electrical conductivity and dielectric permittivity in the homogeneous case and to evaluate the response to dielectric permittivity in the double-layer case, discussed in Chapter 5. Also, the effects of mechanical misalignment were evaluated by FEM in Chapter 4.3, and FEM was used for comparison of the sensor response in the evaluation of shielding effectiveness in Chapter 4.4.6.

# Chapter 4

# Analysis of unwanted electromagnetic coupling and interference rejection techniques

Analyzing the influences on the sensor response is important to determine the main sources of errors and implement techniques for their mitigation. Rejection of unwanted effects is needed to make the sensor response predominantly dependent on the electromagnetic properties of the soil. The influences on sensor response can be due to the electromagnetic coupling, temperature, and mechanical effects. The sources of errors, calibration methods, and best practices in data acquisition of conventional EMI soil sensors are well documented in the literature [93]–[98].

## 4.1 Liftoff analysis

In conventional soil mapping applications using commercially available EMI devices, the sensors are usually mounted on a vehicle, towed behind, or used as handheld devices. When mounted on a vehicle, the sensor is typically positioned a few tens of centimeters from the ground. In the towed case, the sensor is put on a sled or inside an enclosure, so the distance from the ground is usually a few centimeters [99], and it is not easy to obtain constant liftoff through the measurements. Information about the liftoff is important because the output of the commercial instruments, such as Geonics EM-38, is calibrated with the analytical model of the

half-layer with the height of the sensor on the surface [53]. The measured apparent electrical conductivity is the weighted average of conductivities across the depth [53], [100], and the sensitivity curve is a function of the sensor geometry and coil orientations. In the case of both coils oriented vertically, the sensor response is largest directly above the ground, while for the horizontally oriented coils, the sensor response is largest when lifted above the ground [99], [101], [102]. This means the sensor output and measured electrical conductivity change when liftoff above the ground increases or decreases. The effects of liftoff on the proposed HFEMI soil sensor were evaluated experimentally and using an analytical model.

## 4.1.1 Analytical model verification

The liftoff effects were evaluated using the analytical model described in Chapter 2 by varying the height of both transmitter and receiver coils from 6 cm to 28 cm, measured from the center of the transmitter coil and the surface of the medium at height $z$=0. The results were calculated for the sensor above the infinite half-layer and shown as the ratio of $U_S/U_P$ in the complex plane for liftoff and electrical conductivity dependence with fixed relative permittivity at 5 MHz and 20 MHz. In **Figure 21**, the relative permittivity was fixed to 1. The sensor response decreases for given electrical conductivity with the increase in liftoff. The red lines show $U_S/U_P$ with constant conductivity and variable liftoff, and the blue lines show variable conductivity with constant liftoff. The relative permittivity was fixed at 20 In **Figure 22**, and the offset in the real part of the $U_S/U_P$ due to the permittivity also decreases with the liftoff.



(a)                                                        (b)
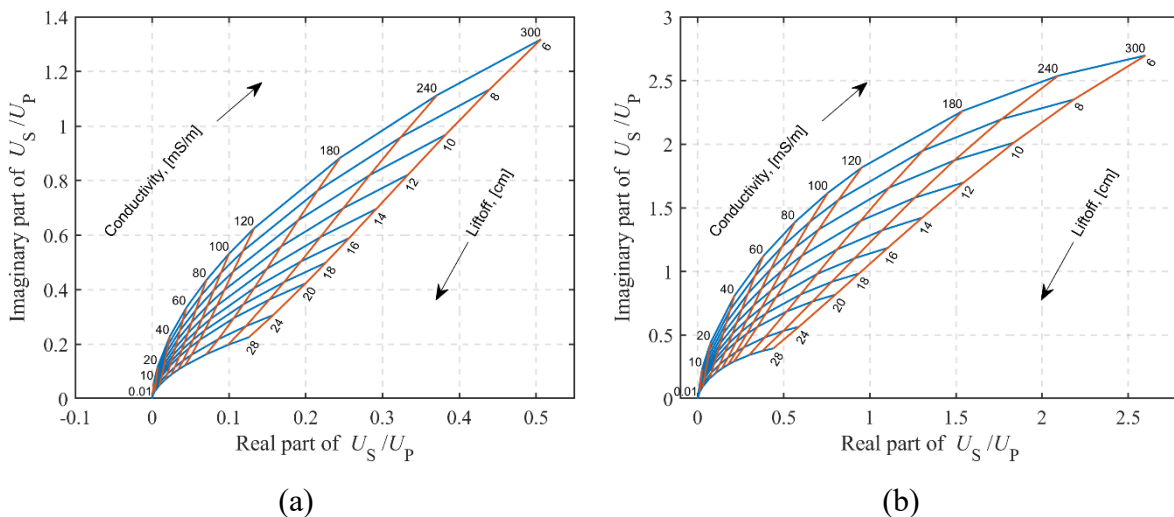
**Figure 21.** Analytical model results for the sensor response $U_S/U_P$ depending on the liftoff and conductivity, with relative permittivity set to 1. The red lines represent constant conductivity, and the blue lines represent constant liftoff: (a) 5 MHz, (b) 20 MHz.

(a)

(b)
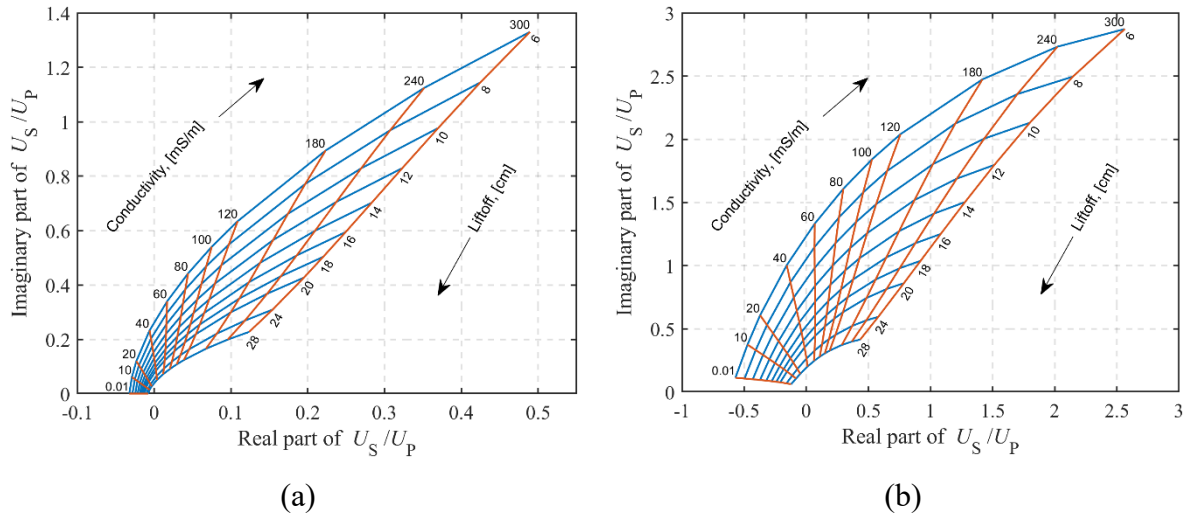
**Figure 22.** Analytical model results for the sensor response $U_S/U_P$ depending on the liftoff and conductivity, with relative permittivity set to 20. The red lines represent constant conductivity, and the blue lines represent constant liftoff: (a) 5 MHz, (b) 20 MHz.

The effects of liftoff on measured permittivity are shown in **Figure 23** for 5 MHz and 20 MHz with electrical conductivity fixed at 0.01 mS/m. Red lines represent constant permittivity with variable liftoff, and red lines are constant liftoff with variable permittivity. A 3D graph of the complex plane at 5 MHz for each pair of electrical conductivity and dielectric permittivity is shown in **Figure 24** for each liftoff.



(a)

(b)
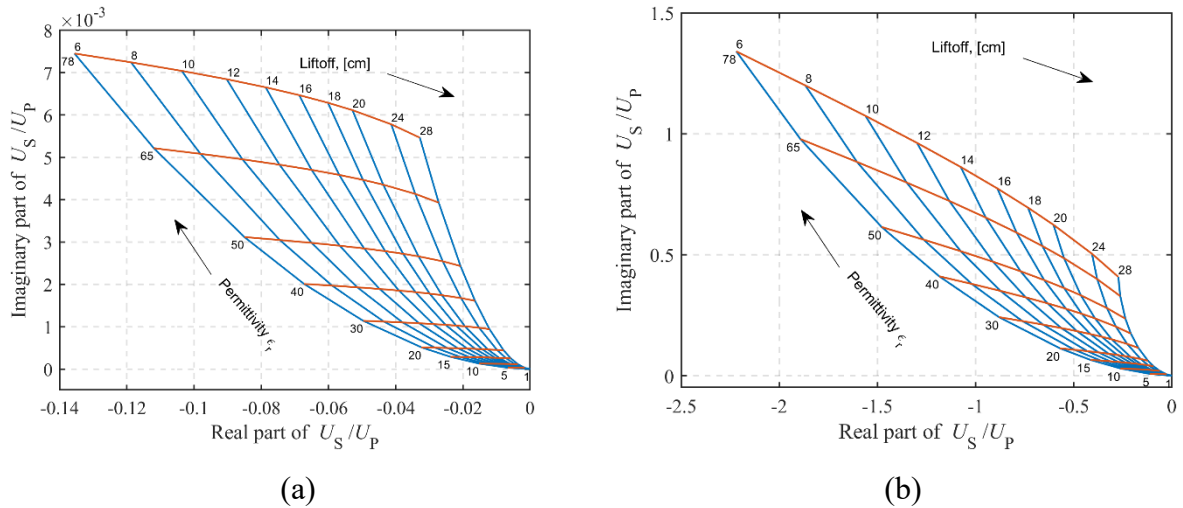
**Figure 23.** Analytical model results for the sensor response $U_S/U_P$ depending on the liftoff and permittivity, with electrical conductivity set to 0.01 mS/m. The red lines represent constant permittivity, and the blue lines represent constant liftoff: (a) 5 MHz, (b) 20 MHz.
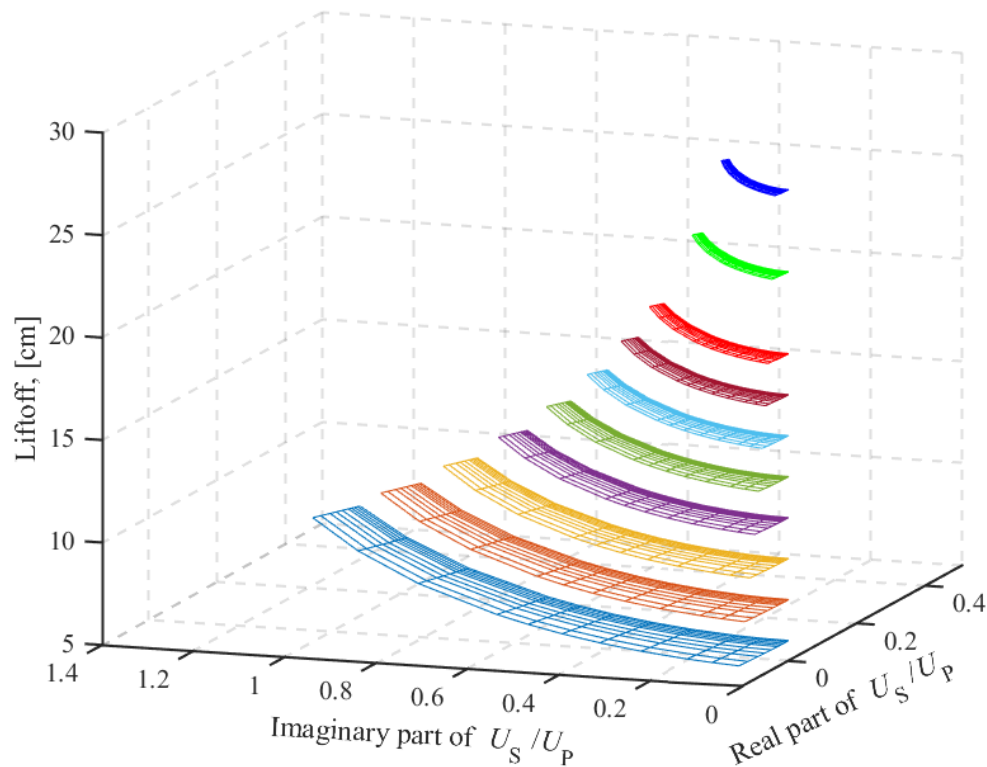
**Figure 24.** Analytical model results for the sensor response $U_S/U_P$ at 5 MHz, depending on the electrical conductivity, relative permittivity, and liftoff.

## 4.1.2 Experimental verification

The sensor response to changes in liftoff was measured for the proposed sensor geometry with the perpendicular coils. The sensor was mounted on a stand above the container filled with water. The experimental runs were done for four different conductivity levels: 60, 118, 180, and 236 mS/m. The liftoff was increased from 9.8 cm to 23.7 cm in 10 points by increasing the height of the stand while keeping the container fixed. The distance was measured from the center of the transmitter coil to the water surface. The liftoff of 9.8 cm was the default distance of the measurement setup. The sensor response in the air was measured for each point of liftoff to mitigate the effects of any changes due to the coupling with the environment.

The effect of the liftoff is depicted in **Figure 25**, with the lines of constant conductivity (blue) and constant liftoff (red) shown in the complex plane measured at 5, 10, 15, 20, 25, and 27 MHz. An increase in the liftoff reduces the sensitivity to conductivity towards zero, making the perpendicular coil configuration similar to the vertical-oriented coil configuration, as discussed in [95]. For higher-frequency ranges, e.g., above 10 MHz, the results imply that it is possible to measure electrical conductivity and the sensor lif-toff simultaneously using one frequency, provided that the dielectric permittivity is known or constant. This could be important in towed sensing applications where it is hard to keep fixed liftoff.
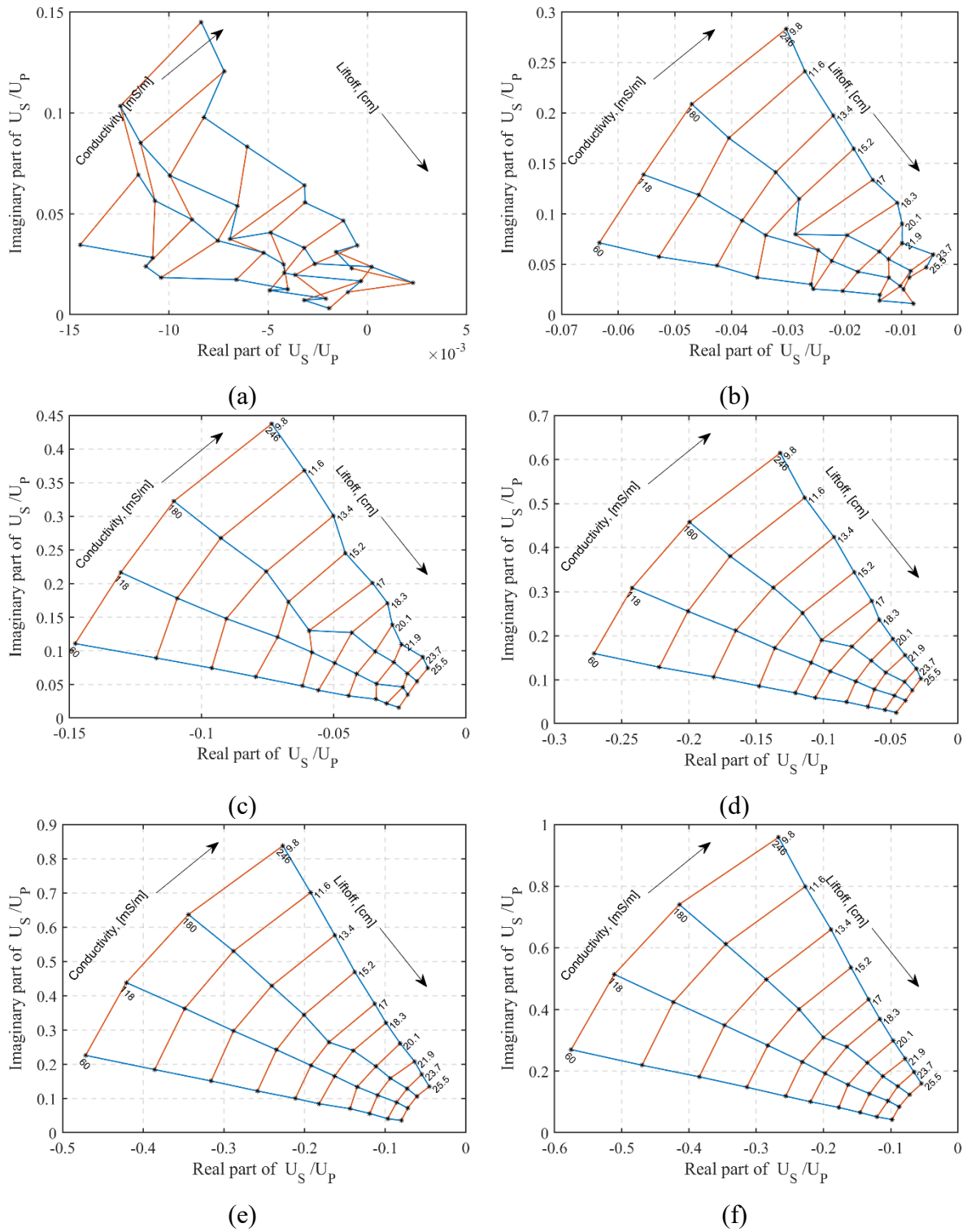
**Figure 25.** The ratio $U_S/U_P$ dependent on the liftoff and conductivity. The blue lines represent constant conductivity, and the red lines represent constant liftoff. Linear interpolation is used between data points: (a) 5 MHz, (b) 10 MHz, (c) 15 MHz, (d) 20 MHz, (e) 25 MHz, (f) 27 MHz.

Real and imaginary parts of the sensor response signal, dependent on the liftoff, for frequencies from 5 MHz to 27 MHz, are shown in **Figure 26** and **Figure 27**. The measurements above the medium with a low conductivity of 60 mS/m are shown in **Figure 26,** and the measurements above the medium with a high electrical conductivity of 236 mS/m are shown in **Figure 27**. The change in liftoff influences both real and imaginary signal components for low and high conductivity.



(a)                                                    (b)
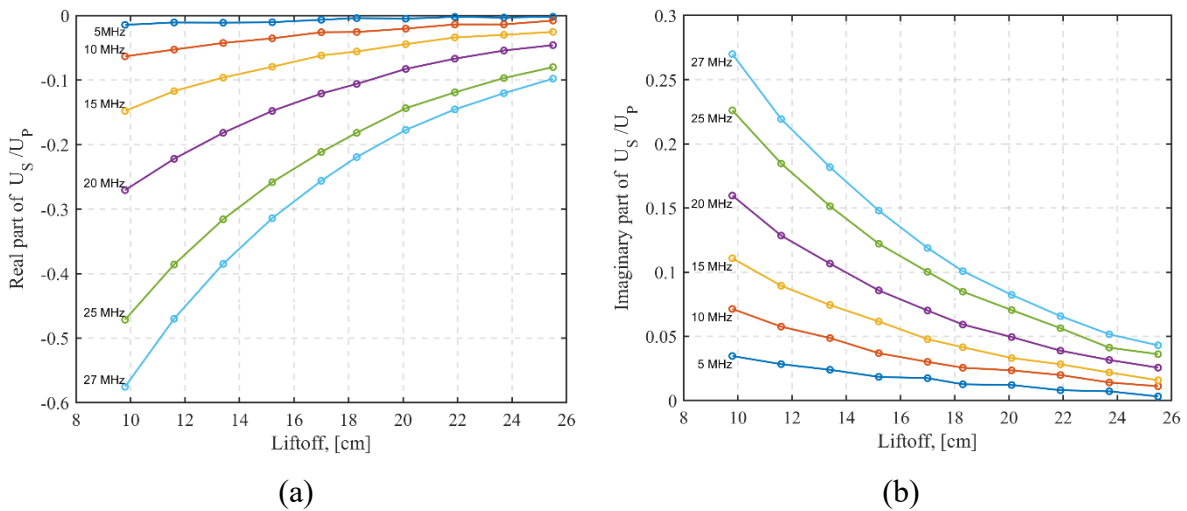
**Figure 26.** Sensor response above the medium with electrical conductivity 60 mS/m depending on the lift-off for 5, 10, 15, 20, 25, and 27 MHz: (a) Real part of ratio Us/Up, (b) Imaginary part of ratio $U_S/U_P$.



(a)                                                    (b)
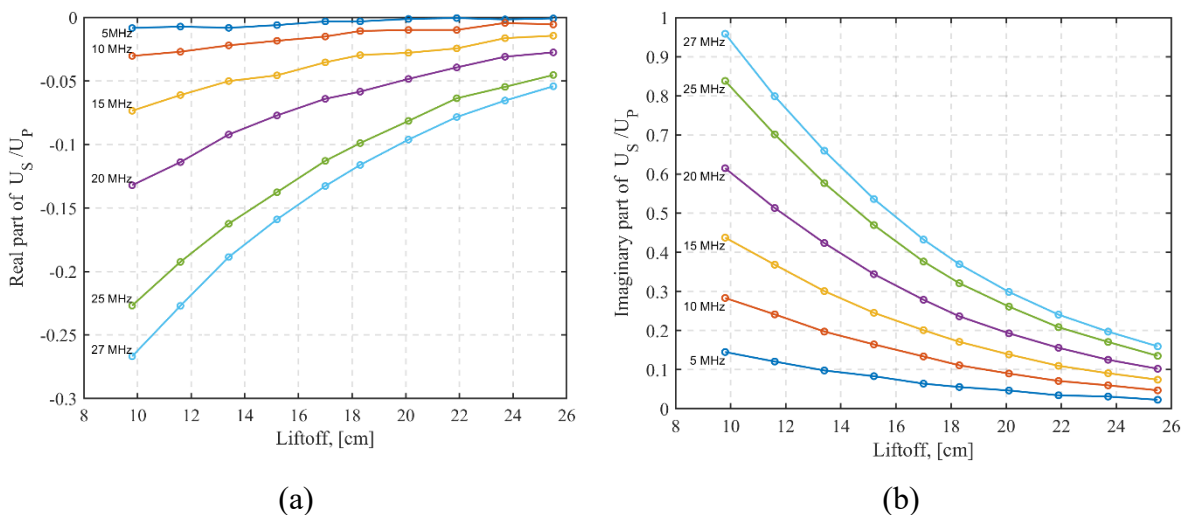
**Figure 27.** Sensor response above the medium with electrical conductivity 246 mS/m depending on the lift-off for 5, 10, 15, 20, 25 and 27 MHz: (a) Real part of ratio Us/Up, (b) Imaginary part of ratio $U_S/U_P$.

The absolute value of the sensor response depending on the liftoff is shown in **Figure 28** for the lower conductivity medium (60 mS/m) and higher conductivity medium (236 mS/m). The magnitude of the signal is higher for the high-conductivity medium, as expected. In both cases, the magnitude of the signal decay with the increase of liftoff is non-linear.
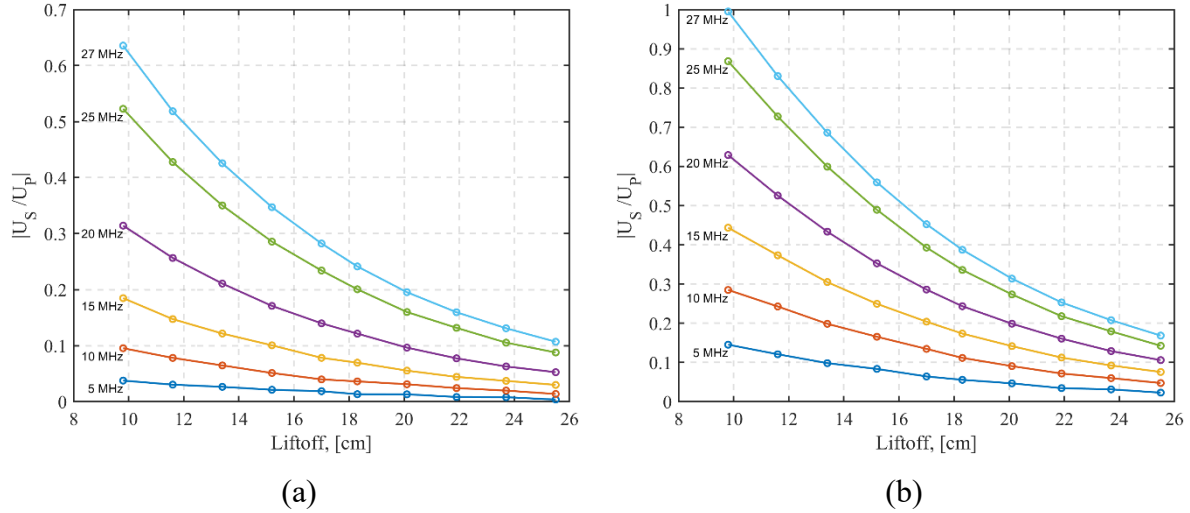


**Figure 28.** Absolute values of ratio $U_S/U_P$ depending on the liftoff for 5, 10, 15, 20, 25 and 27 MHz above the medium with electrical conductivity: (a) 60 mS/m, (b) 246 mS/m.

The signal decay was analyzed by dividing the absolute value sensor response at a certain liftoff by the sensor response at the minimal liftoff when the signal is maximal (114):

$$S.C. = \frac{\left|\dfrac{U_S}{U_P}\right|_{liftoff\,(i)}}{\left|\dfrac{U_S}{U_P}\right|_{liftoff\,(min)}} \cdot 100\% \quad . \tag{114}$$

The ratio of measured signal magnitudes of increased liftoff and minimal liftoff is shown in **Figure 29**. Blue lines show signal change above the medium with a conductivity of 60 mS/m, and the red line shows the medium with a conductivity of 236 mS/m. Results marked with x show a change when the excitation frequency is 5 MHz, and those marked with "o" show a change for the excitation frequency of 27 MHz. It is noticeable that the signal change is similar for the lowest and highest frequencies, suggesting that the change due to the liftoff is frequency-independent in the measured frequency range. The same conclusion can be drawn from the expression (110), showing that the geometry influences are independent of the electromagnetic parameters of the medium. This fact can be useful for the future development of liftoff compensation.
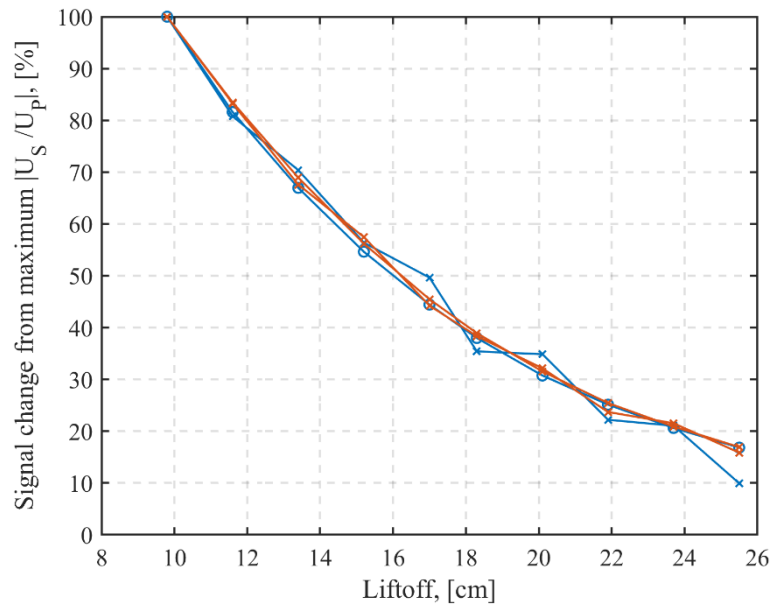
**Figure 29.** Signal change shown as the ratio of different liftoffs and minimal liftoff response.

## 4.2 Temperature influence

A significant challenge in the EMI measurements is the influence of the temperature on the sensor response. Temperature effects are researched in the context of commercially available EMI devices such as Geonics and Dualem. It is noteworthy to discuss and analyze these effects as it can be expected that they are also present in HFEMI soil sensor applications. Temperature drift represents variations in the sensor measurements caused by ambient, device, and soil temperature changes [96], [103]. Temperature drift can manifest as a slow change during the day or a fast change due to environmental conditions, such as exposure to direct sunlight. The main research tracks concerning temperature effects are electronic instrumentation for drift compensation and sensor improvements [94], [104], modeling of temperature effects [105]–[108], sensor evaluation in laboratory and field conditions [93], [109]–[111] and calibration techniques [95], [112], [113].

The influence of ambient temperature on drift in commercially available instrument EM-38 by Geonics is discussed in [94]. The authors found that the high ambient temperature can significantly influence the sensor readings, especially above 40°C, which was the limit for the temperature compensation circuitry. Generally, the electronic components also have temperature dependence, which affects the sensor response. Another issue is the positioning of the compensation circuitry, which was implemented on the control board far from the coils. Due to the distance between the transmitter and receiver coils, it is possible that the heating of the coils is uneven. The suggestion is to put the instrument inside the enclosure, preferably

made out of wood, to keep the heating of the instrument uniform. The approach using multiple temperature sensors near each coil and electronics is proposed in [103] so that the temperature of the coil can be used in the correction model. Field tests described in [93], [94] suggest that the EMI sensor drifts over a typical survey duration, i.e., 8 hours per day, which can be significant, especially over low-conductivity soil. It is necessary to calibrate the instrument multiple times per day during the survey, and it is suggested to avoid measurements during hot and sunny days [114] or to shade the instrument properly [111]. Another common practice in field surveys is to run a drift row, which means measuring along the dedicated row in the field [94], then returning to the same row later in the day and repeating the measurements [93].

The change in soil temperature during the survey affects measured electrical conductivity. Typically, the sensor response is affected by the changes in temperature of the first 10 cm of soil during the single-day surveys. This upper layer can have considerable changes in the temperature, but it decreases rapidly with the depth [110]. When the soil conductivity is represented as the apparent electrical conductivity $EC_a$ used in the conventional EMI soil sensing using commercial devices such as Geonics EM-38, various empirical relationships were determined to recalculate the $EC_a$ into the $EC_{25}$, which is the conductivity at 25°C to enable the comparison of data from different measurement runs. The exponential relation in [93] where the $T_{\text{soil}}$ is the temperature of the soil in °C in the range from 3°C to 50°C is given as:

$$EC_{25} = EC_a \cdot \left( 0.447 + 1.4034 \cdot e^{\left( -\frac{T_{soil}}{26.815} \right)} \right). \tag{115}$$

The ratio model useful in the temperature range from 3°C to 47 C is given in [115] with the $v$ as the temperature slope constant:

$$EC_{25} = \frac{EC_a}{1 + \vartheta(T - 25)}. \tag{116}$$

The cubic relation connecting $EC_{25}$ and $EC_a$ is given in [116] as:

$$EC_{25} = EC_a \cdot \left( 1 - 0.20346 \cdot T + 0.03822 \cdot T^2 - 0.00555 \cdot T^3 \right), \tag{117}$$

with the T defined in °C as

$$T = \frac{T_{soil} - 25}{10}. \tag{118}$$

These analyses and empirical relationships of temperature influence on conventional commercially available low-frequency EMI sensors provide an insight into these effects in the HFEMI sensors for similar use cases and geometries.

## 4.2.1 Temperature drift of the HFEMI sensor system

Temperature can significantly influence the sensor response, especially in field conditions with frequent temperature fluctuations and under direct sunlight. A qualitative analysis of the temperature drift of the proposed HFEMI sensor was conducted in both laboratory and field settings. The drift was analyzed for the primary magnetic field coupling $H_p$, assuming that both transmitter and receiver circuitry heat evenly. The drift in primary coupling affects the data interpretation as the results are usually shown as the secondary to primary magnetic field ratio. Observing the temperature effect on the secondary magnetic field $H$s is difficult due to the interaction with other medium physical properties influencing the sensor response to the electromagnetic soil parameters.

The absolute value of the primary magnetic field coupling Hp measured in the laboratory is shown in **Figure 30** for (a) 5 MHz, (b) 10 MHz, (c) 20 MHz, and (d) 27 MHz. The measurements were taken at 75 points during the experimental run over 13 h. The laboratory temperature was fairly stable, around 24°C throughout the measurements.
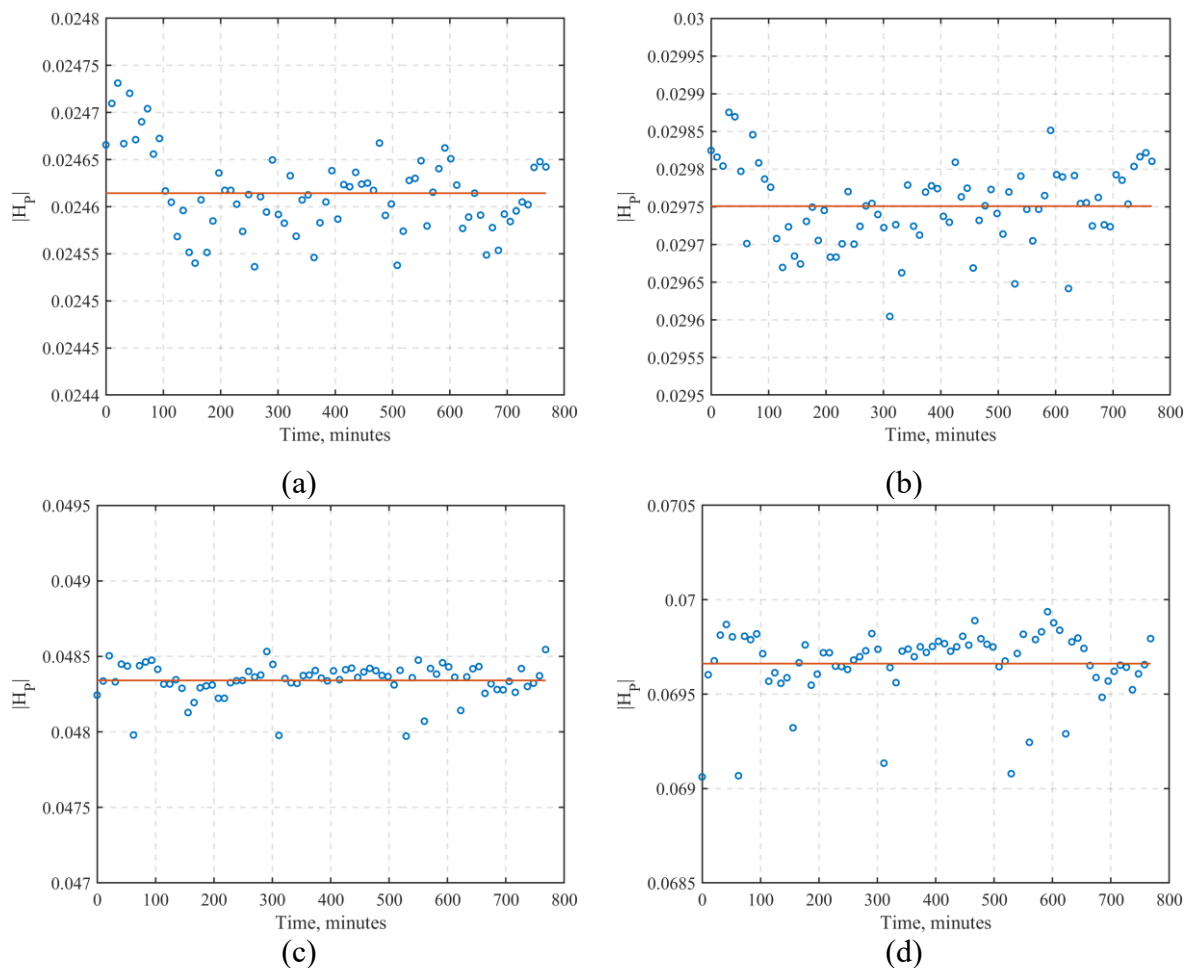


**Figure 30.** Sensor response in the air $|H_p|$ during the laboratory measurement: (a) 5 MHz, (b) 10 MHz, (c) 20 MHz, (d) 27 MHz.

The change in the signal was calculated as

$$\Delta H_P = \frac{\max(H_P) - \min(H_P)}{\max(H_P)} \cdot 100\%.$$

(119)

The measurement of the primary field is stable for all observed frequencies throughout the experiment. The percentage of signal change from maximum to minimum values is 0.8% at 5 MHz, 0.9% at 10 MHz, 1.2% at 20 MHz, and 1.3% at 27 MHz.

The field measurements were done on two sites over multiple days with different weather conditions. Measurements shown in Figure 31 were made on the 14th and 18th of October, 2022, on site 1 in Ludbreg, Croatia. Both figures show measurements for (a) 5 MHz, (b) 10 MHz, (c) 20 MHz, and (d) 27 MHz. Primary magnetic coupling $H$p was measured when the sensor was positioned 1 m above the ground. Two measurement runs at different times are shown in Figure 31.

The first measurement run of 24 points (blue line) started around 13h, and the second run of 22 points (red line) around 16h. Both runs lasted approximately 2 hours. The drift in the signal is noticeably larger for the first experimental run across all frequencies, as the measurement was done when the insolation was higher, and there was a more significant temperature gradient. The measurement setup was shaded from the sun in the second experimental run. The percentage of change in $H_p$ was calculated as the ratio of the difference between the first and the last measurement, divided by the first measurement, **Table 2**. The change from the first to the last measurement also increases with the increase of the excitation frequency. Measured primary coupling in the laboratory conditions is stable, and the fluctuations are not due to the temperature effects. On the other hand, in field conditions, there is an obvious change in the measured primary coupling due to the temperature influence on the electronics and coils, especially when directly under sunlight.

**Table 2**. The percentage of the primary field changes from the first to the last measurement.

| Frequency [MHz] | $|H_p|$ change [%] | |
| :---: | :---: | :---: |
| | First measurement run (blue line) | Second measurement run (red line) |
| 5 | 1.72 | 0.59 |
| 10 | 2.6 | 0.72 |
| 20 | 2.94 | 1.33 |
| 27 | 3.72 | 1.93 |
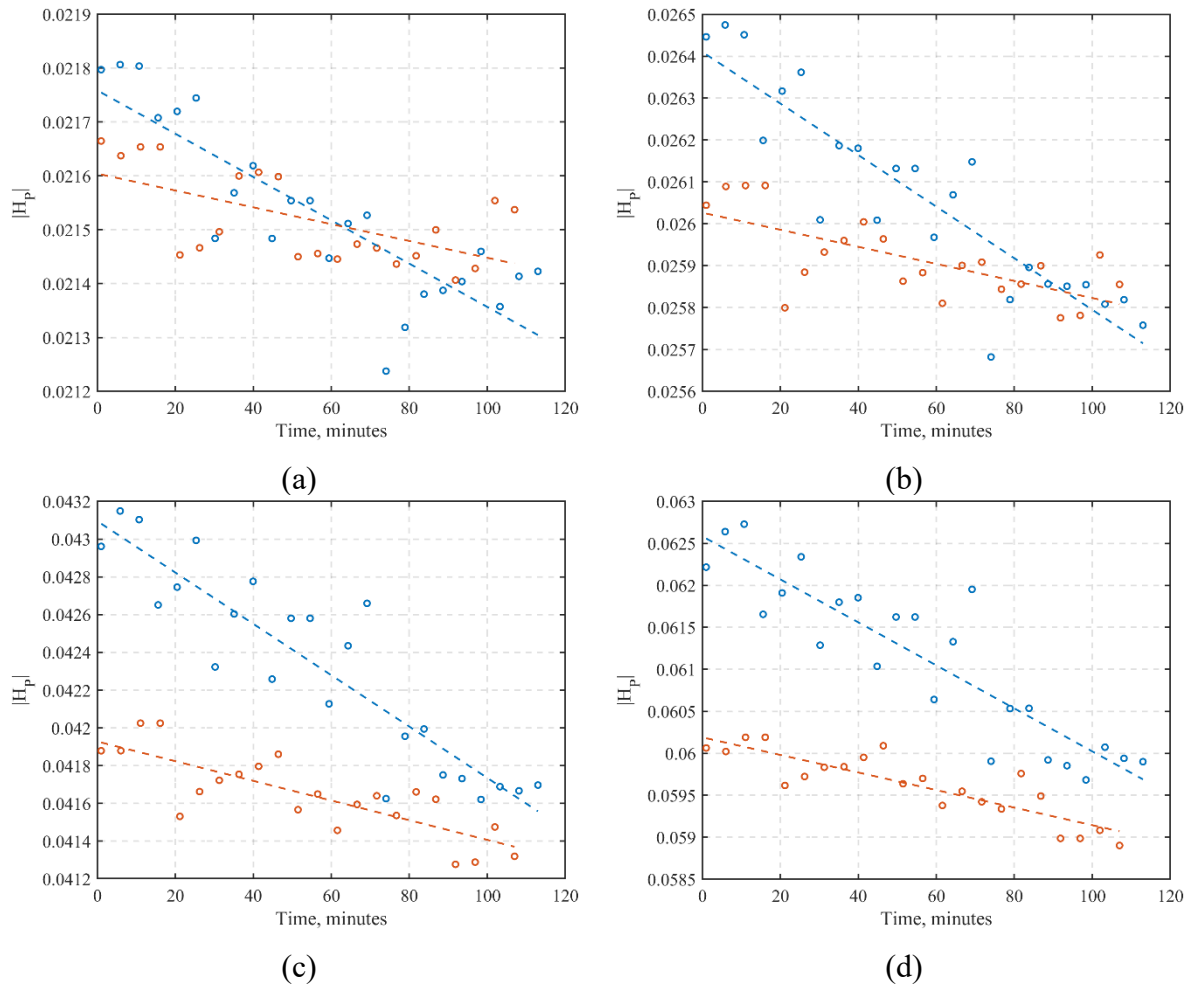
**Figure 31**. Sensor response in the air $|H_p|$ during the first field test for two experimental runs. The first run was done earlier in the day (blue), and the second run later (red). Circles represent measurements, and dashed lines least squares fit. Results are shown for (a) 5 MHz, (b) 10 MHz, (c) 20 MHz, (d) 27 MHz.

The sensor response in the air and the ambient temperature were measured in the experimental run that lasted for 2 hours. The HFEMI sensor and temperature sensor were under direct sunlight from 12h noon to 14h. The ambient temperature was measured with a WTW 340i electrical conductivity probe placed next to the sensor. The results are shown in **Figure 32** for (a) 5 MHz, (b) 10 MHz, (c) 20 MHz, and (d) 27 MHz. The measured sensor response $H_p$ is shown with blue circle marks, and the measured temperature is shown with red x marks. The least squares linear fit was done for both measurements, shown as a blue dashed line for sensor response and a red dashed line for measured temperature. The trend on all frequencies shows that the measured sensor response decreases with the increase in ambient temperature.

(a)

(b)

(c)

(d)
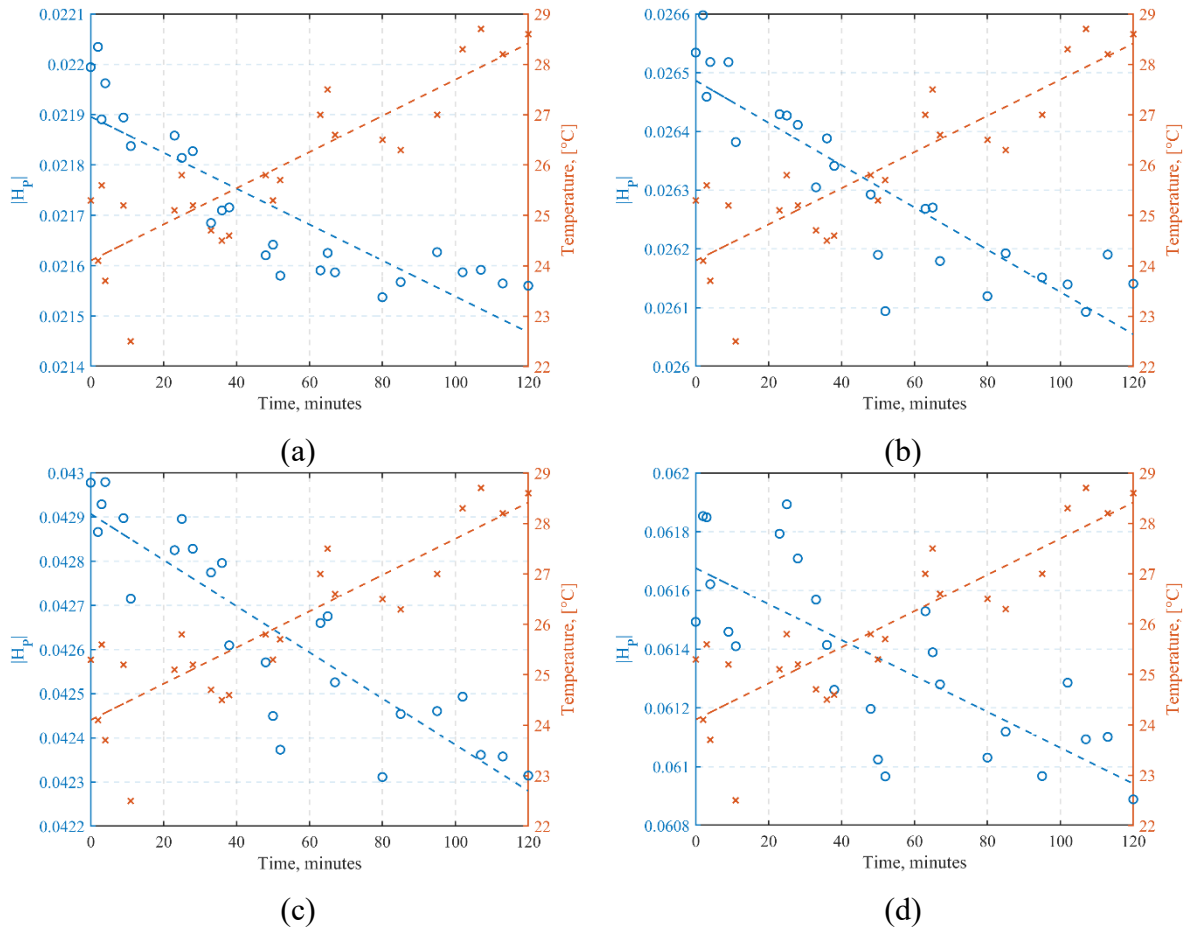
**Figure 32**. Sensor response in the air $|H_p|$ (blue circles) and measured air temperature (red x) during the first field test. Dashed lines are the least square fit. Results are shown for (a) 5 MHz, (b) 10 MHz, (c) 20 MHz, (d) 27 MHz.

The measurements in **Figure 32** are also shown in **Figure 33** as the sensor response in dependence on the air temperature. Blue crosses represent the measurements, and the dashed red lines are the least square fit of the temperature dependence. Temperature coefficients at the shown frequencies for a given temperature range, calculated from the slope of the line obtained by the least square fitting, are $-6.75 \times 10^{-6}$ [°C$^{-1}$] for 5 MHz, $-6.79 \times 10^{-6}$ [°C$^{-1}$] for 10 MHz, $-9.23 \times 10^{-6}$ [°C$^{-1}$] for 20 MHz, and $-9.79 \times 10^{-6}$ [°C$^{-1}$] for 27 MHz.
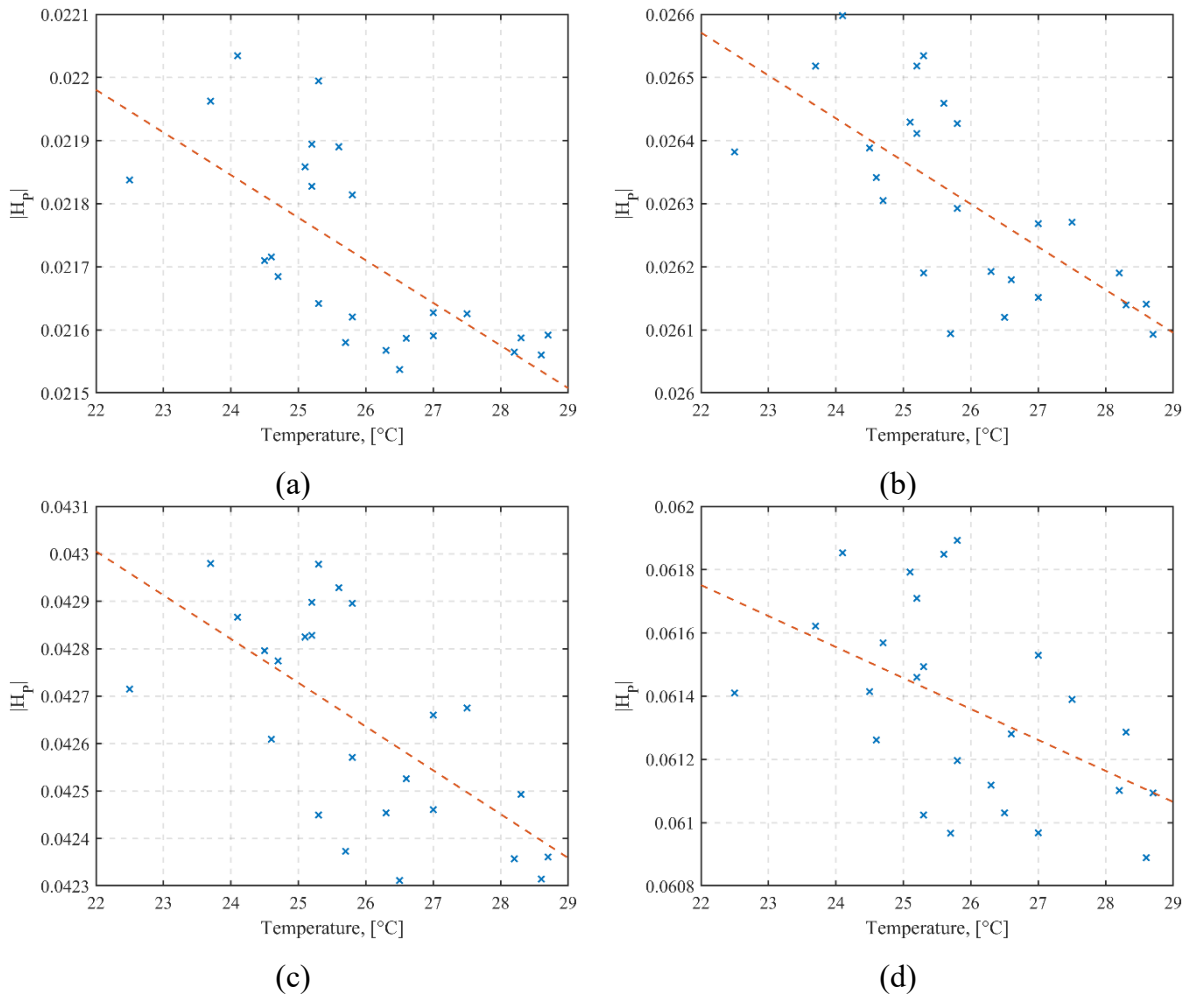
**Figure 33**. Sensor response in the air $|H_\mathrm{p}|$ in regards to measured temperature during 2h experimental run. Blue x marks represent measurements, and the dashed line is the least square fit of data. Results are shown for (a) 5 MHz, (b) 10 MHz, (c) 20 MHz, (d) 27 MHz.

The second field test was done on the 11th and 14th of September, 2023, at test site Jazbina, Croatia. Measurements of $|U_\mathrm{p}|$ done on both days are shown in **Figure 34** for (a) 5 MHz, (b) 10 MHz, (c) 20 MHz, and (d) 27 MHz. On the first day, the experiment was done around noon, the temperature was 27°C, and the sensor was exposed to direct sunlight. Measurements were taken in 2 intervals, 50 minutes apart, and 5 measurements were taken for each interval. On the second day, the temperature was 18°C, and it was a cloudy day. The experiment was done early in the morning, starting from 7 h in 4 intervals 50 minutes apart, and 5 measurements for each interval. Measurements in each interval took 10 minutes. Measurements of the first day are shown with red crosses, and the second-day measurements are with blue circles. On both days, there is a drift in the signal between each interval, and the measurements during the same interval are grouped and stable. The trend indicates that the signal decreases with the

increase in temperature, and it is necessary to calibrate the instrument periodically during the field trials.
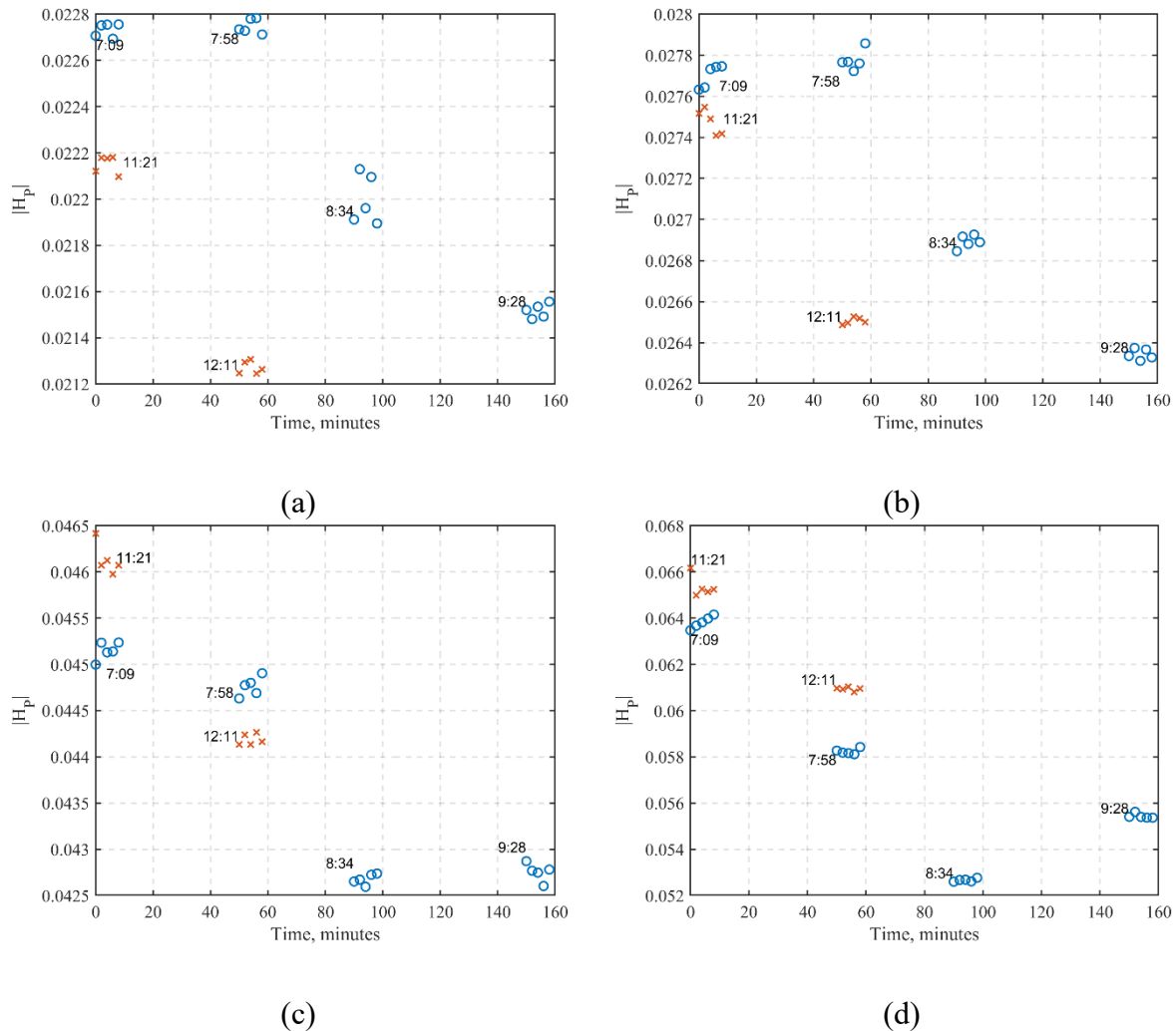


**Figure 34**. Sensor response in the air $|H_p|$. Results are shown for (a) 5 MHz, (b) 10 MHz, (c) 20 MHz, (d) 27 MHz.

## 4.3 Influence of mechanical misalignment

Mechanical influences such as vibrations or bending can impact the sensor output, especially in field conditions where the operator holds the sensor in hand or is mounted on a vehicle. In addition to the discussed liftoff effects, the sensor can also change the angle relative to the ground surface [96], and the mechanical stress within the sensor can alter the precise positions of the coils, changing their relative position.

The mechanical misalignment errors of the proposed HFEMI soil sensor were analyzed by the FEM model. This approach was chosen over the laboratory evaluation in which the sensor is fixed, as small changes in sensor geometry can be precisely set in the FEM setup. The

dimensions of the FEM model were chosen equal to the laboratory setup. The primary coupling $H_P$ was calculated as the sensor response in the air with a medium set to an electrical conductivity of 0 mS/m and a relative permittivity of 1. The secondary coupling $H_S$ was calculated above the medium with an electrical conductivity of 60 mS/m and relative permittivity of 78.

The sensor response was evaluated for the small changes in the transmitter coil height and distance relative to the receiver coil. Also, the changes in the tilt angles were evaluated for both transmitter and receiver coils for sensor response in the air and above the medium. The tilt angles of significance are pitch and roll, as the yaw angle of the coils does not change the position relative to the inspected medium, **Figure 35**. The pitch angle for the transmitter coil varied from -3.75 to 3.75 degrees relative to the medium and reference position, shown in **Figure 35** (a). The variation in roll angle for the transmitter coil was done in both directions from -3.75 to 3.75 degrees, **Figure 35** (b). When the transmitter angles were varied, the receiver coil was fixed in the reference position, and when the receiver coil angles were varied, the transmitter coil was fixed in the reference position.



(a)



(b)
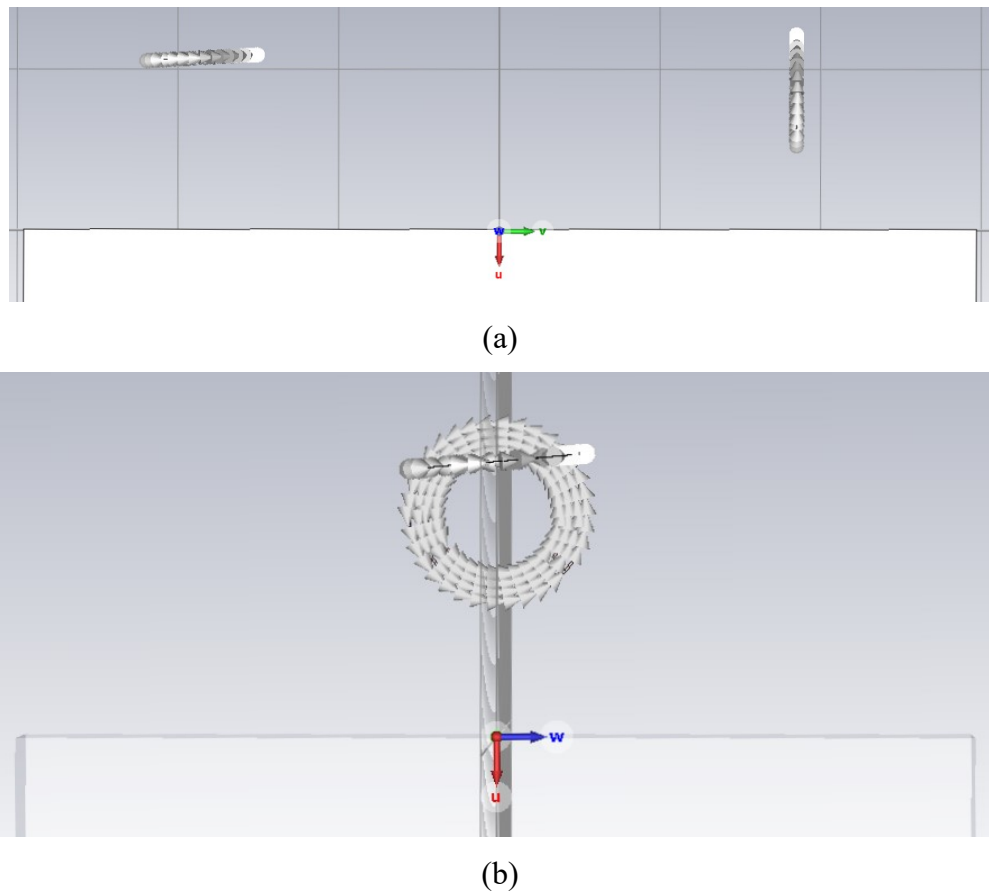
**Figure 35.** Transmitter coil tilt angles in FEM analysis: (a) pitch angle tilt, (b) roll angle tilt.

The reference distance between the centers of the TX and the RX coil is set to 37 cm, and the center of the TX coil is 2.08 cm below the center of the RX coil, which is defined by the dimensions and requirements of the laboratory setup. The horizontal offset from the reference distance between the TX and RX coils was varied from -5 mm (TX coil closest to RX coil) to 5 mm (TX coil moved furthest from RX coil) in 1.25 mm steps. The vertical offset from the reference TX position was varied from -1 mm (TX coil in the highest position) to 1 mm (TX coil in the lowest position) in 0.25 mm increments.

The results at 20 MHz are shown in **Figure 36**(a) for the primary coupling magnitude $|H_P|$ and the secondary coupling magnitude $|H_S|$ in **Figure 36**(b). The reference position is marked with blue "x", sensor response due to the horizontal offset with red circles, and response due to the vertical offset with yellow circles. The change in primary coupling is linear with the change in distance and height, and the geometry is more sensitive to the change in height, **Figure 36**(a). The change in the secondary coupling is almost unchanged for small changes in both distance and height. The different values are due to the numerical errors, as the change in geometry affects the mesh grid of the FEM simulation, **Figure 36**(b). The magnitude $|U_S/U_P|$ at 20 MHz is shown in **Figure 37** for distance and height offset. For all cases, the offset mainly affects the primary coupling and introduces the error when representing the sensor response as the secondary to primary coupling ratio.



(a)                                                                (b)
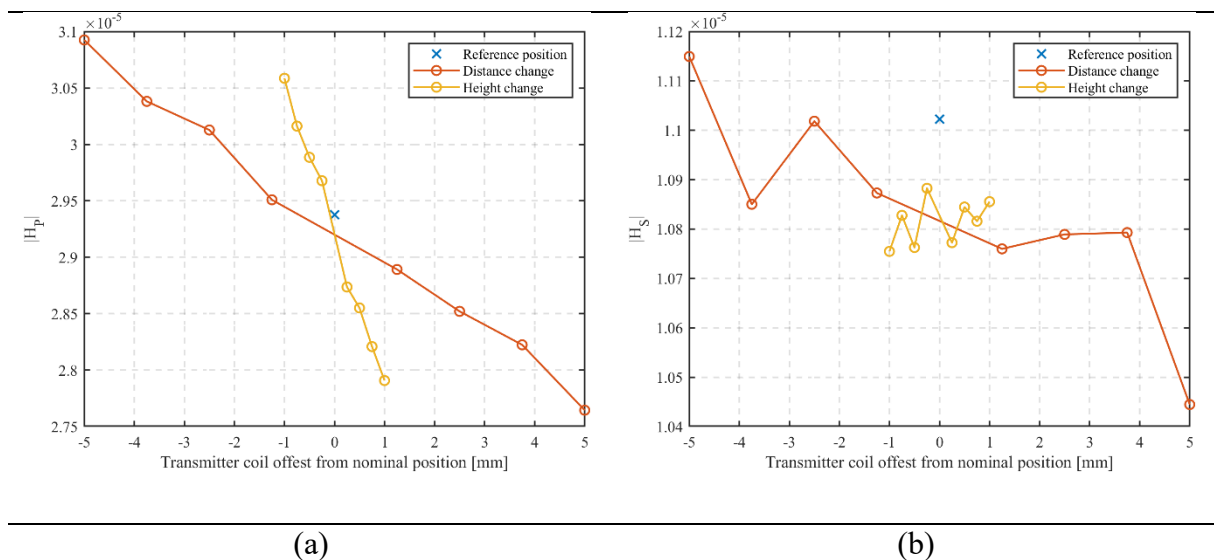
**Figure 36.** (a) FEM analysis of transmitter coil offset from reference position above conductive medium with conductivity 60mS/m and permittivity 78 at 20 MHz for (a) Primary coupling $H_P$ and (b) Secondary coupling $H_S$. Blue x represents the reference position, red lines are horizontal offset, and yellow lines are vertical offset.
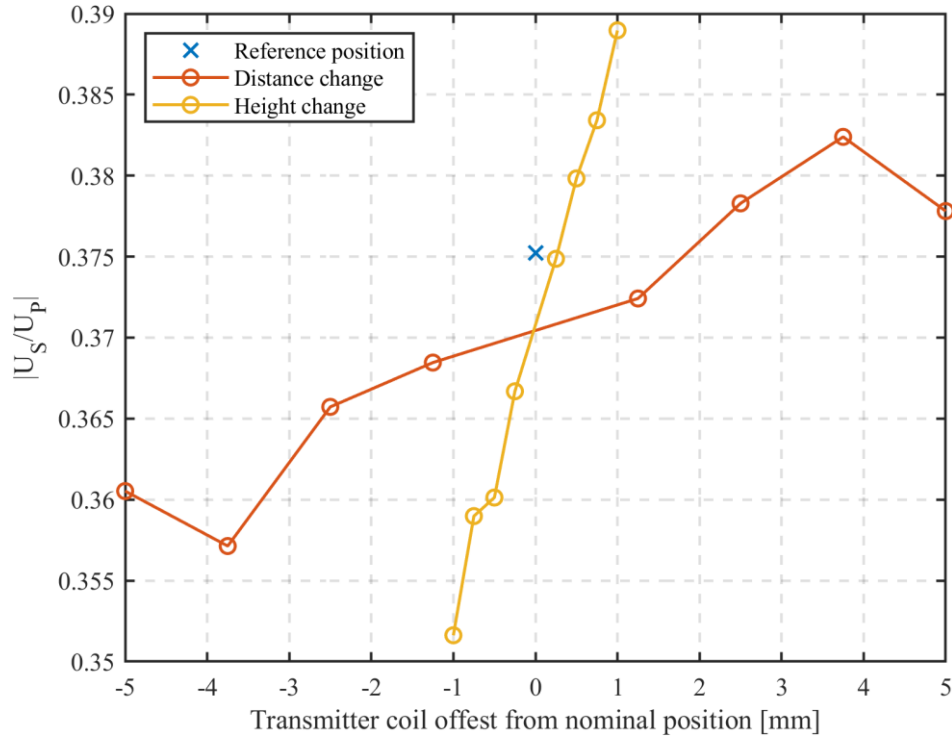
**Figure 37**. FEM analysis of transmitter coil offset from reference position above conductive medium with conductivity 60mS/m and permittivity 78 for the ratio of $U_S/U_P$ for horizontal (red) and vertical offset (yellow) at 20 MHz.

The errors of primary and secondary coupling, relative to the reference position $|H_{REF}|$ are calculated as:

$$ERR = \frac{\left|H_X - H_{X,ref}\right|}{\left|H_{X,ref}\right|} \cdot 100 \left[\%\right] \tag{120}$$

with $H_X$ being either $|H_P|$, $|H_S|$, or $|U_S/U_P|$ at 10 MHz, 20 MHz and 25 MHz, **Table 3**. The change of primary coupling is the same for all frequencies: The change in secondary coupling decreases with the frequency for the same offsets due to the sensitivity to the medium below and changes in the mesh.

**Table 3.** Relative distance and height misalignment errors for primary coupling $H_P$, secondary coupling $H_S$, and ratio $U_S/U_P$ at 10 MHz, 20 MHz, and 25 MHz.

| | Relative distance error [%] | | | Relative height error [%] | | | |
|---|---|---|---|---|---|---|---|
| | TX offset [mm] | Hp | Hs | Hs/Hp | TX offset [mm] | Hp | Hs | Hs/Hp |
| **10 MHz** | 5 | 5.9 | 14.19 | 11.34 | 1 | 4.99 | 5.99 | 4.97 |
| | 3.75 | 3.92 | 2.23 | 1.76 | 0.75 | 3.97 | 7.71 | 6.27 |
| | 2.5 | 2.91 | 3.9 | 2.21 | 0.5 | 2.81 | 6.77 | 5.6 |
| | 1.25 | 1.65 | 9.07 | 8.22 | 0.25 | 2.18 | 8.11 | 7.02 |
| | -1.25 | 0.45 | 7.04 | 7.29 | -0.25 | 1.03 | 7.34 | 7.91 |
| | -2.5 | 2.56 | 6.81 | 8.08 | -0.5 | 1.73 | 11.74 | 12.64 |
| | -3.75 | 3.42 | 17.5 | 18.86 | -0.75 | 2.67 | 7.88 | 9.52 |
| | -5 | 5.28 | 6.99 | 9.45 | -1 | 4.11 | 13.77 | 15.89 |
| | **Relative distance error [%]** | | | **Relative height error [%]** | | | |
| | TX offset [mm] | Hp | Hs | Hs/Hp | TX offset [mm] | Hp | Hs | Hs/Hp |
| **20 MHz** | 5 | 5.89 | 5.79 | 2.62 | 1 | 5 | 1.89 | 3.85 |
| | 3.75 | 3.92 | 2.08 | 1.91 | 0.75 | 3.97 | 2.39 | 2.66 |
| | 2.5 | 2.91 | 2.18 | 0.98 | 0.5 | 2.81 | 2.07 | 1.8 |
| | 1.25 | 1.65 | 2.93 | 1.88 | 0.25 | 2.18 | 2.73 | 1.54 |
| | -1.25 | 0.45 | 1.95 | 2.28 | -0.25 | 1.03 | 1.95 | 2.71 |
| | -2.5 | 2.56 | 1.51 | 2.93 | -0.5 | 1.73 | 3.32 | 4.64 |
| | -3.75 | 3.42 | 4.04 | 6.05 | -0.75 | 2.68 | 2.34 | 4.59 |
| | -5 | 5.27 | 2.01 | 4.23 | -1 | 4.12 | 3.7 | 6.86 |
| | **Relative distance error [%]** | | | **Relative height error [%]** | | | |
| | TX offset [mm] | Hp | Hs | Hs/Hp | TX offset [mm] | Hp | Hs | Hs/Hp |
| **25 MHz** | 5 | 5.89 | 4.3 | 2.62 | 1 | 5 | 1.19 | 2.44 |
| | 3.75 | 3.92 | 2.02 | 1.91 | 0.75 | 3.98 | 1.46 | 1.98 |
| | 2.5 | 2.91 | 1.86 | 0.98 | 0.5 | 2.81 | 1.26 | 1.15 |
| | 1.25 | 1.65 | 1.86 | 1.88 | 0.25 | 2.18 | 1.8 | 1.01 |
| | -1.25 | 0.45 | 1.09 | 2.28 | -0.25 | 1.03 | 1.04 | 1.42 |
| | -2.5 | 2.56 | 1.06 | 2.93 | -0.5 | 1.74 | 1.87 | 2.07 |
| | -3.75 | 3.42 | 2.13 | 6.05 | -0.75 | 2.68 | 1.38 | 3.86 |
| | -5 | 5.27 | 2.06 | 4.23 | -1 | 4.12 | 1.99 | 3.38 |

The sensor response for pitch and roll tilt angles is shown in **Figure 38** as the primary and secondary coupling $|H_P|$ and $|H_S|$, respectively, and for ratio $|U_S/U_P|$ in **Figure 39**. The reference position is shown with a blue circle. The TX coil is in a horizontal position, the RX coil is vertical, and they are mutually perpendicular. Pitch and roll tilt angles were varied for TX and RX coil from -3.75° to 3.75°. For each simulation run, one angle was changed while the rest were fixed to the reference position.

The change of the primary coupling $|H_P|$ is most pronounced for the TX pitch (red circles) and RX pitch (purple circles) angles as this angle variation changes their mutual orientation, so they are not perpendicular to each other. The primary coupling increases or decreases linearly for both TX and RX pitch angles, but the change is not symmetrical due to the TX coil offset from the center of the RX coil. The small changes in TX roll (yellow circles) and RX roll (green circles) angles have negligible effects on primary coupling, Figure 38(a). The secondary

coupling $|H_S|$ is noticeably affected only in the case of TX pitch change, and the changes due to the other tilt angles do not introduce significant errors. The variations are numerical noise due to the changes in the FEM mesh, Figure 38(b). Figure 39 shows that small variations in roll angles for both TX and RX coils change the ratio $|U_S/U_P|$, causing errors in the sensor data interpretation. The change in the TX pitch angle changes the ratio $|U_S/U_P|$ the most because this angle changes the mutual orientation of the coils and, consequently, primary coupling.



(a)                                                                                                (b)
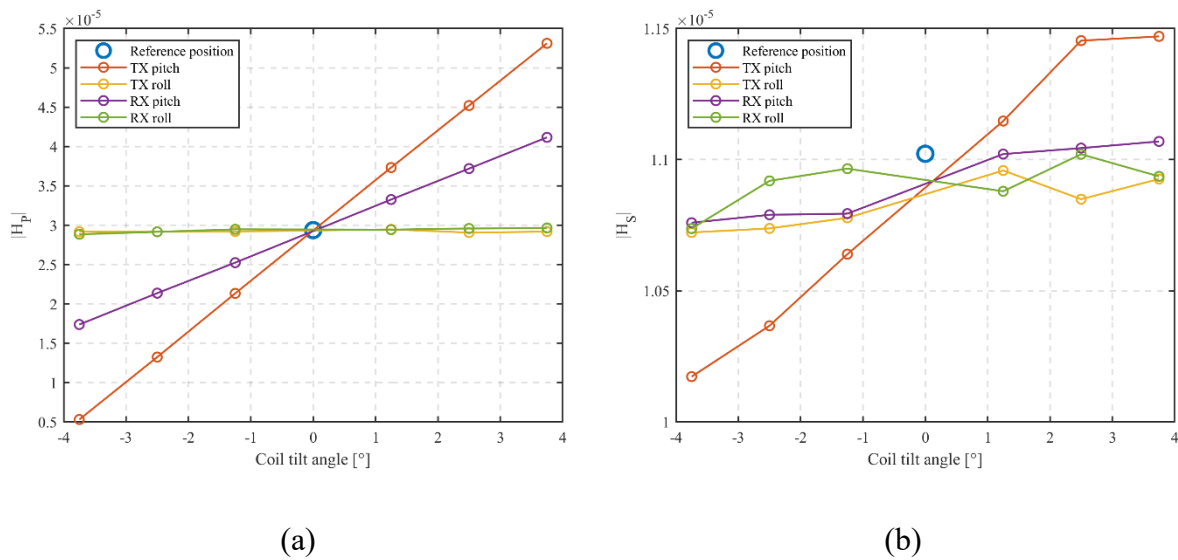
**Figure 38.** FEM analysis of transmitter coil til angles from the reference position (blue circle). Primary coupling (a) in the air and secondary coupling (b) above conductive medium with conductivity 60mS/m and permittivity 78. Results are shown for different tilt angles: TX pitch (red), TX roll (yellow), RX pitch (purple), and RX roll (green).
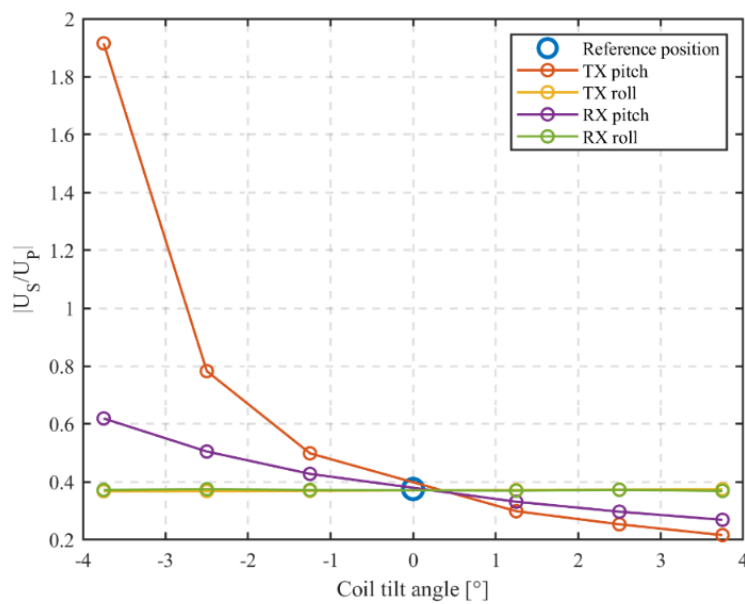


**Figure 39.** FEM analysis of transmitter coil til angles from the reference position (blue circle) for the ratio of $U_S/U_P$. Results are shown for different tilt angles: TX pitch (red), TX roll (yellow), RX pitch (purple), and RX roll (green).

The primary and secondary coupling errors, relative to the reference position $|H_{REF}|$, are calculated similarly to the previous case using the equation (120) for 10 MHz, 20 MHz, and 25 MHz, as shown in **Table 4**.

**Table 4.** Calculated coupling errors for TX pitch, TX roll, RX pitch, and RX roll angles at 10 MHz, 20 MHz, and 25 MHz.

**10 MHz**

| Tilt angle[°] | TX pitch error [%] | | | TX roll error [%] | | | RX pitch error [%] | | | RX roll error [%] | | |
|---|---|---|---|---|---|---|---|---|---|---|---|---|
| | Hp | Hs | Hs/Hp | Hp | Hs | Hs/Hp | Hp | Hs | Hs/Hp | Hp | Hs | Hs/Hp |
| 3.75 | 80.43 | 6.76 | 43.7 | 0.67 | 7.08 | 6.79 | 40.38 | 0.92 | 28.78 | 0.94 | 7.88 | 8.34 |
| 2.5 | 53.64 | 4.65 | 31.89 | 1.06 | 7.74 | 7.22 | 26.8 | 0.73 | 21.25 | 0.71 | 2.24 | 2.61 |
| 1.25 | 26.95 | 4.12 | 21.92 | 0.32 | 7.44 | 7.59 | 13.32 | 0.55 | 11.98 | 0.2 | 8.75 | 8.85 |
| -1.25 | 27.24 | 10.29 | 28.85 | 0.6 | 8.41 | 8.07 | 14.15 | 8.25 | 12.65 | 0.35 | 5.18 | 5.35 |
| -2.5 | 54.67 | 10.98 | 100.35 | 0.7 | 8.61 | 8.21 | 27.43 | 8.09 | 31.67 | 0.75 | 2.43 | 1.96 |
| -3.75 | 81.56 | 12.56 | 381.14 | 0.71 | 7.69 | 7.25 | 41.1 | 7.07 | 61.91 | 1.8 | 7.86 | 6.84 |

**20 MHz**

| Tilt angle | TX pitch error [%] | | | TX roll error [%] | | | RX pitch error [%] | | | RX roll error [%] | | |
|---|---|---|---|---|---|---|---|---|---|---|---|---|
| | Hp | Hs | Hs/Hp | Hp | Hs | Hs/Hp | Hp | Hs | Hs/Hp | Hp | Hs | Hs/Hp |
| 3.75 | 80.79 | 4.62 | 42.47 | 0.67 | 1.75 | 1.53 | 40.12 | 0.62 | 28.33 | 0.94 | 1.85 | 2.39 |
| 2.5 | 53.88 | 3.93 | 32.48 | 1.06 | 2.21 | 1.65 | 26.62 | 0.38 | 20.87 | 0.71 | 0.5 | 0.88 |
| 1.25 | 27.07 | 1.66 | 20.44 | 0.32 | 1.7 | 1.83 | 13.23 | 0.2 | 11.69 | 0.2 | 2.22 | 2.34 |
| -1.25 | 27.36 | 3.81 | 32.93 | 0.6 | 2.72 | 2.27 | 14.07 | 2.56 | 14.05 | 0.35 | 1.2 | 1.38 |
| -2.5 | 54.9 | 6.03 | 108.57 | 0.7 | 3.01 | 2.45 | 27.25 | 2.52 | 34.59 | 0.75 | 1.02 | 0.44 |
| -3.75 | 81.92 | 7.74 | 410.4 | 0.71 | 3.02 | 2.42 | 40.84 | 2.6 | 65.01 | 1.8 | 2.94 | 1.62 |

**25 MHz**

| Tilt angle | TX pitch error [%] | | | TX roll error [%] | | | RX pitch error [%] | | | RX roll error [%] | | |
|---|---|---|---|---|---|---|---|---|---|---|---|---|
| | Hp | Hs | Hs/Hp | Hp | Hs | Hs/Hp | Hp | Hs | Hs/Hp | Hp | Hs | Hs/Hp |
| 3.75 | 81.07 | 4.78 | 42.29 | 0.67 | 0.91 | 1.01 | 39.92 | 0.74 | 28.09 | 0.94 | 0.98 | 1.36 |
| 2.5 | 54.07 | 3.75 | 32.67 | 1.06 | 1.26 | 0.94 | 26.49 | 0.44 | 20.68 | 0.71 | 0.36 | 0.58 |
| 1.25 | 27.17 | 1.7 | 20.19 | 0.32 | 0.94 | 0.94 | 13.16 | 0.18 | 11.57 | 0.2 | 1.14 | 1.24 |
| -1.25 | 27.45 | 2.69 | 34.31 | 0.6 | 1.74 | 1.27 | 14 | 1.6 | 14.71 | 0.35 | 0.62 | 0.72 |
| -2.5 | 55.09 | 5.14 | 111.25 | 0.7 | 2.05 | 1.46 | 27.12 | 1.62 | 35.21 | 0.75 | 0.77 | 0.23 |

The change in the transmitter or receiver height mostly affects the primary coupling, which is minimal when the horizontal position of the transmitter is in the center of the receiver coil. The vertical offset of 1 mm from the defined position can change the primary coupling by 6%. The small variations in coil height do not significantly affect the secondary coupling through the soil. With the small increase in the mutual coil distance, the magnitude of the primary coupling decreases, but the secondary coupling slightly increases due to the more inspected volume. The change in a horizontal distance of 5 mm can change primary coupling by 5%. In both cases, the ratio US/UP is affected due to the primary coupling, and the height change is more significant than the change in the coil distance.

The change in the transmitter and receiver tilt angles dominantly affects the primary coupling, which depends on the mutual coil angle. It is minimal when the coils are mutually perpendicular and maximal in the case of horizontal or vertical coplanar orientations. The biggest source of error is the change of the transmitter pitch angle, which directly increases primary coupling in the order of 80% for an angle around 4°. Combined with height offset, it can sometimes flip the phase of the primary coupling. Overall, small variations in coil angles do not affect secondary coupling significantly.

# 4.4 Electrostatic shielding

The voltage induced in the receiver coil is a superposition of a primary voltage resulting from the direct inductive coupling with the transmitter and a secondary voltage due to the inductive coupling through the medium. There is also a capacitive coupling that can be direct between the coils and through the medium [83]. As the excitation frequency increases, the capacitive coupling can become comparable to inductive coupling and become an issue in HFEMI sensors. The capacitive coupling affects the sensor response and complicates data interpretation. In addition to capacitive parasitics, there is also a capacitive-inductive coupling between the coils and the medium, but this coupling is difficult to quantify compared to capacitive effects, as discussed in [83].

Electrostatic shielding is a standard procedure for minimizing capacitive coupling [117], [118]. Most EMI sensing studies, unrelated to soil sensing, approach this problem from the practical design perspective. However, limited attention is often given to the effectiveness or comparison of different shielding techniques and materials once implemented.

For instance, one study developed a magnetic tomography system operating at 10 MHz to measure the electrical conductivity and permittivity of the biological tissue [119]. The researchers compared measurements from unshielded coils and coils shielded with copper tape, finding that shielded coils provided more accurate results of dielectric permittivity. Another study described a magnetic tomography sensor for biomedical applications using a frequency range of 400 kHz to 12 MHz, consisting of one transmitter coil and two receiver coils positioned to minimize direct inductive coupling [120]. Audio cables were wound around each coil, acting as an electrostatic shield to reduce capacitive coupling. The tomography system in [121] was developed for the measurement of the electrical conductivity of the tissue using a gradiometer coil made of printed circuit board (PCB) coils, with the transmitter coil positioned between the two receiver coils. Patterned PCB shields were used on the top and bottom sides to minimize the capacitive coupling between the coils and tested objects. A study in [122] developed a magnetic induction spectroscopy system for bio-impedance measurement in the frequency range of 156 kHz to 2.5 MHz. Two receiver coils in gradiometer configuration minimized direct inductive and capacitive coupling, and an aluminum enclosure protected the sensor from external electromagnetic interference. Capacitive coupling between the sensor and test sample was mitigated with layers of graphite paint forming a low-conductivity electrostatic shield.

The relevant literature review concludes that no studies in HFEMI soil sensing have addressed the issue of capacitive coupling and the need for electrostatic shielding. This chapter

gives a more general analysis of coupling mechanisms in HFEMI soil sensing with a qualitative description of the main coupling mechanisms using an equivalent circuit model.

## 4.4.1 Equivalent circuit model

Following the analysis in [83], the equivalent circuit model of the experimental setup was derived, as shown in **Figure 40**. The sensor configuration determines the transmitter and receiver parameters, while the coaxial cable and low-pass filter parameters remain constant.
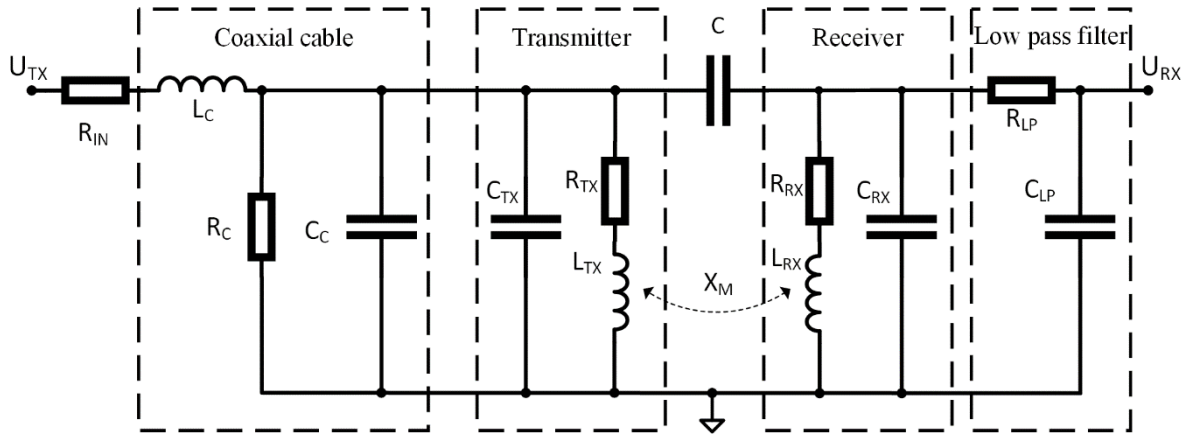


**Figure 40.** Equivalent circuit model of the experimental setup with shielded transmitter and receiver.

The modeled transfer function $H(\omega)$ is derived from the equivalent circuit model, given as

$$H\left(\omega,C,M,k\right) = \frac{U_{RX}}{U_{TX}} \ , \tag{121}$$

where $\omega$ is the angular frequency, $C$ is the mutual capacitance, $M$ denotes the mutual inductance, $k$ approximates frequency-dependent losses, and $X_M$ is the cross-impedance defined as:

$$X_M = j\omega M - k\omega^2 \ . \tag{122}$$

The transmitter and receiver are weakly coupled due to the intercoil separation and orientation, so $C$, $M$, and $k$ have low values relative to other circuit parameters. As a result, the transfer function $H$ can be approximated using a first-order Taylor expansion around $(C, M, k) = (0, 0, 0)$:

$$H\left(\omega,C,M,k\right) \approx h_C\left(\omega\right)C + h_M\left(\omega\right)M + h_k\left(\omega\right)k \ . \tag{123}$$

In this case, $h_C$, $h_M$, and $h_k$ are partial derivatives of $H$ with respect to $C$, $M$, and $k$. This simplification is justified, as computations using typical parameter values from Chapter 4.4.4 show no observable difference between the exact expression for $H$ and its approximation in (123). Relevant expressions for (123) are given in equations (124) to (131):

$$Z_{IN} = R_{IN} + j\omega L_c \ , \tag{124}$$

$$Z_{TX} = R_{TX} + j\omega L_{TX} \ , \tag{125}$$

$$Z_{RX} = R_{RX} + j\omega L_{RX} \ , \tag{126}$$

$$Y = R_C^{-1} + Z_{IN}^{-1} + j\omega\left(C_c + C_{TX}\right) \ , \tag{127}$$

$$Z_D = Z_{IN}\left(1 + YZ_{TX}\right)\left(1 + j\omega C_{LP}R_{LP} + Z_{RX}\left(j\omega C_{RX} + j\omega C_{LP} - \omega^2 C_{RX}C_{LP}R_{LP}\right)\right) \ , \tag{128}$$

$$h_M\left(\omega\right) = \frac{j\omega}{Z_D} \ , \tag{129}$$

$$h_k\left(\omega\right) = \frac{-\omega^2}{Z_D} \ , \tag{130}$$

$$h_C\left(\omega\right) = \frac{j\omega Z_{TX}Z_{RX}}{Z_D} \ . \tag{131}$$

Equations (125) and (126) are transmitter and receiver impedances $Z_{TX}$ and $Z_{RX}$ without their capacitances $C_{TX}$ and $C_{RX}$, respectively. A phase difference between $h_M$ in (129) and $h_C$ in (131), results from the product of $Z_{TX}$ and $Z_{RX}$. At frequencies above 1 MHz, impedances are primarily inductive, with the phase close to 90°, meaning that the phase difference between $h_M$ and $h_C$ is 180°. This phase difference is independent of the transmitter-receiver separation since only $C$, $M$, and $k$ depend on the separation.

## 4.4.2 Experimental procedure and model parameter estimation

The sensor transfer function, denoted as $H_e$, was measured for two different transmitter coil orientations, **Figure 41**. First, the sensor transfer function $H_{e,up}$ was measured with the transmitter coil facing upwards, **Figure 41**(a). Next, the transmitter coil was flipped downwards, and the sensor transfer function $H_{e,down}$ was measured, **Figure 41**(b). In both cases, the capacitive coupling remains the same since the relative positions of all conductive surfaces (such as copper traces and parts of the experimental setup) are unchanged, but the inductive coupling altered its sign with the change of orientation.
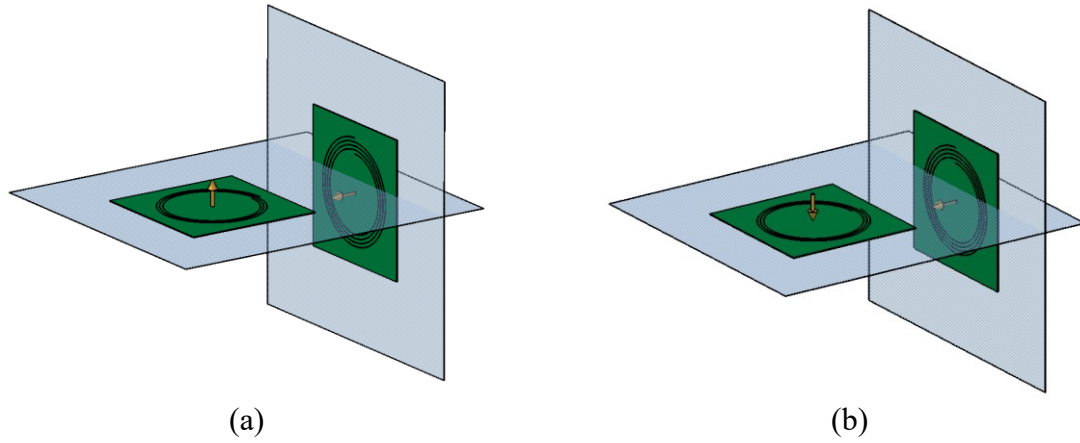
**Figure 41.** Sensor coils orientation: (a) horizontal transmitter coil oriented up, vertical receiver coil, (b) horizontal transmitter coil oriented down, vertical receiver coil.

The equivalent circuit parameters for calculating $h_C$, $h_M$, and $h_k$ were determined using an impedance analyzer before measuring the sensor transfer function. $C$, $M$, and $k$ values were estimated by fitting the equation (123) to the measured transfer functions $H_{e,up}$ and $H_{e,down}$ through linear least-squares regression across the relevant frequency range. For each measured frequency $\omega$, the pair of equations are:

$$H_{e,up}(\omega) = h_C(\omega) \cdot C + h_M(\omega) \cdot M + h_k(\omega) \cdot k \ , \tag{132}$$

$$H_{e,down}(\omega) = h_C(\omega) \cdot C - h_M(\omega) \cdot M - h_k(\omega) \cdot k \ . \tag{133}$$

For $H_{e,up}$, the inductive coupling parameters $M$ and $k$ have a positive sign, while for $H_{e,down}$ they have a negative sign. The overdetermined system with *2n* equations, where *n* is the number of measurement frequencies, is then constructed as:

$$\begin{bmatrix} H_{e,up}(\omega_1) \\ H_{e,down}(\omega_1) \\ \vdots \\ \vdots \\ H_{e,up}(\omega_n) \\ H_{e,down}(\omega_n) \end{bmatrix} = \begin{bmatrix} h_C(\omega_1) & h_M(\omega_1) & h_k(\omega_1) \\ h_C(\omega_1) & -h_M(\omega_1) & -h_k(\omega_1) \\ & \vdots & \\ & \vdots & \\ h_C(\omega_n) & h_M(\omega_n) & h_k(\omega_n) \\ h_C(\omega_n) & -h_M(\omega_n) & -h_k(\omega_n) \end{bmatrix} \begin{bmatrix} C \\ M \\ k \end{bmatrix} . \tag{134}$$

Since there is a 180° phase difference between $h_C$ and $h_M$, the capacitive and inductive coupling components in (132) have opposite phases, reducing the overall coupling. In the case of (133), the sign of the inductive coupling changes, causing the capacitive and inductive coupling components to be in phase, and thus, the overall coupling is increased.

### 4.4.3 Summary of the method for electrostatic shielding evaluation

The outlined procedure is suitable for weakly coupled EMI sensors, meaning the transmitter and receiver coils are positioned far enough apart so that the mutual inductances and capacitances are significantly smaller than the individual coil inductances and capacitances. Applications include EMI soil sensors, tomography, and spectroscopy systems. The following steps provide an overview of the method for assessing electrostatic shielding effectiveness:

1. Develop an equivalent circuit model for a high-frequency EMI (HFEMI) sensor without the medium under investigation, i.e., the sensor in the air.

2. Linearize the derived model for the inductive and capacitive coupling parameters.

3. Measure the impedance of each shielded coil in the sensor and estimate the parameters of its equivalent circuit using a laboratory impedance analyzer. The estimated parameters serve as the parameters of the linearized HFEMI sensor model.

4. Measure the sensor responses for two opposite transmitter orientations. If the transmitter cannot be reoriented, change the direction of the excitation current instead.

5. Estimate the coupling parameters using the linearized model and the measured sensor response.

### 4.4.4 Measurement and estimation of equivalent circuit parameters

Transmitter and receiver equivalent circuit model parameters, **Figure 42**, for both the transmitter and receiver are given in **Table 5** for each coil and shield combination, as measured with the Agilent 4294A impedance analyzer.



(a)                                                        (b)
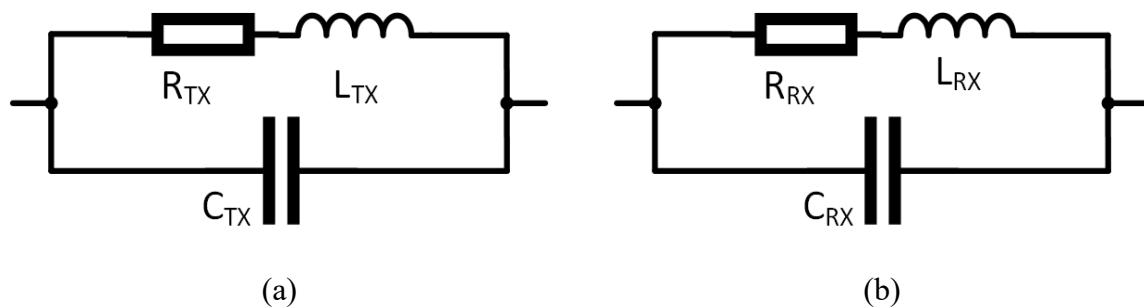
**Figure 42.** Equivalent circuit parameters model: **(a)** transmitter and **(b)** receiver.

The columns in **Table 5**, **Table 7**, and **Table 8** represent various shield patterns (C or X) and coil-shield spacings in millimeters. For instance, C-4 indicates a C pattern shield with a 4 mm spacing from a coil. Receiver capacitance ($C_{RX}$) and transmitter capacitance ($C_{TX}$) account for coil self-capacitance and coil-shield capacitance, which are influenced by the shielding pattern and coil spacing. Receiver inductance ($L_{RX}$), transmitter inductance ($L_{TX}$), and their

corresponding series resistances ($R_{RX}$ and $R_{TX}$) are determined by the coil geometry, as well as the skin and proximity effects in the copper traces of the coils and shields. **Table 6** presents the equivalent circuit parameters for the coaxial cable and low-pass filter. The filter capacitance ($C_{LP}$) is the sum of the receiver amplifier input and filter capacitance.

**Table 5.** Transmitter and receiver equivalent circuit parameters

| | C-2 | C-4 | C-6 | X-2 | X-4 | X-6 |
|---|---|---|---|---|---|---|
| $L_{TX}$ [μH] | 1.101 | 1.117 | 1.124 | 1.084 | 1.108 | 1.117 |
| $C_{TX}$ [pF] | 12.05 | 9.78 | 9.04 | 11.68 | 9.58 | 8.77 |
| $R_{TX}$ [Ω] | 0.345 | 0.351 | 0.347 | 0.301 | 0.29 | 0.286 |
| $L_{RX}$ [μH] | 1.489 | 1.517 | 1.528 | 1.485 | 1.519 | 1.527 |
| $C_{RX}$ [pF] | 13.71 | 10.73 | 9.47 | 13.27 | 10.53 | 9.24 |
| $R_{RX}$ [Ω] | 0.399 | 0.386 | 0.404 | 0.428 | 0.421 | 0.409 |

**Table 6.** Coaxial cable and low-pass filter equivalent circuit parameters

| | **Coaxial cable** |
|---|---|
| $L_k$ [nH] | 40 |
| $C_C$ [pF] | 18.5 |
| $R_k$ [kΩ] | 716 |
| | **Low-pass filter** |
| $C_{LP}$ [pF] | 6.9 |
| $R_{LP}$ [Ω] | 499 |

The coupling parameters $C$, $M$ and $k$ are estimated using the procedure in Section 4.4.3 for the measurement data up to 20 MHz to avoid the coil resonance effects. The results are given in **Table 7** for transmitter-receiver separation of 27 cm and in **Table 8** for 37 cm separation. Different sensor configurations were tested (6 x 6, 2 shield patterns and 3 coil-shield spacings for the transmitter and the receiver) for 36 combinations. Two measurements were made for each configuration: first, with the transmitter coil oriented up and then oriented down. For a given transmitter-receiver separation, the mutual inductance $M$ and losses $k$ are similar for all configurations, which means that the inductive coupling is not significantly affected by changing the shield pattern and coil-shield spacing. The mutual capacitance $C$ depends on the configuration. It can be negligible in some configurations (estimated $C$ is zero) but generally increases as the coil-shield spacing increases.

**Table 7.** Estimated model parameters: 27 cm intercoil separation.

| | | Transmitter coil (TX) | | | | | | |
|---|---|---|---|---|---|---|---|---|
| | | **C-2** | **C-4** | **C-6** | **X-2** | **X-4** | **X-6** | |
| **Receiver coil (RX)** | **C-2** | 66.63 | 68.11 | 67.59 | 65.67 | 66.85 | 67.66 | *M* [pH] |
| | **C-4** | 68.06 | 68.58 | 68.24 | 66.92 | 67.87 | 65.25 | |
| | **C-6** | 69.22 | 69.71 | 69.58 | 68.48 | 69.31 | 69.68 | |
| | **X-2** | 62.69 | 63.83 | 63.55 | 61.34 | 62.68 | 63.09 | |
| | **X-4** | 65.31 | 66.02 | 65.13 | 64.16 | 65.5 | 64.89 | |
| | **X-6** | 67.83 | 68.63 | 68.36 | 67.24 | 68.29 | 68.49 | |
| | **C-2** | 5.1 | 5.2 | 5.2 | 4.9 | 5 | 5 | *k* [0.1 pH/MHz] |
| | **C-4** | 5.2 | 5.3 | 5.1 | 5 | 5.1 | 5 | |
| | **C-6** | 5.3 | 5.4 | 5.2 | 5.3 | 5.4 | 5.4 | |
| | **X-2** | 4.8 | 4.8 | 4.9 | 4.6 | 4.8 | 4.8 | |
| | **X-4** | 4.9 | 5 | 5.1 | 5 | 5.1 | 5 | |
| | **X-6** | 5.3 | 5.3 | 5.6 | 5.8 | 5.4 | 5.4 | |
| | **C-2** | 0 | 0 | 0 | 0 | 0 | 0 | *C* [$10^{-17}$ F] |
| | **C-4** | 0 | 0 | 3.6 | 1.3 | 2.8 | 8.7 | |
| | **C-6** | 0 | 2.7 | 10.3 | 8.1 | 14.2 | 21.2 | |
| | **X-2** | 0 | 0 | 3.3 | 0 | 2.9 | 9.8 | |
| | **X-4** | 0 | 3.2 | 10.4 | 9.8 | 14.4 | 23.2 | |
| | **X-6** | 0 | 8 | 18.2 | 16.4 | 24.3 | 34.7 | |

**Table 8.** Estimated model parameters: 37 cm intercoil separation.

| | | Transmitter coil (TX) | | | | | | |
|---|---|---|---|---|---|---|---|---|
| | | **C-2** | **C-4** | **C-6** | **X-2** | **X-4** | **X-6** | |
| **Receiver coil (RX)** | **C-2** | 19.09 | 19.39 | 18.91 | 18.76 | 19.23 | 18.7 | *M* [pH] |
| | **C-4** | 20.02 | 20.23 | 20.59 | 19.75 | 20.27 | 20.34 | |
| | **C-6** | 21.12 | 21.88 | 21.32 | 20.79 | 21.85 | 21.3 | |
| | **X-2** | 18.03 | 18.23 | 19.31 | 17.82 | 18.2 | 19.25 | |
| | **X-4** | 19.56 | 19.68 | 20.21 | 19.45 | 19.82 | 20.19 | |
| | **X-6** | 21.07 | 21.26 | 21.22 | 20.88 | 21.44 | 21.31 | |
| | **C-2** | 0.7 | 0.7 | 0.7 | 0.7 | 0.7 | 0.7 | *k* [0.1 pH/MHz] |
| | **C-4** | 0.8 | 0.8 | 0.8 | 0.8 | 0.8 | 0.8 | |
| | **C-6** | 0.9 | 0.9 | 0.8 | 0.9 | 0.9 | 0.9 | |
| | **X-2** | 0.7 | 0.7 | 0.8 | 0.7 | 0.7 | 0.8 | |
| | **X-4** | 0.8 | 0.8 | 0.8 | 0.8 | 0.8 | 0.8 | |
| | **X-6** | 0.9 | 0.9 | 0.9 | 0.9 | 0.9 | 0.9 | |
| | **C-2** | 0 | 0 | 0 | 0 | 0 | 0.6 | *C* [$10^{-17}$ F] |
| | **C-4** | 0 | 1.5 | 5.7 | 4.7 | 6.2 | 10.3 | |
| | **C-6** | 0.5 | 5.3 | 11 | 10.3 | 15.3 | 20.2 | |
| | **X-2** | 0 | 2.2 | 5.4 | 5 | 8.4 | 11 | |
| | **X-4** | 1.1 | 5.6 | 11.4 | 10.8 | 15.8 | 20.5 | |
| | **X-6** | 2.6 | 9.7 | 17.8 | 16.8 | 24.6 | 31 | |

## 4.4.5 Effects of shielding on the sensor transfer function

The magnitude and phase spectra of the sensor transfer function $H$ for the TX C - 6 / RX C - 6 sensor configuration are shown in **Figure 43** for a frequency range from 1 MHz to 35 MHz. The spectra depend on the transmitter orientation (blue for up, red for down) and the transmitter-receiver separation (A - 27 cm, B - 37 cm). The resonant peak for all cases in **Figure 43** occurs at 32 MHz, primarily determined by the receiver parameters ($L_{RX}$ and $C_{RX}$) and the input impedance of the low-pass filter and receiver amplifier.

In the results, the sensor transfer functions for the intercoil separation appear similar for both transmitter orientations, up to 13 MHz. Beyond that point, the difference becomes more pronounced, arising from the inductive and capacitive coupling components, which, according to the model, are either in-phase or 180° out of phase. When the transmitter is oriented downwards, the inductive and capacitive coupling components are in phase, leading to an increased receiver voltage. Conversely, when the transmitter is oriented upwards, the phase angle of the inductive coupling flips, while the capacitive coupling remains unchanged, causing the receiver voltage to decrease.

Furthermore, the sensor transfer function magnitude for a 27 cm separation is approximately 3.5 times larger than that of a 37 cm separation. However, the phase of the receiver voltage does not noticeably depend on the separation, as shown in **Figure 43**(b), indicating that the phase relationship between the inductive and capacitive components remains constant for the response in the air. The model also supports this observation.
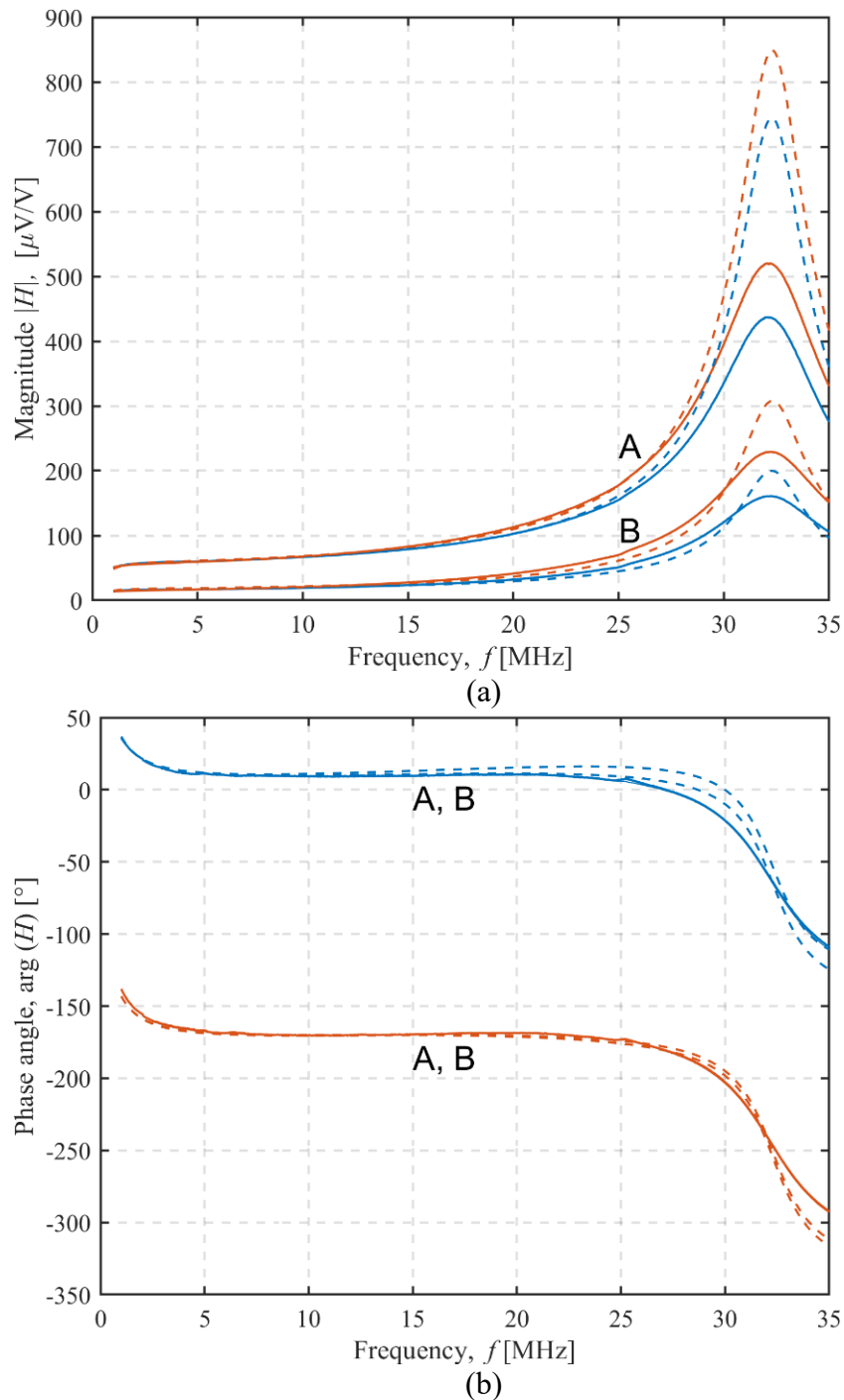
**Figure 43**. TX C-6 / RX C-6 configuration: (a) magnitude and (b) phase characteristics of the sensor.
Measurement (full line) and model results (dashed line). Transmitter orientation up (blue line) or down (red line).
Transmitter-receiver separation 27 cm (A) or 37 cm (B).

The dashed lines in **Figure 43** show the magnitude and phase spectra derived from the model using the electromagnetic coupling parameters from **Table 7** and **Table 8**. The model results and the measurement data agree to up to 20 MHz. Since the model does not consider resonance damping due to the skin effect of the copper traces and coil-shield proximity effect, the upper-frequency limit of further experimental analysis is set at 20 MHz.

The magnitude of the measured and modeled sensor transfer function for 4 of the 36 sensor configurations tested are shown in **Figure 44** through **Figure 47**. In **Figure 44**, the transmitter and receiver have C-shields spaced 2 mm apart (TX C-2 / RX C-2 configuration). There is only a minor frequency-independent difference between the spectra for both transmitter orientations due to small changes in mutual inductance when the transmitter orientation is changed manually. The result is a height misalignment between the transmitter orientations. No other differences are observed, and the estimated mutual capacitance $C$ is zero, **Table 7** and **Table 8**, resulting in identical modeled transfer functions for both orientations. In **Figure 45**, the transmitter has a C-shield, and the receiver has an X-shield, both spaced 4 mm apart (TX C-4 / RX X-4), in **Figure 46**, both have X-shields spaced 4 mm apart (TX X-4 / RX X-4), while in **Figure 47**, the X-shields are spaced 6 mm apart (TX X-6 / RX X-6).

In contrast to **Figure 44**, the differences between the magnitudes of the sensor transfer functions for both transmitter orientations for rest configurations increase with the frequency and the coupling capacitance $C$. The lowest coupling capacitance $C$ is found in **Figure 45**, and the highest is in **Figure 47**, **Table 7**, and **Table 8**. The capacitive coupling $C$ is lower for higher capacitances $C_{RX}$ and $C_{TX}$, **Table 5**. Capacitances $C_{RX}$ and $C_{TX}$ are higher at smaller spacings and slightly higher with C-shields than with X-shields, **Table 5**. At the lower frequencies, the difference between the magnitude spectra for both transmitter orientations is dominantly caused by the small changes in mutual inductance due to the transmitter height misalignment, but this is overcome by the capacitive coupling that becomes a dominant cause of the difference at a crossing frequency near 5 MHz.
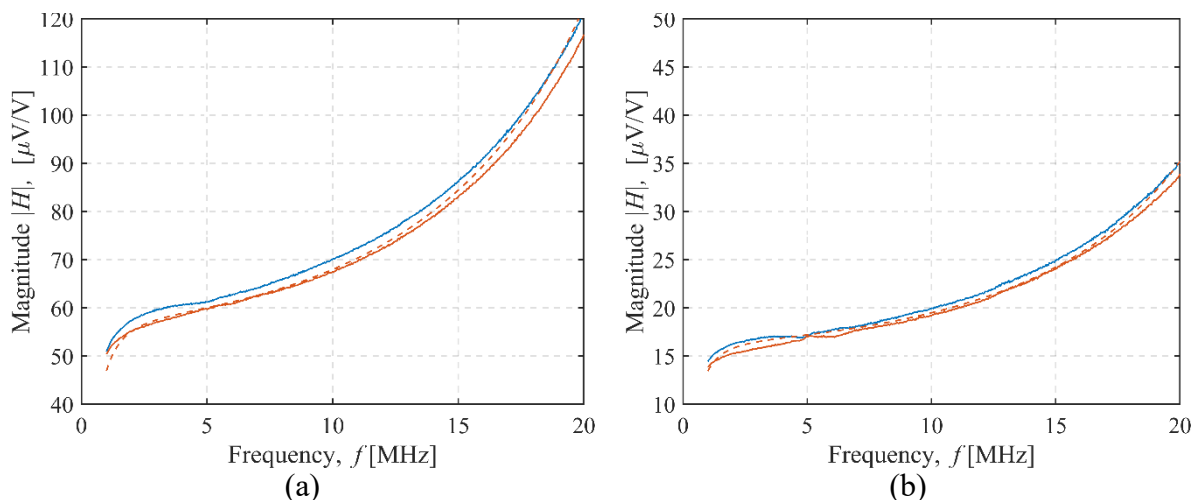


**Figure 44**. TX C-2 / RX C-2 configuration. Sensor transfer function magnitude. Transmitter-receiver separation: (a) 27 cm, (b) 37 cm. Measurement (full line) and model results (dashed line). Transmitter orientation up (blue line) or down (red line).

(a)                                                                 (b)
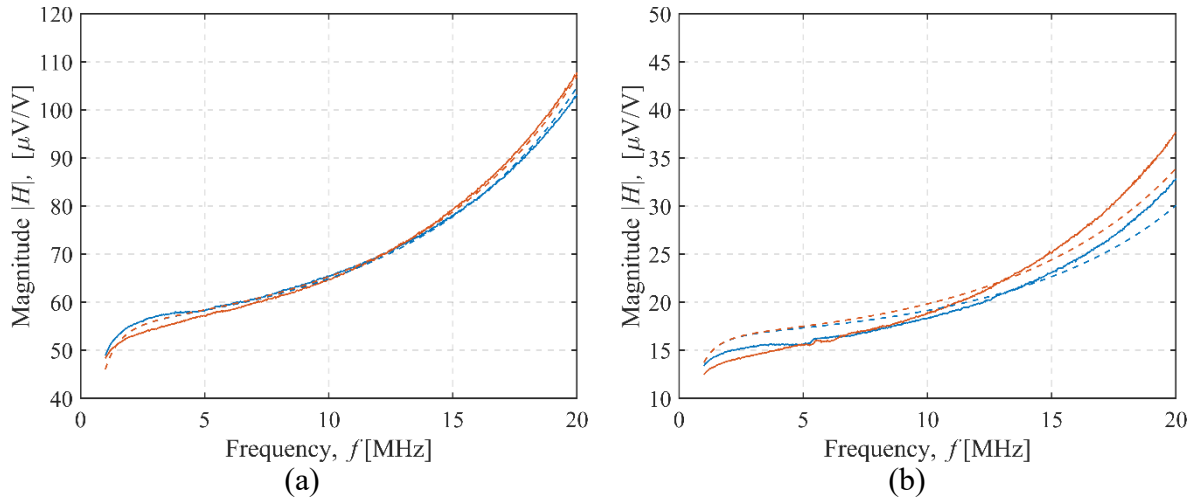
**Figure 45.** TX C-4 / RX X-4 configuration. Sensor transfer function magnitude. Transmitter-receiver separation: (a) 27 cm, (b) 37 cm. Measurement (full line) and model results (dashed line). Transmitter orientation up (blue line) or down (red line).



(a)                                                                 (b)
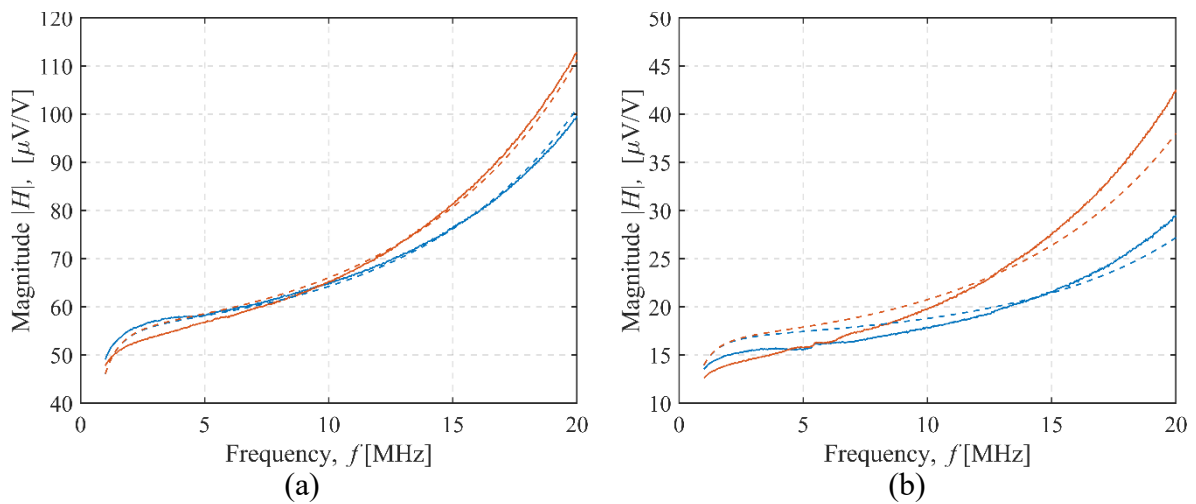
**Figure 46.** TX X-4 / RX X-4 configuration. Sensor transfer function magnitude. Transmitter-receiver separation: (a) 27 cm, (b) 37 cm. Measurement (full line) and model results (dashed line). Transmitter orientation up (blue line) or down (red line).



(a)                                                                 (b)
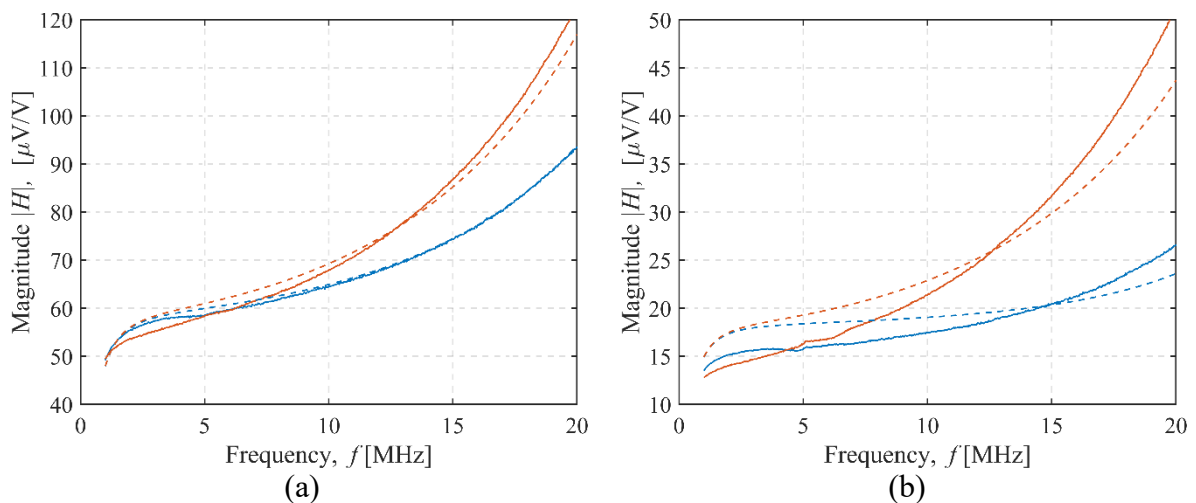
**Figure 47.** TX X-6 / RX X-6 configuration. Sensor transfer function magnitude. Transmitter-receiver separation: (a) 27 cm, (b) 37 cm. Measurement (full line) and model results (dashed line). Transmitter orientation up (blue line) or down (red line).

## 4.4.6 Validation of shield effectiveness in the presence of the conductive medium

The shielding effect was demonstrated by measuring the sensor response above the container filled with 60 liters of saline water with an electrical conductivity of 1 S/m and a dielectric permittivity of 78, **Figure 48**. The saline water is used to emulate the soil because it has similar electromagnetic properties and allows easier control of the electrical conductivity. First, the sensor response in the air was measured, and then the response above the saline water was measured. Two different shield configurations were evaluated (TX C-2 / RX C-2 and TX X-6 / RX X-6). Intercoil separation was 27 cm, and the sensor lift-off above the saline water was 11 cm, measured from the transmitter. The experimental setup and instrumentation are the same as described for other experiments.



**Figure 48.** The photograph of the sensor above the container filled with saline water.

The measurement results were compared with the 3D full-wave finite element method (FEM) analysis using CST studio suite 2021 software (Dassault Systèmes Simulia) [92]. The FEM model, equivalent to the measurement setup geometry, is shown in **Figure 49**. The saline water was modeled as a homogeneous medium with dimensions of 58.3cm x 37.2cm x 28.3 cm, an electrical conductivity of 1 S/m, and a dielectric permittivity of 78. The medium parameters were set to an electric conductivity of 0 S/m and dielectric permittivity of 1 to simulate the sensor response in the air. The boundary of the FEM model was set at 100 cm from the medium. The mesh grid consisted of 580,133 elements.
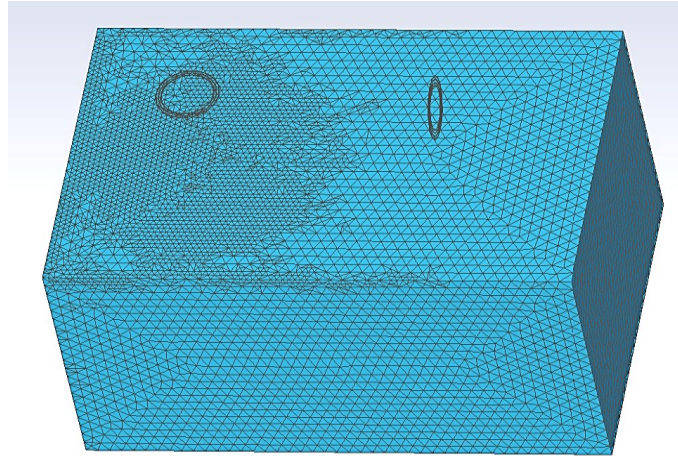
**Figure 49.** Sensor geometry and mesh grid of the medium used in FEM analysis.

The measurement results for the two sensor configurations (TX C-2 / RX C-2 and TX X-6 / RX X-6) and the FEM results in the complex plane are shown in **Figure 50**. The measurements (full line) are compared with the FEM analysis (dashed line) for both transmitter orientations (blue line for up, red line for down) in the frequency range from 1 MHz (dot) to 20 MHz (cross). An effective shield reduces the capacitive coupling component of both the primary and secondary voltages so that their ratio is predominantly due to inductive coupling and, consequently, is in better overall agreement with the FEM model results. It was shown that the TX C-2 / RX C-2 configuration has negligible capacitive coupling compared to the TX X-6 / RX X-6 configuration, hence better overall agreement of the former with the FEM model. This case study demonstrates that the proposed method, summarized in Section 4.4.3, is appropriate for evaluating the shielding effectiveness.



(a)  (b)
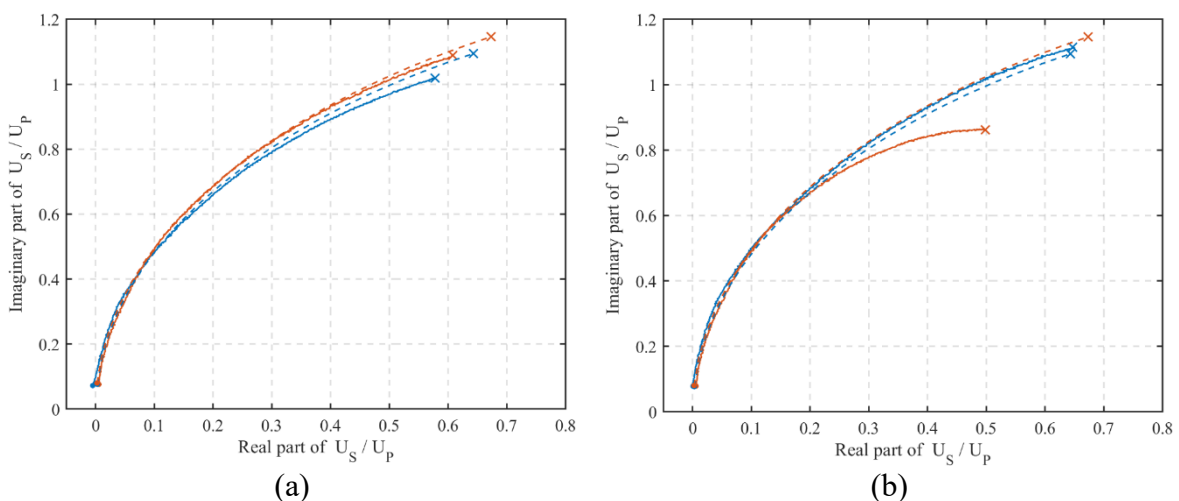
**Figure 50.** Secondary to primary induced voltage ratio: (a) TX C-2 / RX C-2 configuration, (b) TX X-6 / RX X-6 configuration. Measurement (full line) and FEM analysis (dashed line). Transmitter orientation up (blue line) or down (red line).

# Chapter 5

# Results

## 5.1 Laboratory measurements

The sensitivity to electrical conductivity and dielectric permittivity of the HFEMI soil sensor was evaluated in the laboratory. The laboratory setup is described in Chapter 3.3, and the measurement procedure is in Chapter 3.4. The measurements are compared with the FEM model described in Chapter 3.5.

### 5.1.1 Measurement of electrical conductivity

The sensor response $U_S/U_P$ was evaluated experimentally and by FEM. The sensitivity to electrical conductivity was assessed with laboratory measurements by adding the salt to the container filled with deionized water and then to the sucrose-water solution. The salt was added to 61.5 L of deionized water in steps ranging from 0.5 g to 8 g, increasing conductivity to 305 mS/m, measured with the laboratory handheld conductometer WTW 430i, **Table 9**. A substantially larger amount of salt was used for the experimental run with a sucrose-water solution to obtain similar conductivity levels, **Table 10**.

**Table 9.** Electrical conductivity of the saline water, depending on the added salt mass to 61.5 L of deionized water, measured with a conductometer WTW 340i.

| Salt [g] | Conductivity [mS/m] | Salt [g] | Conductivity[mS/m] |
|---|---|---|---|
| 0 | 0.49 | 16 | 57.6 |
| 0.5 | 1.75 | 20 | 70 |
| 1 | 4.72 | 26 | 87.5 |
| 1.5 | 6.25 | 32 | 104.8 |
| 2 | 9.53 | 40 | 128.1 |
| 3 | 13.43 | 50 | 159 |
| 4 | 17.57 | 60 | 189.8 |
| 5 | 22 | 70 | 221 |
| 6 | 25.6 | 80 | 251 |
| 8 | 32.4 | 88 | 281 |
| 10 | 39 | 96 | 305 |
| 12 | 45.2 | | |

**Table 10.** Electrical conductivity of the saline water depending on the mass of the added salt to 61.5 L sucrose water solution with relative permittivity 62, measured with conductometer WTW 340i.

| Salt [g] | Conductivity [mS/m] | Salt [g] | Conductivity [mS/m] | Salt [g] | Conductivity [mS/m] |
|---|---|---|---|---|---|
| 0 | 0.7 | 35 | 11.8 | 525 | 147.1 |
| 0.5 | 0.9 | 55 | 18 | 600 | 167.4 |
| 1 | 1.16 | 75 | 23.8 | 700 | 192 |
| 2 | 1.57 | 100 | 31.5 | 800 | 220 |
| 3 | 1.96 | 150 | 46.2 | 900 | 245 |
| 5 | 2.54 | 200 | 60.2 | 1000 | 269 |
| 7 | 3.26 | 250 | 74.2 | 1110 | 297 |
| 11 | 4.46 | 300 | 87.1 | 1138 | 300 |
| 15 | 5.75 | 375 | 106.8 | | |
| 25 | 8.89 | 450 | 126.6 | | |

The real and imaginary parts of the sensor response $U_S/U_P$ in the dependence on the electrical conductivity with the frequency as the parameter are shown in **Figure 51**. The experimental run with the deionized water with a relative permittivity of 78 is shown in **Figure 51** (a) and (c), and the experimental run with a sucrose-water of permittivity 62 is in **Figure 51** (b) and (d). The imaginary parts of both runs are more sensitive to the electrical conductivity, and for frequencies up to 20 MHz, the sensor response increases linearly for the whole range of measured conductivities. The real part of the sensor response also changes with the conductivity, shown in **Figure 51** (a), indicating that the low-induction number approximation is no longer valid in the frequency range above 5 MHz.

(a)

(b)

(c)

(d)
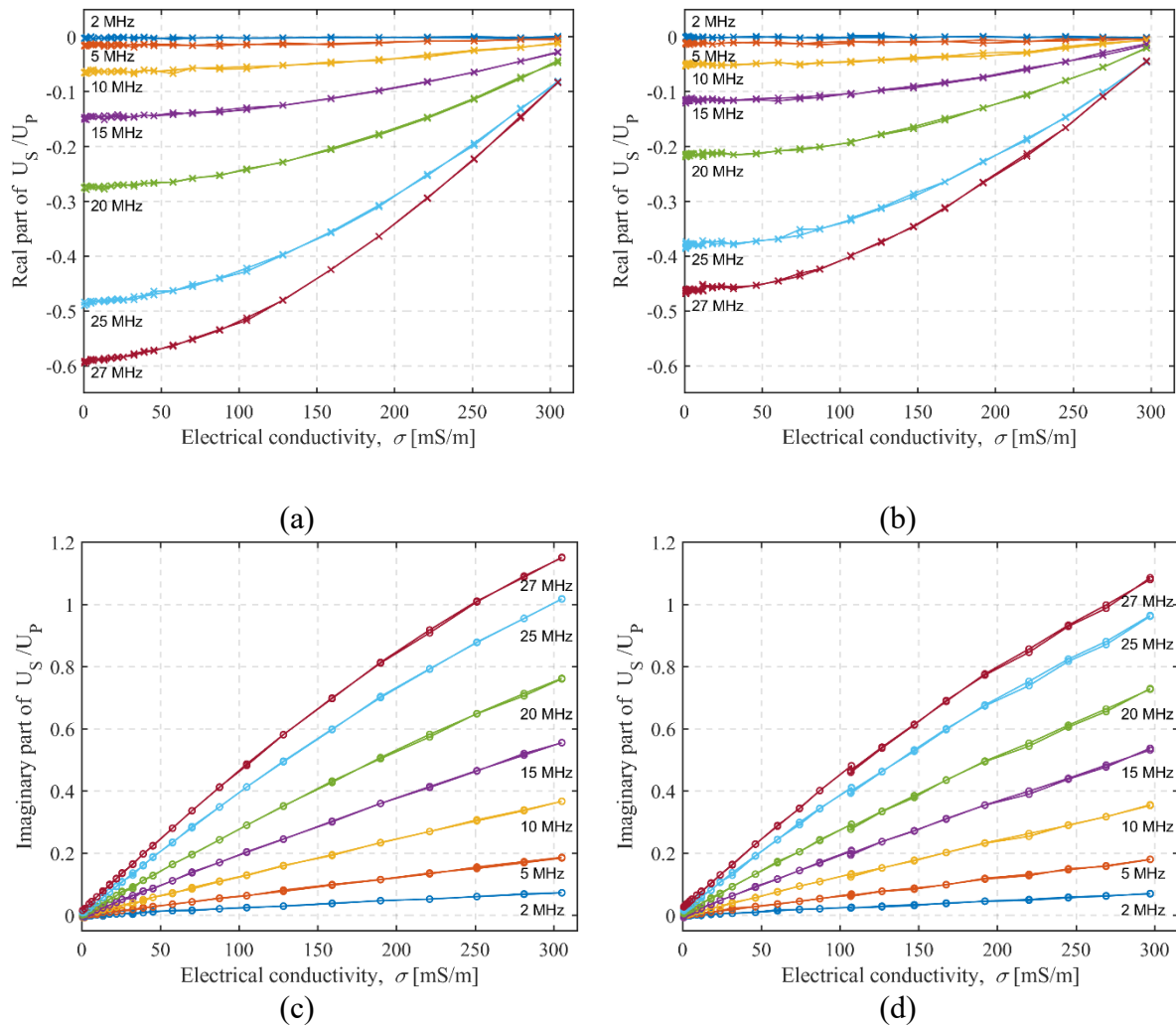
**Figure 51.** Measured electrical conductivity from 0 to 305 mS/m for 2, 5, 10, 15, 20, 25, and 27 MHz: (a) Real part of $U_S/U_P$, (b) Imaginary part of $U_S/U_P$.

The sensor response to the low electrical conductivity values from 0 to 35 mS/m is shown in **Figure 52**, (a) and (c) for deionized water, and (b) and (d) for sucrose-water solution. As conductivity decreases towards zero, the real part of $U_S/U_P$ converges to the offset value corresponding to the permittivity of the medium. This can be observed in **Figure 52** (a) and (b) as the offset decreases for the sucrose-water solution when comparing the same frequencies as the deionized water. For the low electrical conductivity values, the imaginary part of the sensor response is linear with the conductivity increasing in the whole frequency range. From **Figure 52** (b) and (d), the estimated resolution of the measurement is below 2 mS/m for the frequencies above 20 MHz, 5 mS/m for the frequency range between 10 MHz and 20 MHz, and approximately 20 mS/m for the lower end of the frequency range below 10 MHz.

The FEM results shown in **Figure 53** correspond to **Figure 51**, and the simulation results agree well qualitatively with the experimental results. There is a relative discrepancy between 10% and 20%, and the two main sources of this error are the effect of shielding and small coil misalignment in the experiment, which are not present in the FEM model.

The same measurement results are shown in **Figure 54**. in the complex plane for conductivities for 0 to 305 mS/m to illustrate the influence on both real and imaginary parts of the sensor response. For lower frequencies, sensitivity to conductivity is smaller, but the response is mainly in the imaginary part of the signal, enabling easier interpretation of the data. In the higher frequency range, the sensitivity to conductivity greatly increases, but both real and imaginary components are affected, making the data interpretation more complicated.
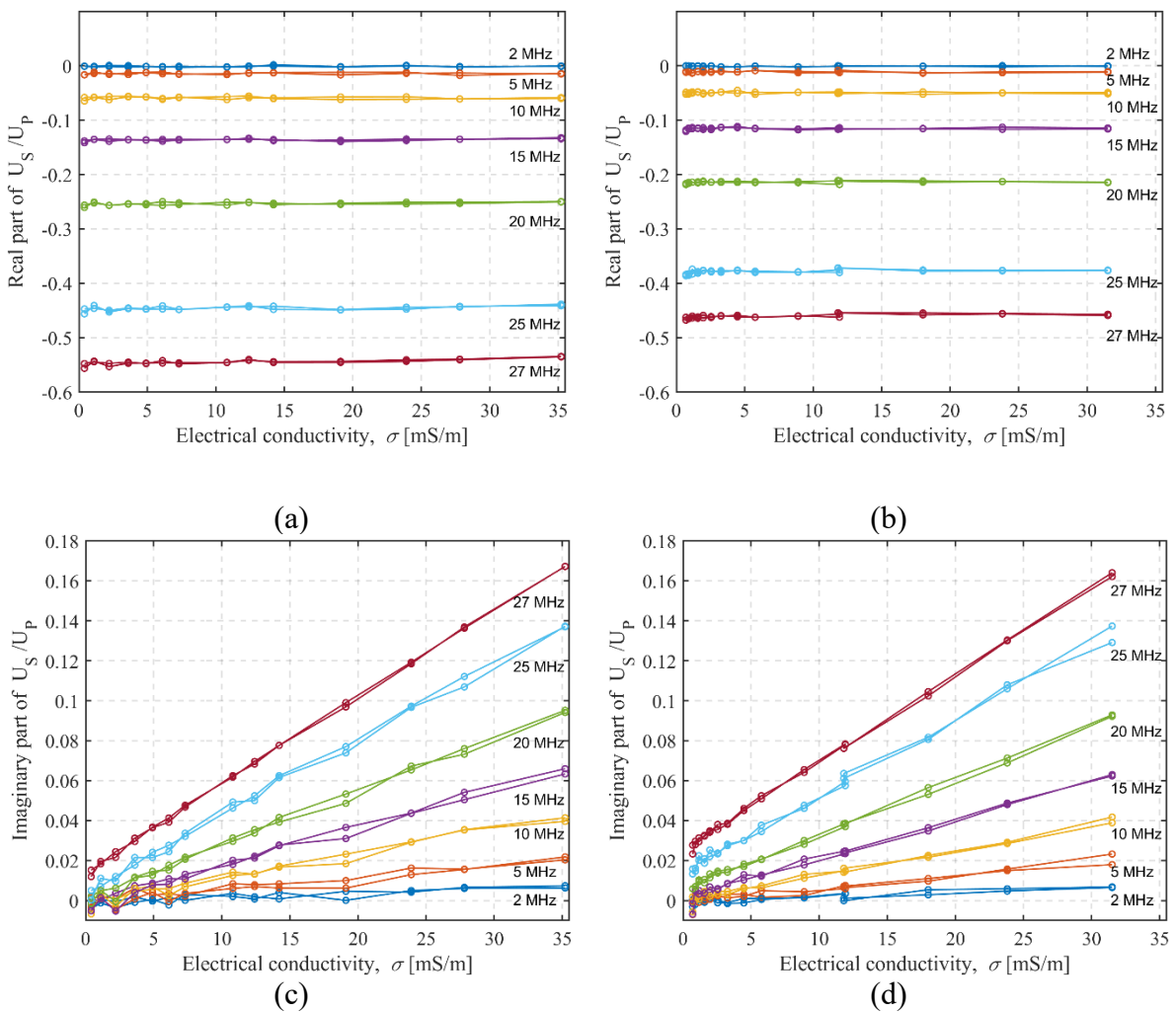


**Figure 52.** Measured electrical conductivity from 0 to 35 mS/m for 2, 5, 10, 15, 20, 25, and 27 MHz: (a) Real part of $U_S/U_P$, (b) Imaginary part of $U_S/U_P$.

(a)                                                                          (b)
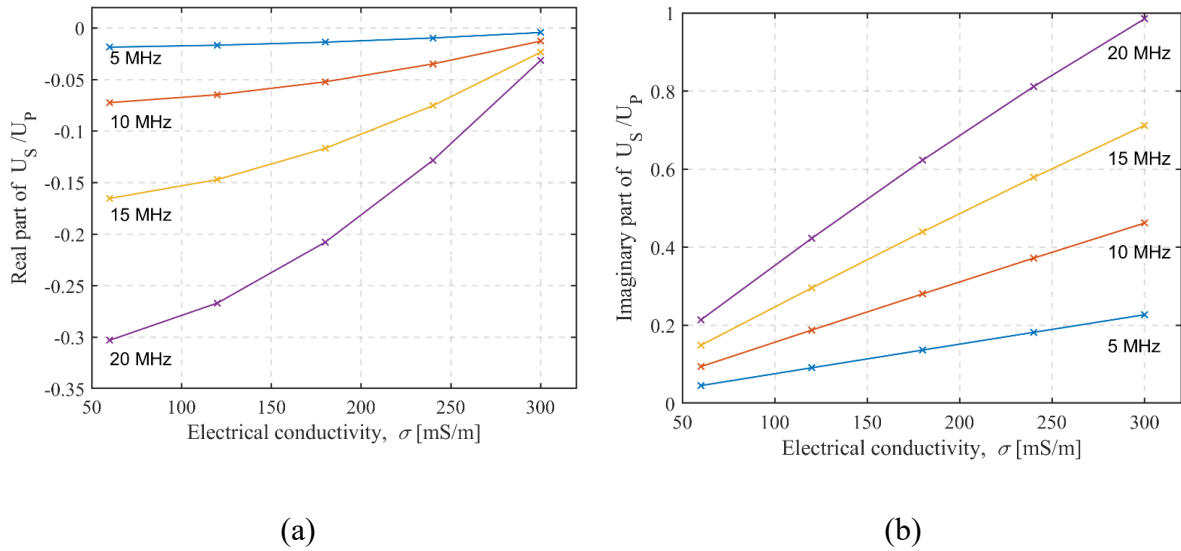
**Figure 53.** FEM conductivity dependence of the (a) real part and (b) imaginary part of $U_S/U_P$ with the frequency as a parameter. Linear interpolation is used between data points.
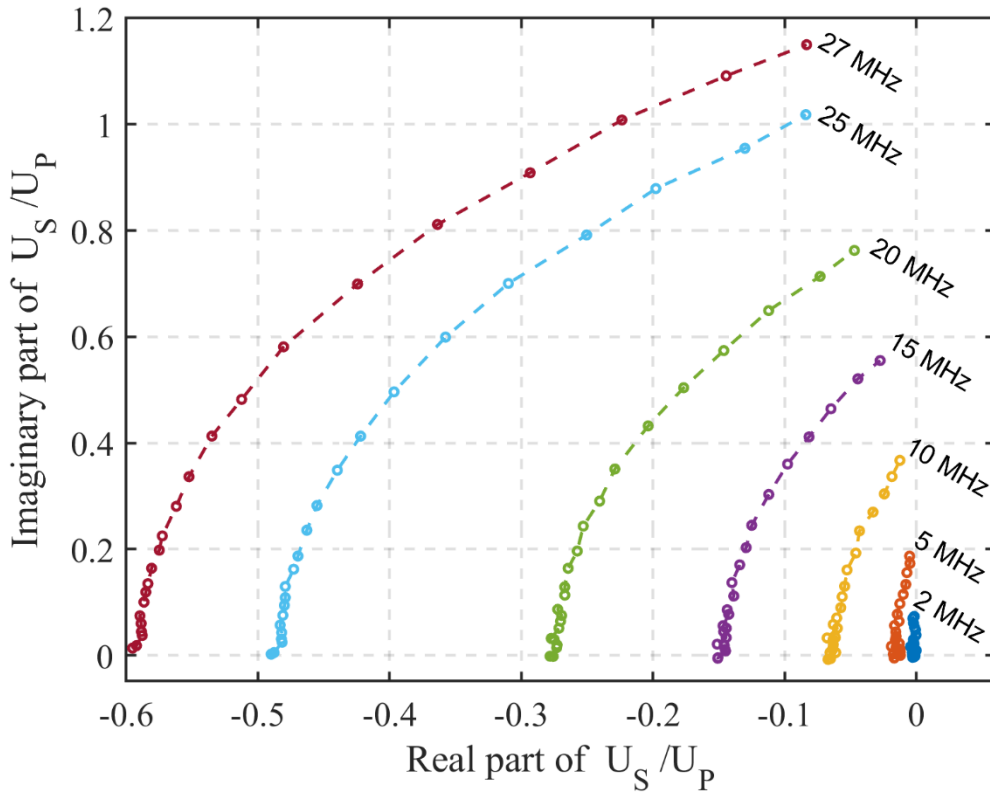


**Figure 54.** Measured electrical conductivity from 0 to 305 mS/m for 2, 5, 10, 15, 20, 25, and 27 MHz: shown in complex plane as $U_S/U_P$.

## 5.1.2 Measurement of dielectric permittivity

The sensor response to dielectric permittivity was analyzed experimentally and by FEM for two laboratory experiment cases depending on the medium in the container. In the first analysis, the container was filled with water, and the permittivity was varied by adding sucrose, making it a homogeneous medium case. In the second analysis, the container was partially filled with deionized water, and this was a double-layer case as the upper part of the container was air, and the lower part was water. The double-layered medium has effective permittivity ranging from 1 to 78 depending on the height of the water layer.

### 5.1.2.1 Homogeneous medium case

The sensor sensitivity to dielectric permittivity was initially assessed in a laboratory setting by measuring its response over deionized water, and the permittivity was varied by adding sucrose to the mixture. The relative permittivity of the sucrose-water solution was calculated using the empirical formula as in [123]:

$$\varepsilon_{r_{sucrose}} = \varepsilon_{r_{water}} - 0.226w - \left[ 6.75 \cdot 10^{-4} - 1.5 \cdot 10^{-5} (t-25) \right] w^2 \\ - \left[ 1.09 \cdot 10^{-5} + 4 \cdot 10^{-8} (t-25) \right] w^3, \tag{135}$$

where $\varepsilon_{sucrose}$ and $\varepsilon_{water}$ are the relative permittivities of the sucrose solution and water, respectively, at the temperature $t$ in degrees Celsius, and $w$ is the weight percentage of sucrose in the mixture.

The experiment commenced with the container filled with 61.5 liters of deionized water, and the sensor response was measured for the water's permittivity (($\varepsilon_{water}$ = 78). In each of the 12 subsequent measurement sets, 5000 g of sucrose was added to the water-sucrose mixture. With water having a density of 1 g/ml and sucrose having a density of 1.59 g/ml, the total volume of the mixture increased to 64.64 litres once the sucrose was dissolved. To maintain a constant volume, 3,146.65 ml of the mixture was removed. Consequently, the effective amount of sucrose in the measured mixture was less than the added amount for each measurement set, as detailed in **Table 11**.

Calculated sucrose weight percentage $w$ and temperature $t$ are given in **Table 12**, which are then used to calculate the relative permittivity of a medium (135). The temperature and the electrical conductivity of the mixture were measured using a handheld conductometer WTW 340i. In all cases, the electrical conductivity was less than 0.002 S / m, below the sensor sensitivity to electrical conductivity. Adding a large amount of sucrose to change the permittivity increases the height of the medium in the container. Because of this, after the

dissolution of newly added sucrose, some volume of the mixture was removed before each measurement step to maintain the height in the container.

**Table 11.** Parameters of the water-sucrose mixture for each measurement step.

| Meas. step | Added sucrose [kg] | Water mass [kg] | Total sucrose mass [kg] | Total mixture mass [kg] | Mass of the measured mixture [kg] | Water mass in the measured mixture [kg] | Sucrose mass in the measured mixture [kg] |
|---|---|---|---|---|---|---|---|
| 1 | 0 | 61.5 | 0 | 61.5 | 61.5 | 61.5 | 0 |
| 2 | 5 | 61.5 | 5 | 66.5 | 63.265 | 58.508 | 4.756 |
| 3 | 5 | 58.508 | 9.756 | 68.265 | 64.944 | 55.662 | 9.282 |
| 4 | 5 | 55.662 | 14.282 | 69.944 | 66.541 | 52.954 | 13.587 |
| 5 | 5 | 52.954 | 18.587 | 71.541 | 68.061 | 50.378 | 17.683 |
| 6 | 5 | 50.378 | 22.683 | 73.061 | 69.507 | 47.927 | 21.579 |
| 7 | 5 | 47.927 | 26.579 | 74.507 | 70.883 | 45.596 | 25.286 |
| 8 | 5 | 45.596 | 30.286 | 75.883 | 72.191 | 43.378 | 28.813 |
| 9 | 5 | 43.378 | 33.813 | 77.191 | 73.436 | 41.268 | 32.168 |
| 10 | 5 | 41.268 | 37.168 | 78.436 | 74.621 | 39.260 | 35.360 |
| 11 | 5 | 39.260 | 40.360 | 79.621 | 75.748 | 37.350 | 38.397 |
| 12 | 5 | 37.350 | 43.397 | 80.748 | 76.820 | 35.533 | 41.286 |
| 13 | 5 | 35.533 | 46.286 | 81.820 | 77.839 | 33.805 | 44.034 |

**Table 12.** Sucrose weight percentage, temperature of the sucrose-water mixture, and calculated permittivity of the medium.

| Measurement | Sucrose weight percentage $w$ [%] | Mixture temperature $t$ [°C] | Calculated relative permittivity $\varepsilon_r$ |
|---|---|---|---|
| 1 | 0% | 26.50 | 78.02 |
| 2 | 8% | 25.80 | 76.54 |
| 3 | 14% | 25.20 | 75.10 |
| 4 | 20% | 24.50 | 73.76 |
| 5 | 26% | 23.80 | 72.48 |
| 6 | 31% | 23.50 | 71.10 |
| 7 | 36% | 24.20 | 69.43 |
| 8 | 40% | 23.60 | 68.26 |
| 9 | 44% | 22.90 | 67.17 |
| 10 | 47% | 22.40 | 66.06 |
| 11 | 51% | 22.80 | 64.79 |
| 12 | 54% | 22.40 | 63.50 |
| 13 | 57% | 24.80 | 62.50 |

The measured sensor response to the permittivity for excitation frequencies 10 MHz, 20 MHz, 25 MHz, and 27 MHz is shown in **Figure 55.** Only the real part of the signal is shown, as the imaginary part is negligible due to the low conductivity of deionized water and the volume of the medium. The same data is shown in **Figure 56** compared to the FEM results for the permittivity range from 1 to 78. It can be seen that the measurement results agree well with

the FEM results both in terms of absolute values and sensitivity to the dielectric permittivity. It can also be inferred that the sensor system at the higher end of the frequency range would be sensitive to lower values of permittivity, which are more typical for soils. Using sucrose to reduce water permittivity is useful for the narrow range of permittivity values because a high mass percentage of the sucrose is needed to decrease the relative permittivity of the homogeneous medium significantly. For example, relative permittivity values below 60 require a sucrose mass percentage higher than 60%.
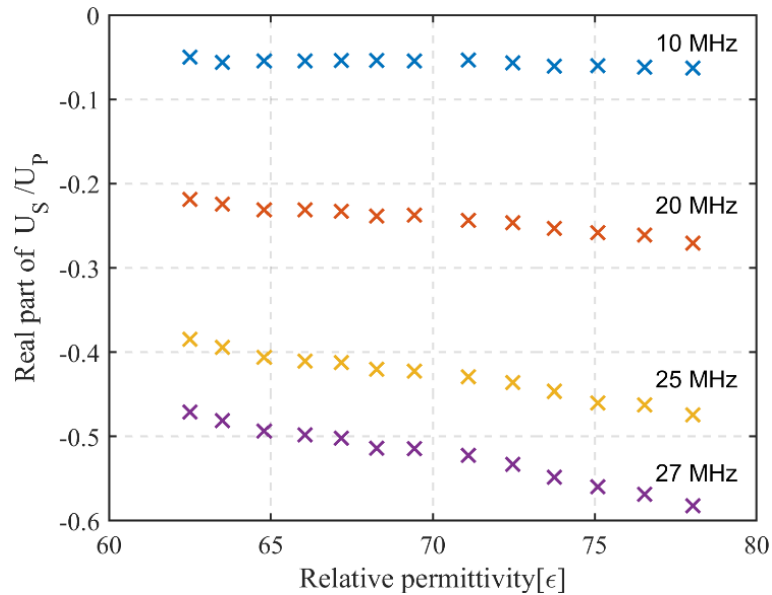


**Figure 55.** Real part of the measured sensor response $U_S/U_P$ for permittivity from 62 to 78, depending on the excitation frequency. The sucrose-water solution permittivity was calculated following [123].
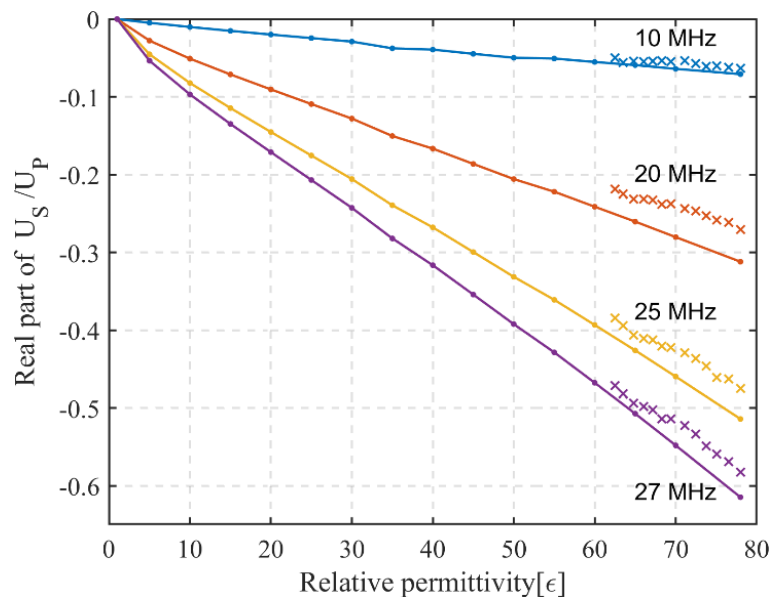


**Figure 56.** Real part of the measured sensor response $U_S/U_P$ for permittivity from 62 to 78 (crosses) depending on the excitation frequency, compared to the FEM results (dotted full lines) for permittivity from 1 to 78.

## 5.1.2.2 Double-layered medium case

In this analysis, the container has two layers: the upper layer is air, and the lower layer is deionized water with a height $h_w$. The height of the lower layer is increased from 0 to the total height of the container $h$. The spatial sensitivity and the inspected volume determine the sensor response. The effective permittivity is 1 for $h_w$=0 cm and 78 for $h_w$=$h$.

The sensor response was measured in the laboratory using deionized water as the second layer, whose height was varied from 2.5 cm to 28.5 cm in 17 steps by adding water to the container. For the first 11 levels of the medium, 5 liters of deionized water was added at each step, which increased the height to 25.3 cm. For the remaining 6 steps, the amount of water was gradually reduced to 0.5 liters per step until the final height of 28.5 cm was obtained. This was done because the sensor sensitivity increases with the height of the second layer. The amount of water per step was measured using a precision weight scale, assuming that 1 liter equals 1 kg of water. The amount of added water, the height of the medium, the temperature, and the conductivity for each step are listed in **Table 13**.

**Table 13.** Amount and properties of deionized water in the double-layered medium experiment.

| Amount of water [L] | Added weight [kg] | Height of the medium $h_w$ [cm] | Temperature T [°C] | Conductivity σ [µS/m] |
|---|---|---|---|---|
| 5 | 5 | 2.6 | 26.2 | 3.3 |
| 10 | 5 | 5 | 25.7 | 3.3 |
| 15 | 5 | 7.5 | 25.7 | 3.3 |
| 20 | 5 | 9.9 | 25.5 | 3.4 |
| 25 | 5 | 12.1 | 25.3 | 3.5 |
| 30 | 5 | 14.5 | 24.9 | 3.8 |
| 35 | 5 | 16.7 | 24.8 | 3.8 |
| 40 | 5 | 18.9 | 25 | 3.8 |
| 45 | 5 | 21 | 24.8 | 3.8 |
| 50 | 5 | 23.2 | 24.8 | 3.8 |
| 55 | 5 | 25.4 | 25.4 | 3.8 |
| 57.5 | 2.5 | 26.4 | 24.4 | 3.8 |
| 60 | 2.5 | 27.5 | 24.5 | 3.8 |
| 61 | 1 | 27.9 | 24.4 | 3.8 |
| 61.5 | 0.5 | 28.1 | 24.4 | 3.8 |
| 62 | 0.5 | 28.3 | 24.5 | 3.9 |
| 62.5 | 0.5 | 28.5 | 24.5 | 3.9 |

In the FEM simulations, the container was divided into 17 layers corresponding to the 17 steps in the experiment. The height of the second layer was increased by switching the material of a layer from air ($\varepsilon_r = 1$, $\mu_r = 1$, $\sigma = 0$ S/m) to deionized water ($\varepsilon_r = 78$, $\mu_r = 1$, $\sigma = 0.3$ mS/m), **Figure 57**.

(a)

(b)

(c)

(d)

(e)

(f)
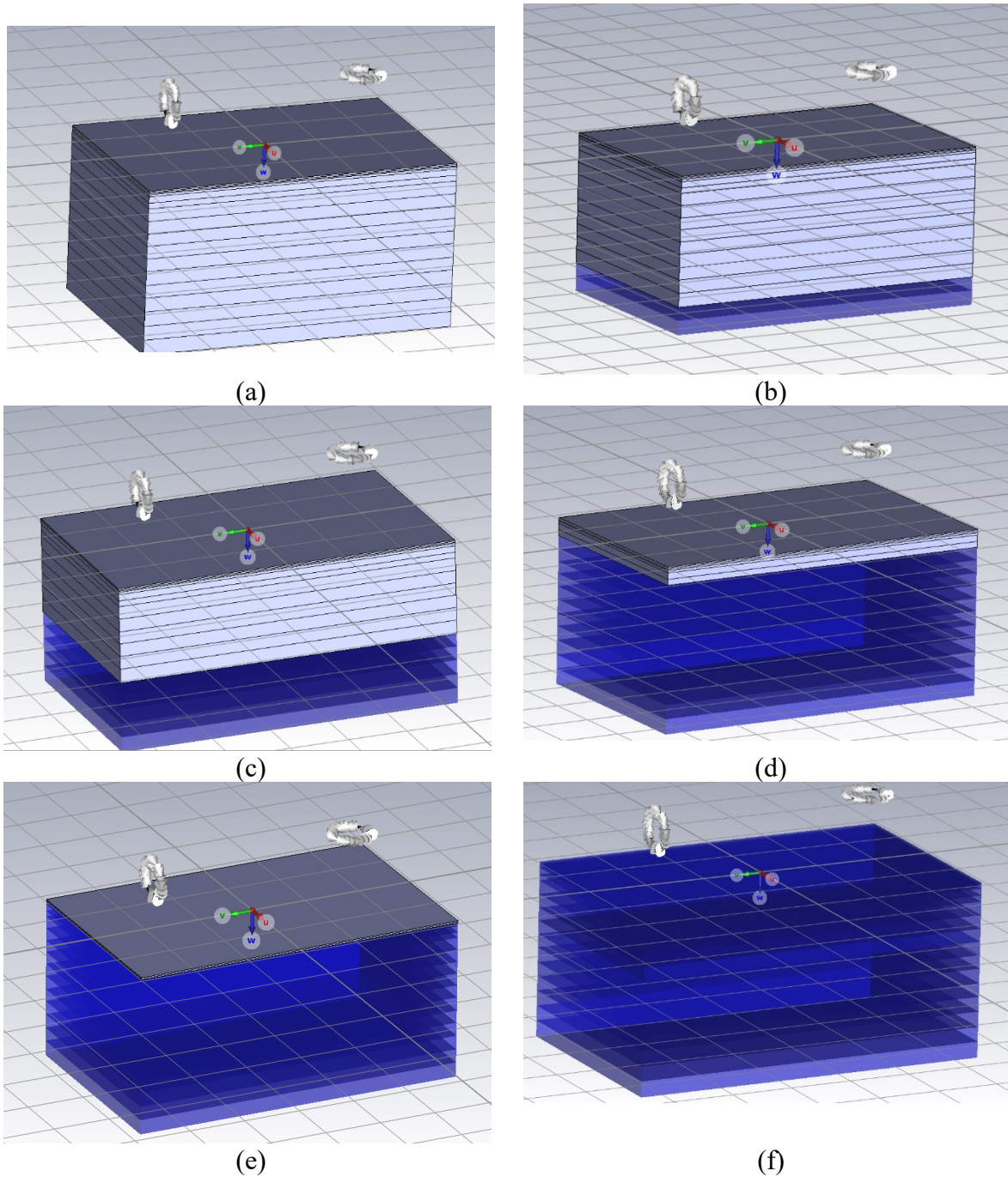
**Figure 57.** FEM geometry for the double-layered medium. In the depicted examples, the lower blue layers of total height $h_w$ are deionized water, and the remaining light blue layers of total height $h-h_w$ are air. The height of the dark blue layers is: (a) 0 cm, (b) 5 cm, (c) 12 cm, (d) 25.3 cm, (e) 28.1 cm, (f) 28.5 cm.

The sensor response was measured in the frequency range from 1 MHz to 30 MHz in 1 MHz steps, and the results are shown as the ratio of secondary to primary magnetic field for both real and imaginary parts of the signal. The real part of the signal Us/Up is shown in **Figure 58** for 8 excitation frequencies (1, 5, 10, 15, 20, 27, and 30 MHz). The measured sensor response (red and blue lines) is compared with the FEM analysis for the equal heights of the medium. The red and blue lines are two sets of experimental runs for the same height of the

medium, done to validate the repeatability of the measurement. Because the electrical conductivity of the second layer is below the sensor threshold, the imaginary part of the signal, shown in **Figure 59**, is negligible, and the sensitivity to the dielectric permittivity is observed in the real part of the signal.



(a) 1 MHz

(b) 10 MHz

(c) 15 MHz

(d) 20 MHz

(e) 27 MHz
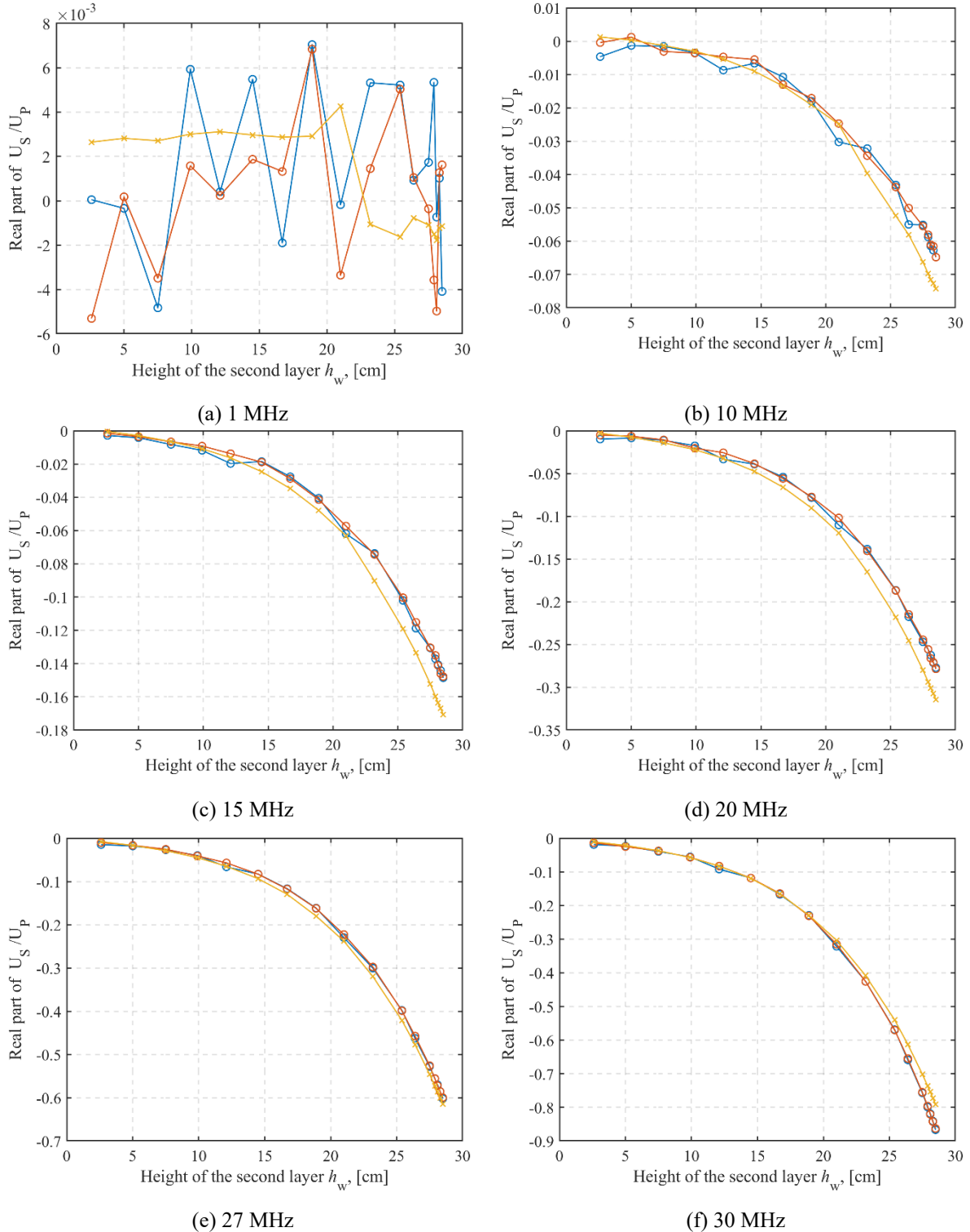
(f) 30 MHz

**Figure 58.** Real part of the sensor measured response $U_S/U_P$ for two experimental runs (red and blue circles) depending on the height of the second layer, compared with FEM analysis (yellow crosses) for excitation frequencies from 1 to 30 MHz, (a)-(f).

(a)

(b)
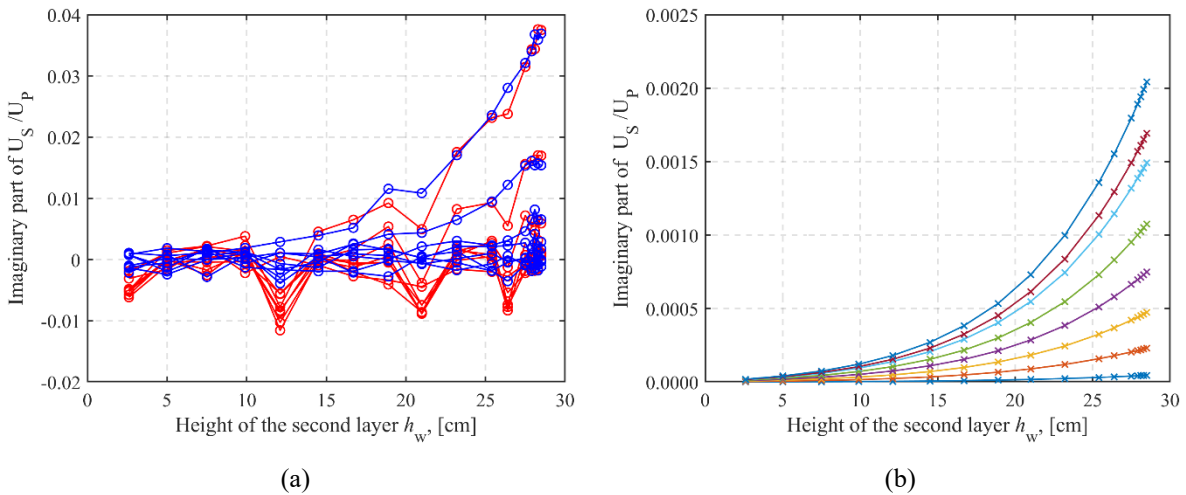
**Figure 59.** Imaginary part of the sensor response $U_S/U_P$ from 1 to 30 MHz: (a) measurement of the first experimental run (blue) and second experimental run (red), (b) FEM results for the same experimental run.

By comparing laboratory measurements and FEM analysis, it is possible to estimate the effective relative permittivity of the double-layered container. The comparison of the laboratory measurements for the higher part of the frequency range of interest is shown in **Figure 60**. The real part of the measured sensor response is shown with circles, and the FEM results with lines for frequencies 15 MHz (blue), 20 MHz (red), 25 MHz (yellow) and 27 MHz (purple). There is a good agreement between the measurements and the FEM results across the frequency range of the interest, opening the possibility of estimating the effective permittivity.
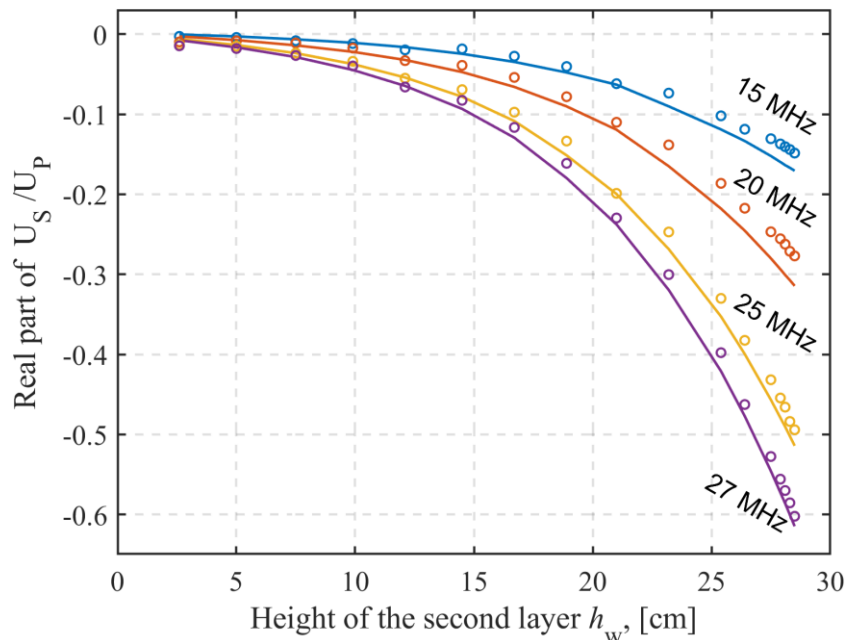


**Figure 60.** The real part of the measured sensor response $U_S/U_P$ for different medium heights (circles) for the higher end of the excitation frequency range of interest, compared to the FEM results (full lines) for medium heights from 2.5 cm to 28.5 cm.

The effective permittivity $\varepsilon_{\text{eff}}$ of the double-layered medium of height $h_{\text{w}}$ is the permittivity of the homogeneous medium that would result in the same real part of $U_{\text{S}}/U_{\text{P}}$ as the double-layered medium. The dependence $\varepsilon_{\text{eff}}(h_{\text{w}})$ was determined using the FEM results for the sensor response above the homogeneous medium with relative permittivity varying from 1 to 78, which was described in the homogeneous case measurement, **Figure 56**, and the FEM results for double-layered medium with the water layer heights of $h_{\text{w}}$, **Figure 60**. The real part of the sensor response above the homogeneous medium with the relative permittivity $\varepsilon_{\text{r}}$ and the maximum height of the medium $h_{\text{w}} = h$ is compared to the real part of the sensor response above the double-layered medium in which the second layer has fixed relative permittivity $\varepsilon_{\text{r}} = 78$, and the height $h_{\text{w}}$ is changed from 2.5 cm to 28.5 cm.

$$\varepsilon_{\text{eff}}\left(h_{\text{w}}\right)=\left\{\varepsilon_{\text{r}} \mid \underbrace{\text{Re}\left[\frac{U_{S}\left(\varepsilon_{\text{r}},h_{\text{w}}=h\right)}{U_{P}}\right]}_{\text{FEM, homogenenous}}=\underbrace{\text{Re}\left[\frac{U_{S}\left(\varepsilon_{\text{r}}=78,h_{\text{w}}\right)}{U_{P}}\right]}_{\text{FEM, double-layered}}\right\} \tag{136}$$

The FEM analysis data for both homogeneous and double-layer cases was interpolated using the spline interpolation to obtain more data points, shown in **Figure 61**, **Figure 62**, **Figure 63**, and **Figure 64**.
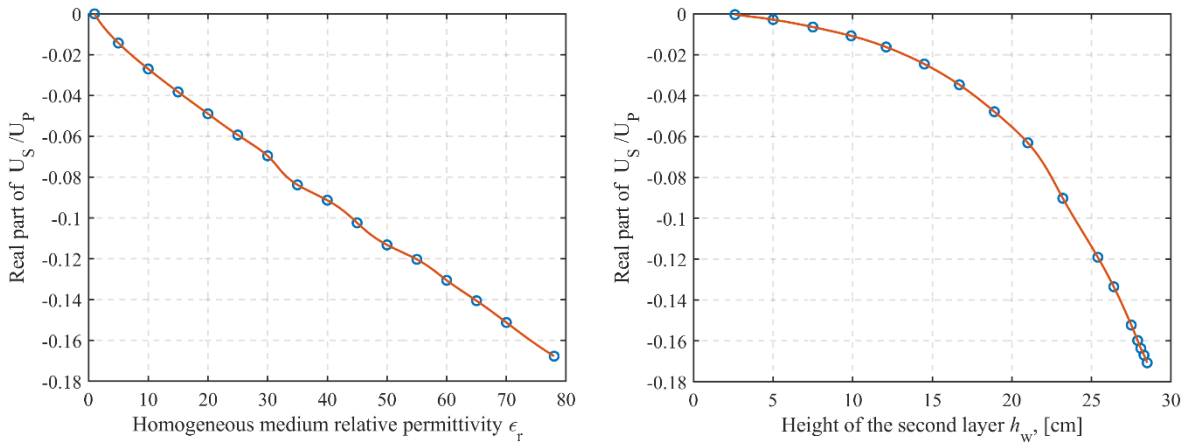


**Figure 61.** Real part of FEM sensor response data for the homogeneous case (left) and double-layered case (right) at 15 MHz. Blue circles are FEM data, and the red line is interpolated data.
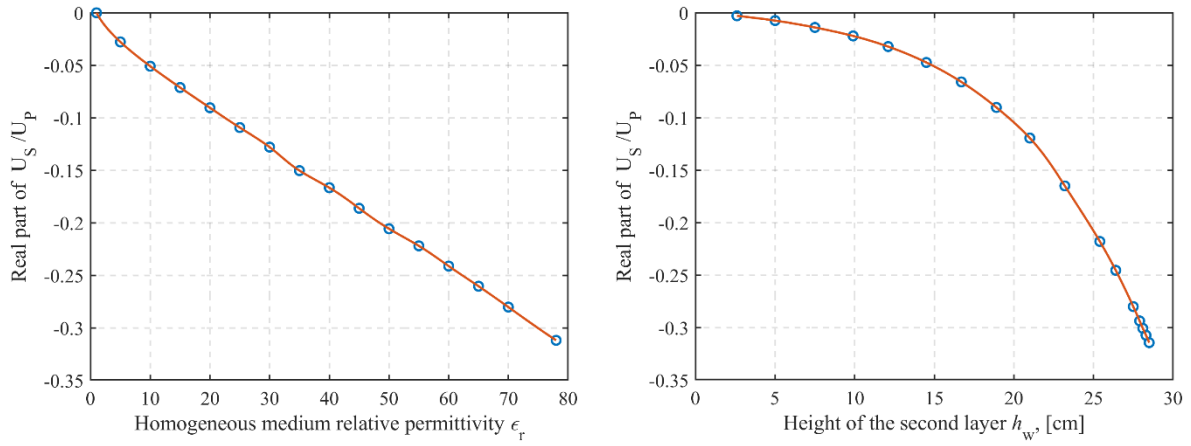
**Figure 62.** Real part of FEM sensor response data for the homogeneous case (left) and double-layered case (right) at 20 MHz. Blue circles are FEM data, and the red line is interpolated data.
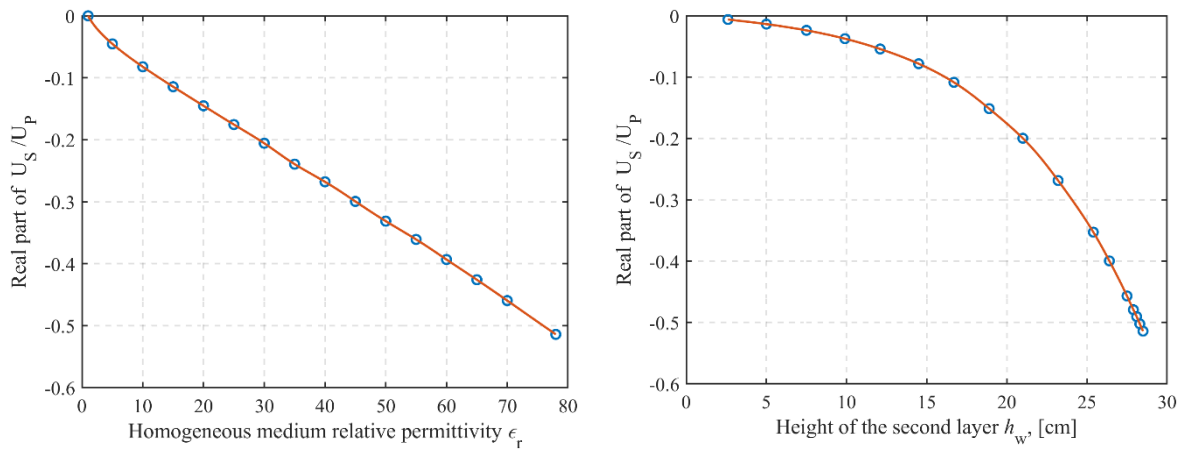


**Figure 63.** Real part of FEM sensor response data for the homogeneous case (left) and double-layered case (right) at 25 MHz. Blue circles are FEM data, and the red line is interpolated data.
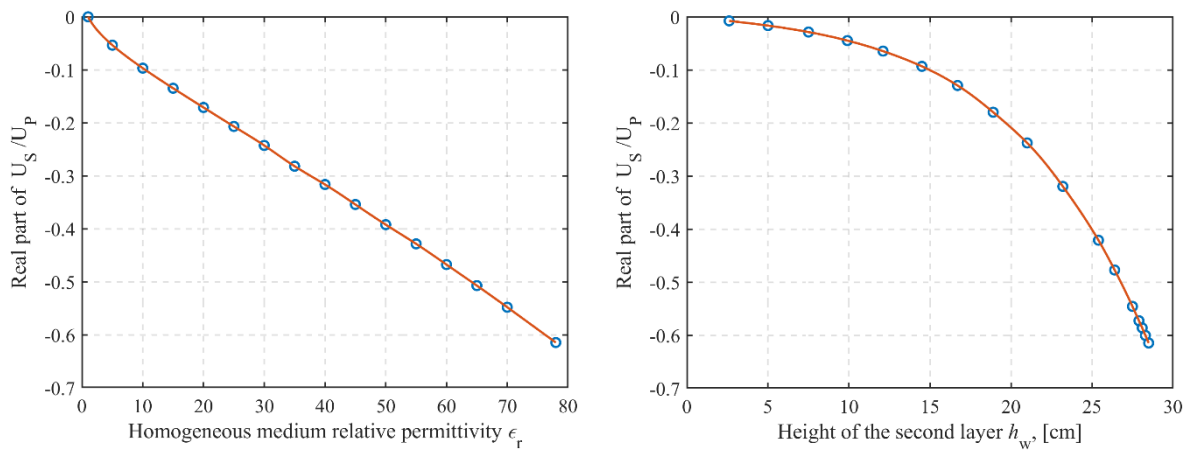


**Figure 64.** Real part of FEM sensor response data for the homogeneous case (left) and double-layered case (right) at 27 MHz. Blue circles are FEM data, and the red line is interpolated data.

The relationship between the effective relative permittivity $\varepsilon_{eff}$ and the second layer height $h_w$ is shown in **Figure 65**. This relationship is independent of the frequency in the analyzed range.
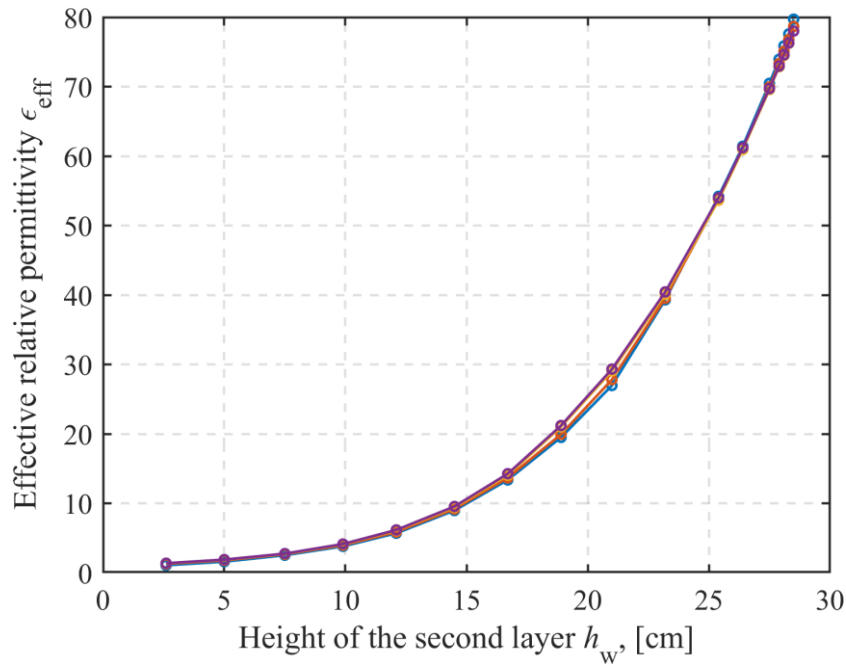


**Figure 65**. FEM analysis of the relationship between medium height and effective relative permittivity for 15 MHz (blue line), 20 MHz (red line), 25 MHz (yellow line) and 27 MHz (purple line).
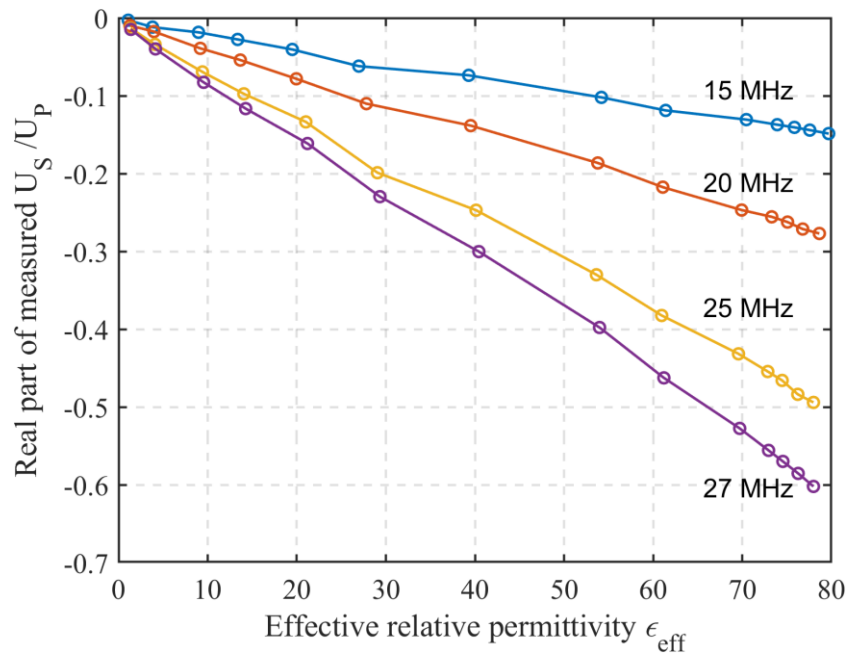


**Figure 66**. The real part of the measured sensor response $U_S/U_P$ for a double-layered medium depending on the effective relative permittivity estimated by FEM.

Because the FEM and measurement results are in good agreement, we can use the relationship from **Figure 65** to pair the measured sensor response at a given water height $h_w$ to

the effective permittivity $\varepsilon_{eff}$ of the corresponding homogeneous medium. The real part of measured $U_S/U_P$, depending on the $\varepsilon_{eff}$ is shown in **Figure 66**. The response is linearly proportional to the $\varepsilon_{eff}$, and the results follow the results of the experiments with the sucrose in **Figure 55**. Furthermore, the changes in the permittivity range of 3–40, typical for soils, are measurable by the proposed sensor system.

## 5.1.3 Simultaneous measurement of conductivity and permittivity

The possibility of simultaneous electrical conductivity and dielectric permittivity measurement was investigated using FEM and laboratory measurements. The FEM analysis results are depicted in a complex plane for multiple excitation frequencies in **Figure 67**, **Figure 68** and **Figure 69**. The conductivity varied from 0.3 mS/m to 300 mS/m, and the permittivity from 1 to 78. Each blue line represents the sensor response for the conductivity range and a constant value of the permittivity. Each red line represents the sensor response for the dielectric permittivity range and a constant value of the electrical conductivity.

The FEM results for the lower part of the frequency range are shown in **Figure 67** for 2 MHz and 5 MHz. For these frequencies, the sensor response is dominantly in the imaginary part of the signal and increases linearly with the electrical conductivity, but the sensitivity is low. The sensor response to the dielectric permittivity is negligible; the real part of the signal is by an order of magnitude lower than the imaginary part, and it is not possible to distinguish different values of medium permittivity as the response is close to the numerical noise floor.



(a)                                                    (b)
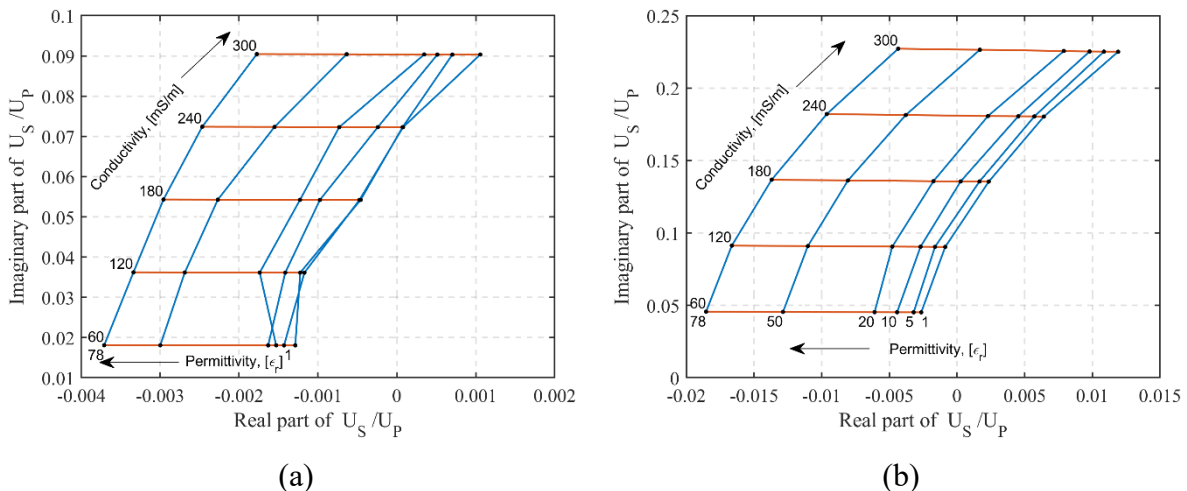
**Figure 67.** FEM results for sensor response $U_S/U_P$ depending on the conductivity and permittivity of the medium shown for the lower range of frequencies: (a) 2 MHz, (b) 5 MHz. Blue lines represent constant permittivity with varied conductivity, and red lines represent constant conductivity with varied permittivity.

The FEM results for the middle part of the frequency range are shown in **Figure 68** for 10 MHz (a) and 15 MHz (b). For these frequencies, the sensitivity to dielectric permittivity is still much lower than the sensitivity to the electrical conductivity. The sensor response is dominantly in the imaginary part of the signal due to the change of electrical conductivity, and the small-induction number approximation is still valid [91].



(a)                                                  (b)
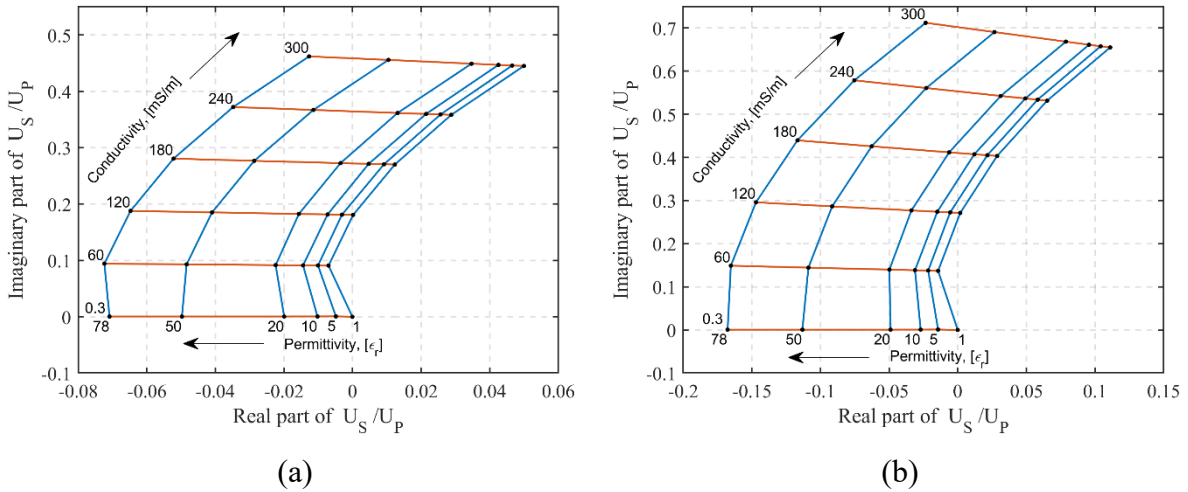
**Figure 68.** FEM results for sensor response $U_S/U_P$ depending on the conductivity and permittivity of the medium, shown for (a) 10 MHz and (b) 15 MHz. Blue lines represent constant permittivity with varied conductivity, and red lines represent constant conductivity with varied permittivity.

The FEM analysis for the upper-frequency range is shown in **Figure 69** for 20 MHz excitation frequency. For low conductivity (below 60 mS/m), the change in the sensor response is dominantly along the imaginary axis of $U_S/U_P$. However, both real and imaginary parts of $U_S/U_P$ are affected for larger electrical conductivities as the low-induction number approximation is no longer valid [91]. The change in the permittivity mainly affects the real part of $U_S/U_P$. The results in **Figure 69** agree with the theoretical analysis of EMI coupling with the medium, e.g., [91], [73]. This separation in the complex plane of the contributions of the electrical conductivity and dielectric permittivity is important as it indicates the possibility of the simultaneous determination of both soil parameters at a single frequency.
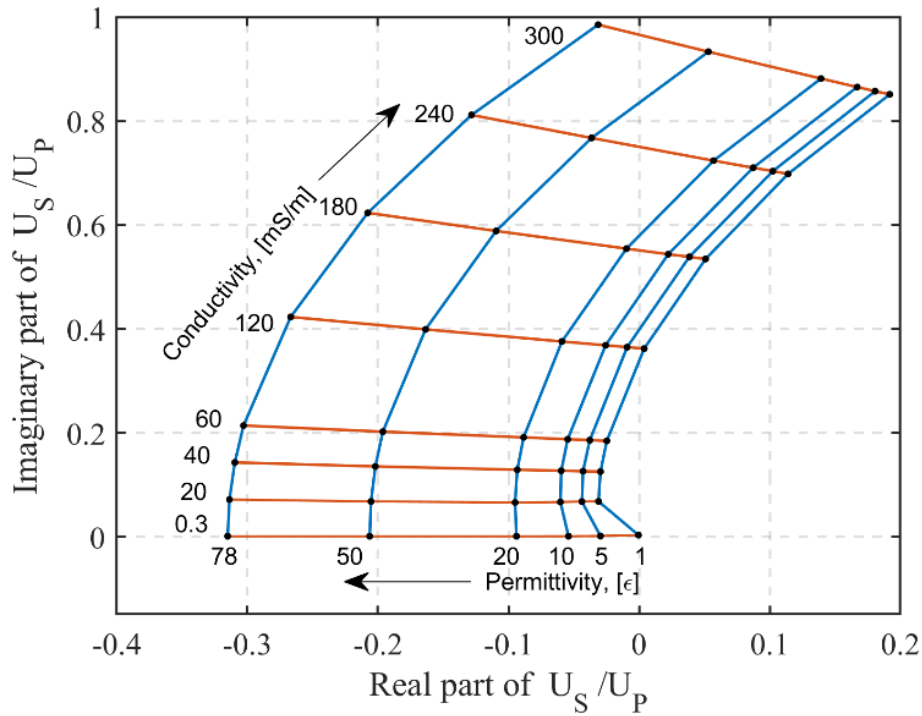
**Figure 69.** FEM results for sensor response $U_S/U_P$ at 20 MHz depending on the conductivity and permittivity of the medium: blue lines represent constant permittivity with varied conductivity, and red lines represent constant conductivity with varied permittivity.

The sensor response was measured in the laboratory for four experimental runs: A–B, A–C, C–D, and E–A. The results for 20 MHz and 27 MHz are shown in **Figure 70** and **Figure 71**, respectively. The values of electrical conductivity and dielectric permittivity of the medium corresponding to measurement data points are shown in **Figure 72**. In the first run (yellow line, A–B), electrical conductivity was varied by adding salt to the deionized water. The sensor response was measured starting from A ($\sigma = 0.3$ mS/m and $\varepsilon_r = 78$) to B ($\sigma = 300$ mS/m, $\varepsilon_r = 78$). In the second run (blue line, A–C), the permittivity was decreased by adding sucrose (5 kg for each of 12 steps) to the deionized water starting from A ($\sigma = 0.3$ mS/m, $\varepsilon_r = 78$) to C ($\sigma = 0.3$ mS/m, $\varepsilon_r = 62$). In the third run (red line, C–D), electrical conductivity was varied by adding salt to the sucrose-water solution starting from point C ($\sigma = 0.3$ mS/m, $\varepsilon_r = 62$) to point D ($\sigma = 300$ mS/m, $\varepsilon_r = 62$). In the fourth run, the sensor response was measured for the double-layered medium, purple line (E–A). The range of permittivity values from 62 to 78 overlaps with the measurement results using the sucrose-water solution, experimental run C–A (blue). The sensor response for the effective permittivity $\varepsilon_{eff}$ of the double-layered medium agrees with the sensor response for the calculated relative permittivity $\varepsilon_r$ of the homogeneous medium. The measurement results for all 4 experimental runs in **Figure 70** agree with the FEM analysis because they follow simulated lines of constant permittivity or conductivity, as in **Figure 69**.
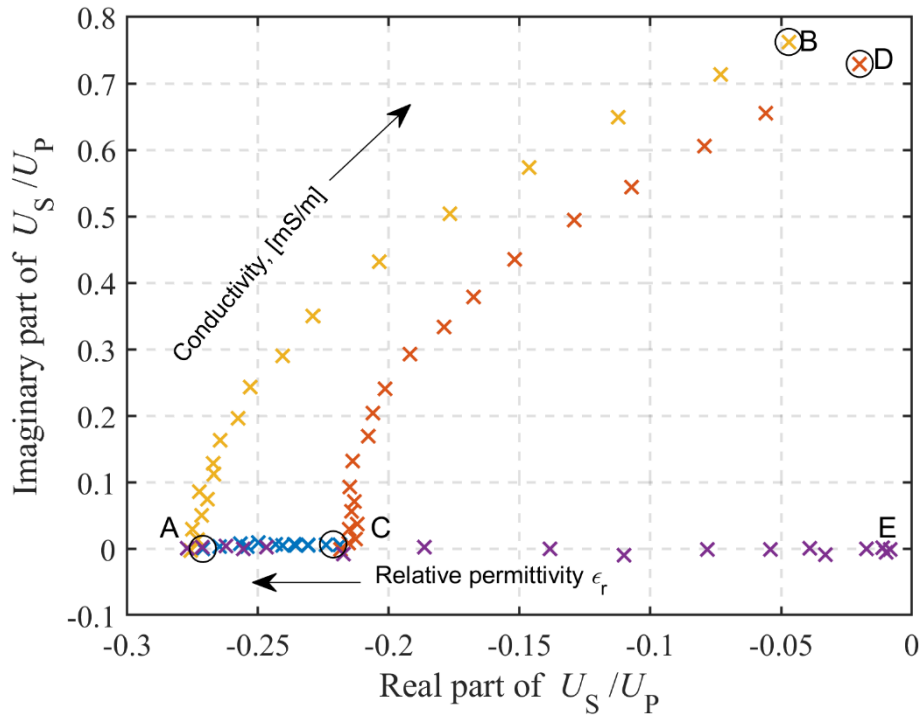
**Figure 70.** Measured $U_S/U_P$ at 20 MHz depending on the conductivity and permittivity of the medium: A ($\sigma = 0.3$ mS/m and $\varepsilon_r = 78$), B ($\sigma = 300$ mS/m, $\varepsilon_r = 78$), C ($\sigma = 0.3$ mS/m, $\varepsilon_r = 62$), D ($\sigma = 300$ mS/m, $\varepsilon_r = 62$). The purple line from E ($\varepsilon_{eff} = 1$) to A ($\varepsilon_{eff} = 78$) is the measurement with the double-layered medium.
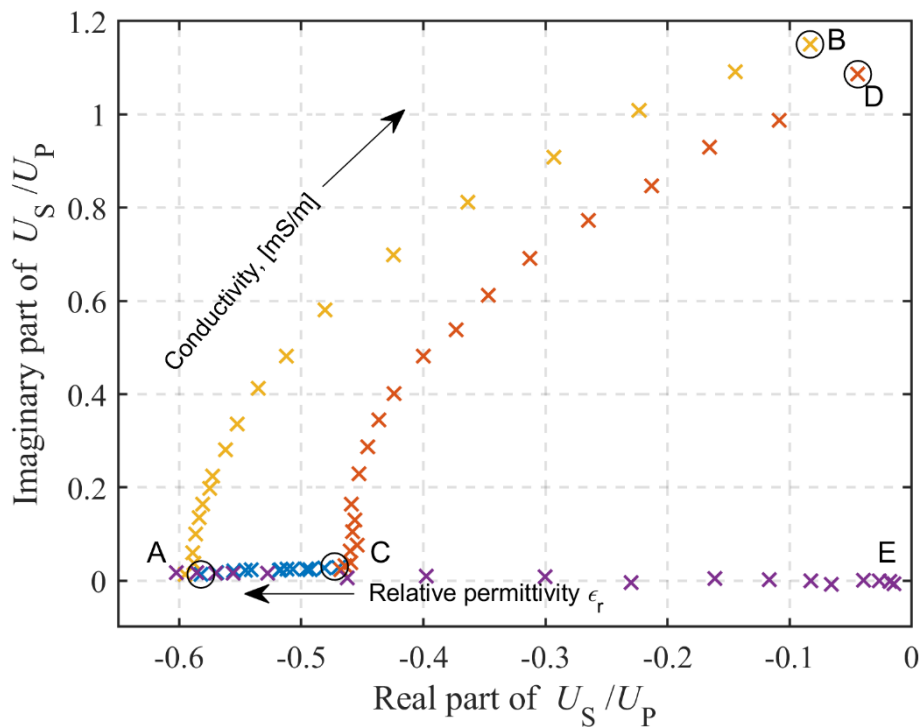


**Figure 71.** Measured $U_S/U_P$ at 27 MHz depending on the conductivity and permittivity of the medium: A ($\sigma = 0.3$ mS/m and $\varepsilon_r = 78$), B ($\sigma = 300$ mS/m, $\varepsilon_r = 78$), C ($\sigma = 0.3$ mS/m, $\varepsilon_r = 62$), D ($\sigma = 300$ mS/m, $\varepsilon_r = 62$). The purple line from E ($\varepsilon_{eff} = 1$) to A ($\varepsilon_{eff} = 78$) is the measurement with the double-layered medium.
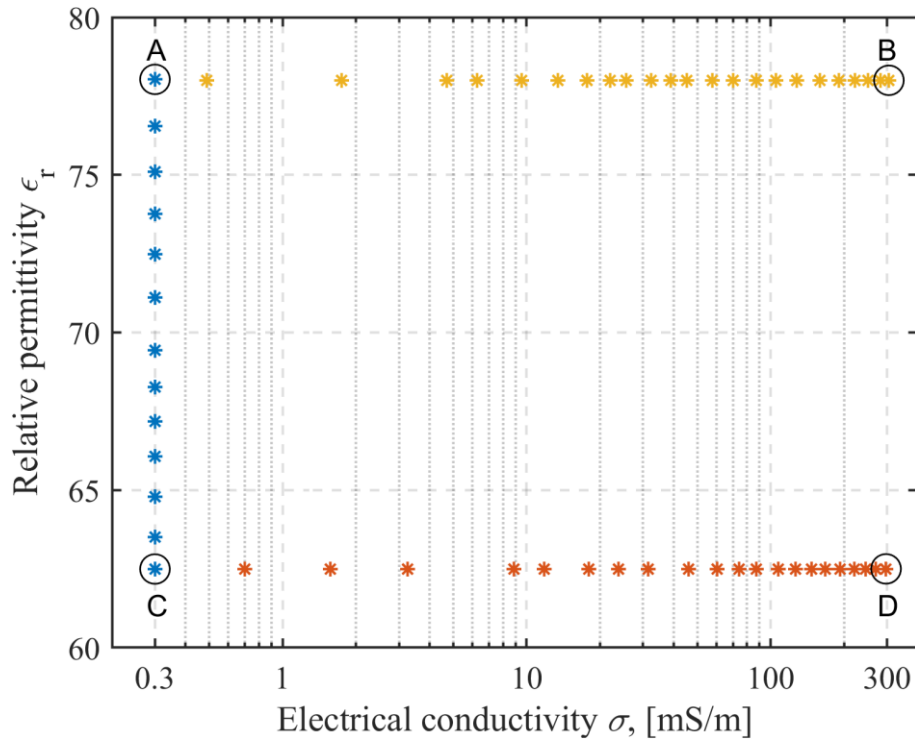
**Figure 72.** Values of electrical conductivity and dielectric permittivity corresponding to each measured data point in **Figure 70** and **Figure 71**.

The measured sensor response for the lower part of the frequency range of interest is shown in **Figure 73** for 2 MHz and 5 MHz. The sensitivity to the electrical conductivity is low, although it is possible to measure different conductivity levels from point A to B and from C to D. However, it is not possible to distinguish different levels of the medium's dielectric permittivity measured in the experimental runs from A to C and from E to A, and there is an overlap between experimental runs regarding the electrical conductivity. The measured sensor response is on the order of the measurement system's noise floor for the real part of the sensor response $U_S/U_P$.

The middle part of the frequency range is shown in **Figure 74**: (a) 10 MHz and (b) 15 MHz. In this frequency range, the sensitivity to electrical conductivity is improved, and in the case of 15 MHz, it is possible to distinguish different permittivity of the medium between experimental runs A-B and C-D. The imaginary part of the $U_S/U_P$ is dominant over the real part, and the sensitivity to the permittivity is still much lower for the range of interest from 1 to 78 than the sensitivity to electrical conductivity from 1 mS/m to 300 mS/m.

(a)

(b)
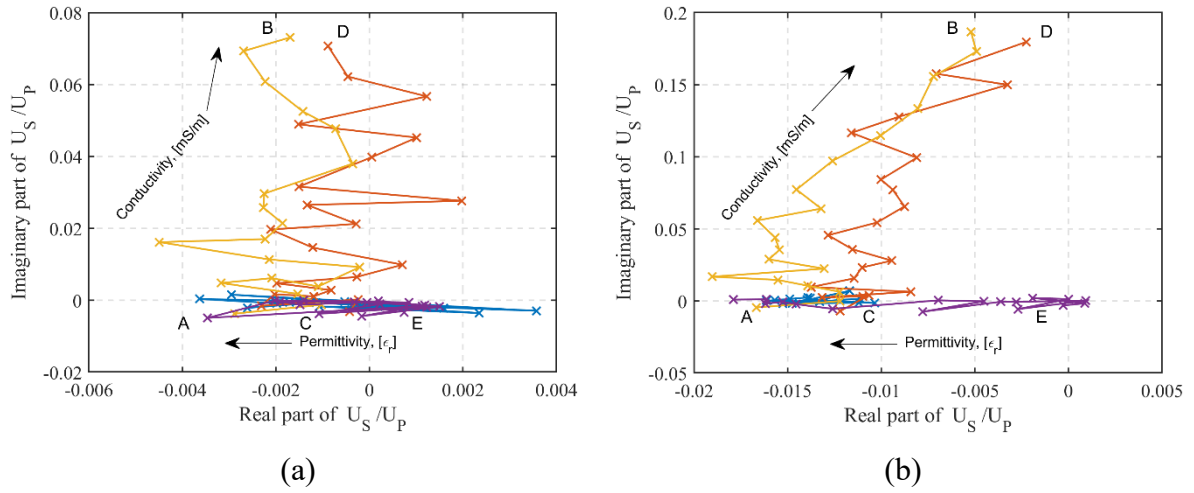
**Figure 73.** Measured $U_S/U_P$ at (a) 2 MHz and (b) 5 MHz, depending on the conductivity and permittivity of the medium: A ($\sigma = 0.3$ mS/m and $\varepsilon_r = 78$), B ($\sigma = 300$ mS/m, $\varepsilon_r = 78$), C ($\sigma = 0.3$ mS/m, $\varepsilon_r = 62$), D ($\sigma = 300$ mS/m, $\varepsilon_r = 62$). The purple line from E ($\varepsilon_{eff} = 1$) to A ($\varepsilon_{eff} = 78$) is the measurement with the double-layered medium.



(a)

(b)
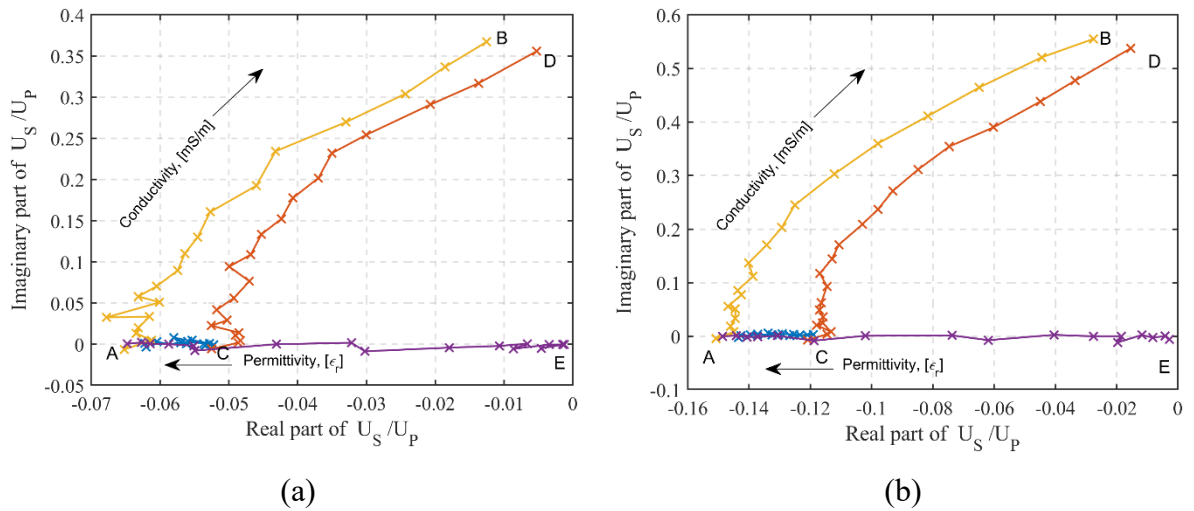
**Figure 74.** Measured $U_S/U_P$ at (a) 10 MHz and (b) 15 MHz, depending on the conductivity and permittivity of the medium: A ($\sigma = 0.3$ mS/m and $\varepsilon_r = 78$), B ($\sigma = 300$ mS/m, $\varepsilon_r = 78$), C ($\sigma = 0.3$ mS/m, $\varepsilon_r = 62$), D ($\sigma = 300$ mS/m, $\varepsilon_r = 62$). The purple line from E ($\varepsilon_{eff} = 1$) to A ($\varepsilon_{eff} = 78$) is the measurement with the double-layered medium.

## 5.2 Field trial

The HFEMI soil sensor was tested in a field trial to analyze the response in a more realistic setting. The field trial was done on the 14th and 18th of October, 2022, in Ludbreg, Croatia, with the laboratory sensor prototype.

The sensor was stationary and placed on two soil patches with similar properties, each with an area of approximately 0.5 m$^2$. The sensor response in the air was measured while the sensor was placed on the wooden stand, approximately 1.5 m above the ground, **Figure 75**. For the measurement of the soil, the sensor was placed directly above the ground, and the distance from the transmitter to the ground was approximately 5 cm, Figure 76.
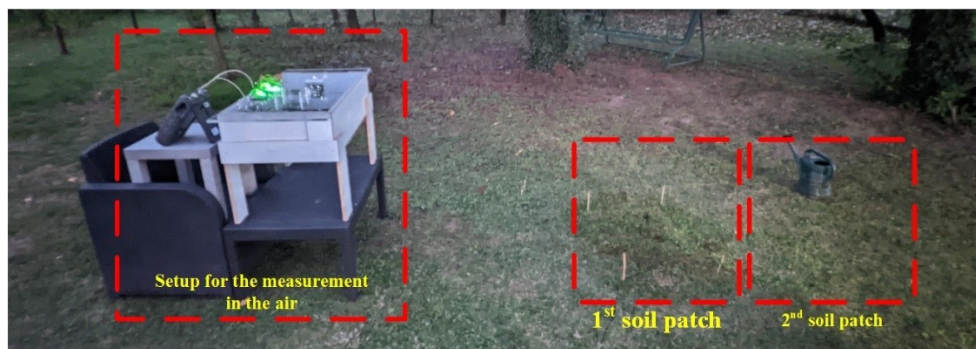


**Figure 75.** Measurement setup for showing the sensor position when measuring response in the air and the position of the first and second measured soil patches.

The first soil patch was irrigated with deionized water in 2.5-liter or 5-liter increments, and the sensor response in both air and above ground was measured after each increment in order to mitigate the temperature effects and possible signal drift. The second soil patch was irrigated with saline water in 2.5-liter increments, with an electrical conductivity of 300 mS/m, following the same measurement procedure.
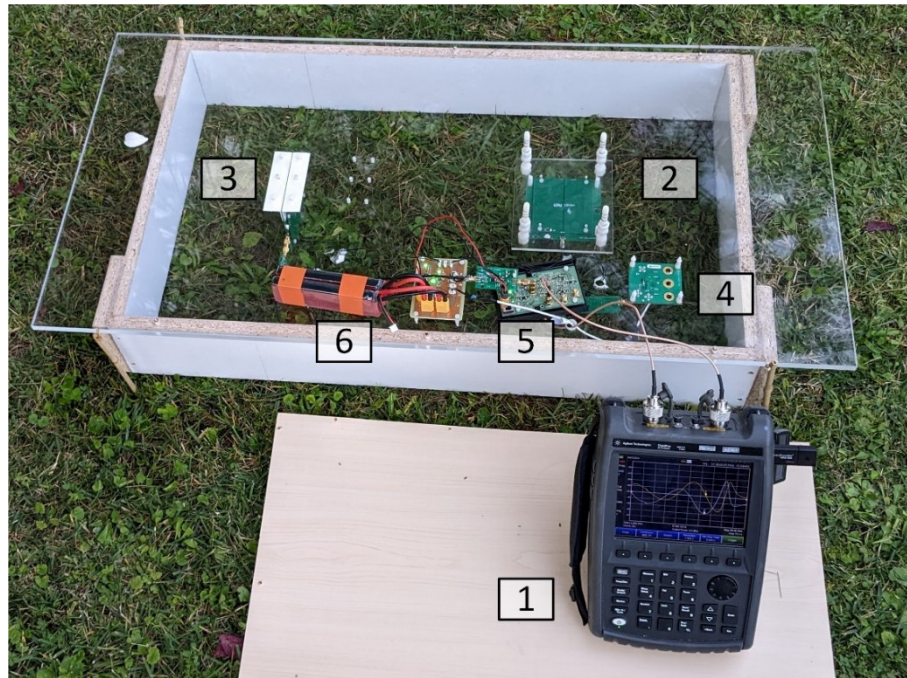
**Figure 76.** Field experimental setup: (1) Network analyzer Keysight Fieldfox N9913A, (2) Shielded transmitter, (3) Shielded receiver, (4) TX amplifier and filter, (5) RX amplifier and filter, (6) Battery power supply.

The field experiment results are shown as the real part of sensor response $U_S/U_P$ in **Figure 77** and the imaginary part in Figure 78 at 10 MHz, 20 MHz, and 27 MHz, depending on the added volume of water. The blue lines represent the first experiment with deionized water, whereas the red lines represent the second experiment with saline water. Adding water increases the soil permittivity, which increases the magnitude of the real part of $U_S/U_P$ at 20 MHz and 27 MHz, **Figure 77**. However, the sensitivity of the real part of $U_S/U_P$ in **Figure 77** to the water volume is lower for the saline water (red) than for the deionized water (blue). This effect is visible in the FEM analysis in Figure 69 as well. The change in the real part is less pronounced beyond 12.5 L of added water, presumably because of the top soil layer saturation. The magnitude of the imaginary part of $U_S/U_P$ in Figure 78 increases with the addition of saline water as it increases the soil's electrical conductivity (red). A significantly less pronounced increase of the imaginary part when adding the deionized water in Figure 78 (blue) is due to the mineral dissolution in the soil.
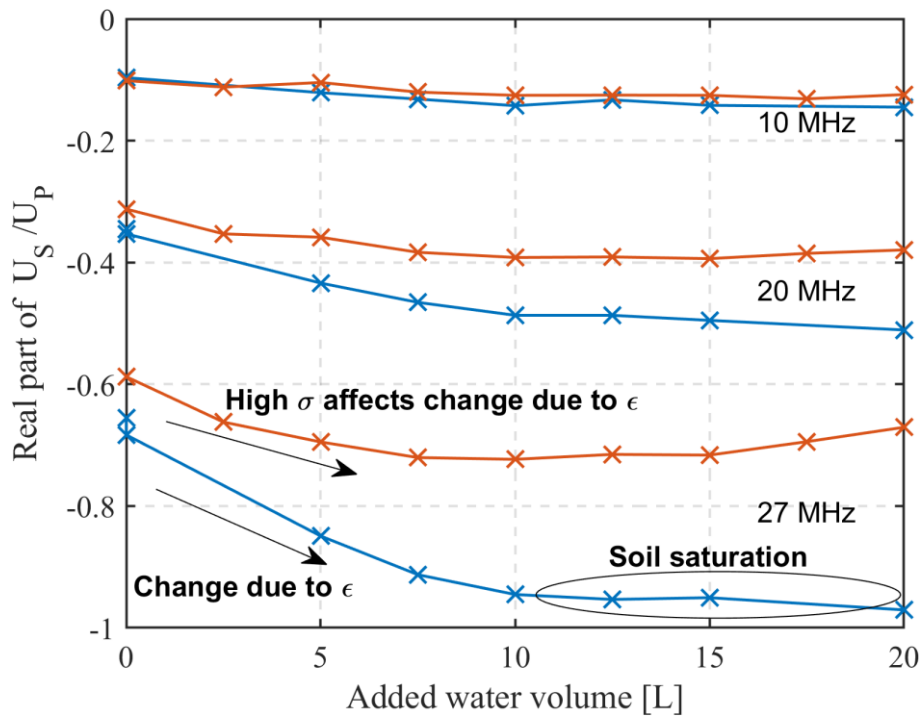
**Figure 77.** Real part of the measured sensor response $U_S/U_P$ in the field experiment at 10 MHz, 20 MHz, and 27 MHz. Soil irrigated with deionized water (blue lines) and saline water with a conductivity of 300 mS/m (red lines).
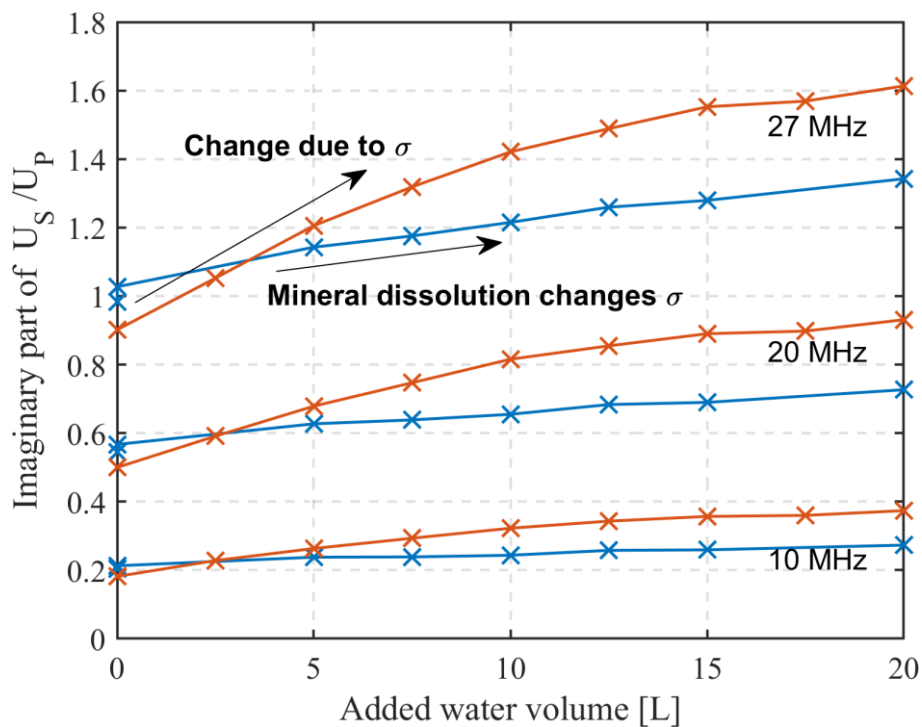


Figure 78. Imaginary part of the measured sensor response $U_S/U_P$ in the field experiment at 10 MHz, 20 MHz, and 27 MHz. Soil irrigated with deionized water (blue lines) and saline water with a conductivity of 300 mS/m (red lines).

# Chapter 6

# Conclusions

## 6.1 Main findings

In precision agriculture, efficient and sustainable soil management relies on mapping the within-field variability of crop conditions and soil properties. The physical and chemical properties of the soil, such as water content or salinity, are connected to the soil electromagnetic parameters of soil (electrical conductivity, magnetic susceptibility, and dielectric permittivity), and there are empirical and theoretical models that relate soil properties to electromagnetic parameters.

Proximal soil sensing (PSS) techniques have a high temporal and spatial resolution of soil data and are better suited than remote sensing for mapping within-field variability. However, the sensors used for PSS have to be adequate for the handheld or towed operation to map larger areas, and they need to have a volume of sensitivity larger than soil heterogeneities to capture information about soil conditions. Electromagnetic PSS modalities that satisfy those conditions are direct current resistivity (DCR) measurement, capacitively coupled resistivity (CCR) measurement, ground-penetrating radar (GPR), and electromagnetic induction (EMI) measurement. They are sensitive to the different electromagnetic parameters because they operate across different frequency ranges, but all modalities provide averages over a volume of spatially dependent sensitivity.

DCR measurements encounter challenges in obtaining reliable data in dry, dense, or stony soil due to the need for good mechanical contact. CCR measurements are contactless and utilize similar inversion algorithms. Both modalities are sensitive only to electrical conductivity. GPR

operates in the ultra-high frequency range and provides information on soil's dielectric permittivity and electrical conductivity. This modality has constrained effectiveness in areas with relatively high electrical conductivity and requires well-identifiable reflections in the soil.

Low-frequency EMI soil sensing is a well-established method in precision agriculture. The sensors operate in the audio frequency range and are sensitive to magnetic susceptibility and electrical conductivity. They are usually used to obtain maps of soil trends, as their absolute response depends on sensor geometry. The provided information complements GPR because, combined, it covers different electromagnetic parameters over a wide frequency range.

High-frequency EMI sensors operate in the high-frequency range (between 3 MHz and 30 MHz, and exhibit higher sensitivity to electrical conductivity, and the sensitivity to dielectric permittivity becomes significant, positioning this modality between the low-frequency EMI and GPR. This thesis presents the model-based method for measuring electrical conductivity and dielectric permittivity using the HFEMI soil sensor, including sensor geometry and electronic instrumentation of the proposed HFEMI sensor, and the analysis of unwanted electromagnetic coupling and interference rejection techniques.

The analytical model of the sensor above the conductive half-layer was derived from the Maxwell equations. In contrast to the low-induction number approximation in LFEMI, the full-wave approach was used, assuming that the electrical field has only an irrotational part. The characteristic dimensions of the problem are still much smaller than the wavelength of the excitation frequency, there is no charge accumulation in the source, and the propagation can be considered instantaneous. It is shown that the sensitivity to electrical conductivity increases linearly with the frequency, quadratically for dielectric permittivity, while the sensitivity to magnetic susceptibility is frequency-independent. The sensor model above the half-layer can be used to calibrate the proposed HFEMI soil sensor.

The proposed HFEMI soil consists of a mutually perpendicular transmitter and receiver coil to reduce direct inductive coupling between the coils. The coil centers are slightly offset to control the magnitude of the primary coupling in order to obtain a stable phase angle when interpreting the measurements. The coils were made on PCB with a few turns and patterned PCB electrostatic shields to reduce capacitive coupling between the coils and the medium. The total capacitance of the transmitter and receiver was kept low enough to obtain a coil resonant frequency above 30 MHz. The electronic design involves battery-powered proprietary analog front-end circuitry and a commercial vector network analyzer. The laboratory measurement setup included a wooden stand and a plastic container filled with a medium to emulate soil properties. The sensor response was interpreted as the ratio of secondary-to-primary induced

voltage to allow comparison with numerical models. A measurement protocol was derived in which the sensor response was first measured in the air to obtain the primary coupling and then above the medium.

The method to evaluate the effectiveness of electrostatic shielding for the proposed HFEMI soil sensor geometry was presented. The sensor transfer function was measured in the air from 1 MHz to 20 MHz for the cases when the magnetic moment of the transmitter points up or down. The derived equivalent circuit model can approximate the measured transfer function and estimate the inductive and capacitive coupling. This can be used to evaluate the effectiveness of the shielding. The method was illustrated on 36 different shielding configurations, and the results are aligned with the shielding practices, showing that the lowest capacitance was achieved by reducing the spacing between coil and shields and, to a lesser degree, by choosing the appropriate shield pattern. The comparison with the FEM model for the sensor response above the conductive medium corroborated that the shielded coils with the lowest capacitance have the best agreement with the FEM results.

The sensor liftoff can be a significant source of errors in soil mapping applications. The variations in the liftoff can become prominent when using the EMI sensors mounted on a vehicle or as a handheld device on uneven terrain. The influence of the liftoff on the proposed HFEMI sensor was evaluated in the laboratory by raising the sensor above the conductive medium and with the analytical model. The sensitivity to electrical conductivity decreases non-linearly with the increase in height. Perpendicular coil configuration behaves similarly to the vertically oriented coil configuration. The measurement results show that the sensitivity to liftoff is frequency-independent under the medium's constant dielectric permittivity and electrical conductivity. It is possible to simultaneously determine liftoff and electrical conductivity or dielectric permittivity from the measurement at a single frequency. The interpretation of the measurements is not unambiguous when electrical conductivity, dielectric permittivity, and liftoff change simultaneously. The results of the analytical model and laboratory measurements show that the liftoff depends on geometry and distance from the medium. This means that for simultaneous measurement of both electrical conductivity and dielectric permittivity in field conditions, techniques of measuring liftoff or using multiple excitation frequencies should be explored.

The temperature influence on EMI soil sensors presents a challenge in field mapping applications. From the literature overview about the influence of temperature on commercially available sensors such as Geonics EM-38, the main highlighted issues are fluctuation in ambient temperature, device temperature, and topsoil layer temperature, which changes electrical

conductivity. The changes in sensor response can manifest as slow drift during the day or as fast changes due to temperature spikes, such as exposing the sensor to direct sunlight. The effects can be mitigated by implementing temperature sensors near electronics and measuring ambient temperature to compensate for the drift. Good practices for EMI soil sensors in field surveys are turning on the sensor and leaving it to reach working temperature, using the enclosure that isolates the electronics from outside effects, and avoiding measurements on hot days and under direct sunlight. The temperature effects in low-frequency EMI soil sensors translate to HFEMI soil sensors, so the literature overview provides valuable insight for sensor design.

The temperature influence on the proposed HFEMI soil sensor was evaluated experimentally in the laboratory and the field by measuring primary coupling over an extended period. The ambient temperature was kept relatively constant in the laboratory experiment over the 13h measurement period. The measured primary coupling $H_P$ change was around 1 % across the whole frequency range and exhibited minimal drift in a controlled environment. The field experiments showed that temperature fluctuations and direct sunlight exposure could cause notable drift of $H_P$. For the geometry used, the primary coupling decreases with the increase in temperature. These findings suggest that temperature compensation mechanisms and calibration procedures are necessary for field application use.

The mechanical misalignment effects on the proposed HFEMI sensor were investigated by FEM analysis by varying the intercoil separation, coil height, and tilt angles of transmitter and receiver coils separately. The primary coupling in the air was evaluated, and the sensor response above the conductive medium. For small changes in height, separation, and angles, the secondary coupling through the medium is not affected due to the sensor's characteristic dimension, which is much larger than mechanical variations. On the other hand, the primary coupling is notably influenced by these misalignments, showing a linear change in height and distance. The change of transmitter pitch angle affects the primary coupling the most because the coupling is minimal for the perpendicular coil geometry, so the angle change increases primary coupling. This affects the interpretation of sensor results because the ratio of secondary-to-primary coupling $U_S/U_P$ is used. These effects can be mitigated by designing the sensor for field use in which the construction is rigid, the coils are fixed in place, and the sensor is often calibrated to track any changes in primary coupling.

The HFEMI soil sensor was analyzed quantitatively in the laboratory, with FEM, and qualitatively in the field experiments. In the laboratory experiments, sensor response to dielectric permittivity was evaluated using two approaches. In the first approach, sucrose was

added to deionized water, which reduced permittivity from 78 to 62, making this homogeneous medium case. In the second approach, the water level in the container varied, effectively lowering the permittivity as the upper layer was air and lower water, making it a double-layered medium case. The conductivity was varied by adding salt to deionized water and to sucrose-water solution. The experiments showed good sensitivity for the range of electrical conductivity and dielectric permittivity typical for most soil types (10 mS/m – 300 mS/m and 3 – 40, respectively) in the high-frequency range (15 MHz-30 MHz). The results agree well with the results of the FEM model. The results demonstrate that each pair of electrical conductivity and dielectric permittivity can be determined from the in-phase and quadrature signal measurement at one frequency. The field trials were done to test the sensor in a more realistic setting, and the measurement results are aligned with the laboratory findings in that the measured trends in soil when irrigating with water or saline water follow the theoretical analysis.

The frequency range of high-frequency EMI soil sensing is positioned between low-frequency EMI and GPR soil sensing, and it can provide complementary information to other modalities about soil. The HFEMI soil sensor proposed and analyzed in this thesis is sensitive to electrical conductivity and dielectric permittivity in a range typical for soils. It was shown that the high-frequency EMI soil sensor is feasible, but care must be taken to control the sensor liftoff, temperature influence, mechanical misalignment, and unwanted electromagnetic coupling. The laboratory results, the FEM model, and the analytical model show that simultaneous measurement of the electrical conductivity and dielectric permittivity is possible, and it requires sensor calibration.

## 6.2 Limitations and future work

The conducted research can be extended, and several areas have the potential to be further explored. The existing limitations of the proposed high-frequency electromagnetic induction soil sensor will be addressed in future work. These can be grouped into improvements regarding electronic instrumentation, sensor design, and sensor validation in the field conditions.

From the sensor design perspective, a new generation of the proposed sensor prototype can be developed, which includes the design of excitation circuitry, signal amplification, data acquisition, and temperature compensation. Sensor geometry, including coil dimensions, shielding patterns, and coil separation, can be optimized.

The sensor liftoff affects the measurement, and the liftoff compensation should be implemented either by multi-frequency excitation or by using another modality to measure the distance of the sensor from the ground.

A field-ready prototype combined with analytical model calibration would allow further evaluation of the proposed high-frequency electromagnetic induction soil sensor and comparison with other modalities such as direct resistivity, low-frequency electromagnetic induction sensors, or ground-penetrating radar. Further sensor development opens the possibility of advanced data processing procedures and a multidisciplinary approach, as the proposed sensor could become a tool for geoscience and agricultural research.

## 6.3 Final words

Measuring and mapping soil properties gives valuable information about the soil conditions, enabling the optimization of resources in the context of precision agriculture applications. The findings presented in this thesis are promising and encourage further research of high-frequency electromagnetic modality, either in the context of soil sensing or other applications.

# Bibliography

[1]    E. G. Youngs and D. Hillel, *Fundamentals of Soil Physics.*, vol. 19, no. 1. Wiley, 1982. doi: 10.2307/2403016.

[2]    J. W. Doran and M. R. Zeiss, "Soil health and sustainability: managing the biotic component of soil quality," *Applied Soil Ecology*, vol. 15, no. 1, pp. 3–11, Aug. 2000, doi: 10.1016/S0929-1393(00)00067-6.

[3]    R. A. Viscarra Rossel and J. Bouma, "Soil sensing: A new paradigm for agriculture," *Agricultural Systems*, vol. 148, pp. 71–74, Oct. 2016, doi: 10.1016/J.AGSY.2016.07.001.

[4]    D. V. Fitterman and V. F. Labson, "10. Electromagnetic Induction Methods for Environmental Problems," *Near-Surface Geophysics*, pp. 301–356, Jan. 2005, doi: 10.1190/1.9781560801719.ch10.

[5]    C. Bruschini, "A Multidisciplinary Analysis of Frequency Domain Metal Detectors for Humanitarian Demining The Current Situation in Humanitarian Demining," Vrije Universiteit Brussel, Belgium, 2002.

[6]    J. D. D. McNeill, "Archaeological Mapping Using the Geonics EM38B to Map Terrain Magnetic Susceptibility (With Selected Case Histories)," *Geonics Limited Technical Note TN-35*, 2012. http://www.geonics.com/html/technicalnotes.html (accessed Jan. 25, 2022).

[7]    J. A. Doolittle and E. C. Brevik, "The use of electromagnetic induction techniques in soils studies," *Geoderma*, vol. 223–225, no. 1, pp. 33–45, Jul. 2014, doi: 10.1016/j.geoderma.2014.01.027.

[8]    R. Viscarra Rossel and V. Adamchuk, "Proximal soil sensing," 2013, pp. 99–118. doi:

10.13140/2.1.2799.1847.

[9] Y. Xu, S. E. Smith, S. Grunwald, A. Abd-Elrahman, and S. P. Wani, "Evaluating the effect of remote sensing image spatial resolution on soil exchangeable potassium prediction models in smallholder farm settings," *Journal of environmental management*, vol. 200, pp. 423–433, Sep. 2017, doi: 10.1016/J.JENVMAN.2017.06.017.

[10] M. I. Abdulraheem, W. Zhang, S. Li, A. J. Moshayedi, A. A. Farooque, and J. Hu, "Advancement of Remote Sensing for Soil Measurements and Applications: A Comprehensive Review," *Sustainability 2023, Vol. 15, Page 15444*, vol. 15, no. 21, p. 15444, Oct. 2023, doi: 10.3390/SU152115444.

[11] V. L. Mulder, S. de Bruin, M. E. Schaepman, and T. R. Mayr, "The use of remote sensing in soil and terrain mapping — A review," *Geoderma*, vol. 162, no. 1–2, pp. 1–19, Apr. 2011, doi: 10.1016/J.GEODERMA.2010.12.018.

[12] B. Lu, P. D. Dao, J. Liu, Y. He, and J. Shang, "Recent advances of hyperspectral imaging technology and applications in agriculture," *Remote Sensing*, vol. 12, no. 16, p. 2659, Aug. 2020, doi: 10.3390/RS12162659.

[13] R. A. Viscarra Rossel, V. I. Adamchuk, K. A. Sudduth, N. J. McKenzie, and C. Lobsey, "Proximal Soil Sensing: An Effective Approach for Soil Measurements in Space and Time," in *Advances in Agronomy*, D. L. Sparks, Ed., in Advances in {Agronomy}, vol. 113. Academic Press, 2011, pp. 243–291. doi: 10.1016/B978-0-12-386473-4.00005-1.

[14] D. A. Robinson *et al.*, "Soil Moisture Measurement for Ecological and Hydrological Watershed-Scale Observatories: A Review," *Vadose Zone Journal*, vol. 7, no. 1, pp. 358–389, 2008, doi: 10.2136/vzj2007.0143.

[15] D. A. Robinson, S. B. Jones, J. M. Wraith, D. Or, and S. P. Friedman, "A Review of Advances in Dielectric and Electrical Conductivity Measurement in Soils Using Time Domain Reflectometry," *Vadose Zone Journal*, vol. 2, no. 4, pp. 444–475, Nov. 2003, doi: 10.2136/VZJ2003.4440.

[16] H. M. Jawad, R. Nordin, S. K. Gharghan, A. M. Jawad, and M. Ismail, "Energy-efficient wireless sensor networks for precision agriculture: A review," *Sensors (Switzerland)*, vol. 17, no. 8, p. 1781, Aug. 2017, doi: 10.3390/s17081781.

[17] T. Ojha, S. Misra, and N. S. Raghuwanshi, "Wireless sensor networks for agriculture: The state-of-the-art in practice and future challenges," *Computers and Electronics in*

*Agriculture*, vol. 118, pp. 66–84, Oct. 2015, doi: 10.1016/j.compag.2015.08.011.

[18]    S. A. Kumar and P. Ilango, "The Impact of Wireless Sensor Network in the Field of Precision Agriculture: A Review," *Wireless Personal Communications*, vol. 98, no. 1. Springer New York LLC, pp. 685–698, Jan. 01, 2018. doi: 10.1007/s11277-017-4890-z.

[19]    J. Lloret, S. Sendra, L. Garcia, and J. M. Jimenez, "A wireless sensor network deployment for soil moisture monitoring in precision agriculture," *Sensors*, vol. 21, no. 21, p. 7243, Oct. 2021, doi: 10.3390/s21217243.

[20]    U. Shafi, R. Mumtaz, J. García-Nieto, S. A. Hassan, S. A. R. Zaidi, and N. Iqbal, "Precision Agriculture Techniques and Practices: From Considerations to Applications," *Sensors 2019, Vol. 19, Page 3796*, vol. 19, no. 17, p. 3796, Sep. 2019, doi: 10.3390/S19173796.

[21]    H. Yin, Y. Cao, B. Marelli, X. Zeng, A. J. Mason, and C. Cao, "Soil Sensors and Plant Wearables for Smart and Precision Agriculture," *Advanced Materials*, vol. 33, no. 20, p. 2007764, May 2021, doi: 10.1002/ADMA.202007764.

[22]    B. D. Fuller and S. H. Ward, "Linear System Description of the Electrical Parameters of Rocks," *IEEE Transactions on Geoscience Electronics*, vol. 8, no. 1, pp. 7–18, 1970, doi: 10.1109/TGE.1970.271447.

[23]    M. A. Hatch *et al.*, "The importance of including conductivity and dielectric permittivity information when processing low-frequency GPR and high-frequency EMI data sets," *Journal of Applied Geophysics*, vol. 96, pp. 77–86, 2013, doi: 10.1016/j.jappgeo.2013.06.007.

[24]    J. C. Santamarina, A. Klein, and M. A. Fam, "Soils and waves:Particulate materials behavior, characterization and process monitoring," *Journal of Soils and Sediments*, vol. 1, no. 2, pp. 130–130, Jun. 2001, doi: 10.1007/bf02987719.

[25]    D. L. Corwin and S. M. Lesch, "Apparent soil electrical conductivity measurements in agriculture," *Computers and Electronics in Agriculture*, vol. 46, no. 1-3 SPEC. ISS., pp. 11–43, Mar. 2005, doi: 10.1016/j.compag.2004.10.005.

[26]    G. E. Archie, "The Electrical Resistivity Log as an Aid in Determining Some Reservoir Characteristics," *Transactions of the AIME*, vol. 146, no. 01, pp. 54–62, Dec. 1942, doi: 10.2118/942054-G.

[27]    A. E. Bussian, "Electrical conductance in a porous medium.," *Geophysics*, vol. 48, no.

9, pp. 1258–1268, 1983, doi: 10.1190/1.1441549.

[28]   G. C. Topp, J. L. Davis, and A. P. Annan, "Electromagnetic determination of soil water content: Measurements in coaxial transmission lines," *Water Resources Research*, vol. 16, no. 3, pp. 574–582, Jun. 1980, doi: 10.1029/WR016I003P00574.

[29]   D. P. Lesmes and S. P. Friedman, "Relationships between the Electrical and Hydrogeological Properties of Rocks and Soils," pp. 87–128, 2005, doi: 10.1007/1-4020-3102-5_4.

[30]   M. H. Loke, J. E. Chambers, D. F. Rucker, O. Kuras, and P. B. Wilkinson, "Recent developments in the direct-current geoelectrical imaging method," *Journal of Applied Geophysics*, vol. 95, pp. 135–156, Aug. 2013, doi: 10.1016/j.jappgeo.2013.02.017.

[31]   A. Samouëlian, I. Cousin, A. Tabbagh, A. Bruand, and G. Richard, "Electrical resistivity survey in soil science: a review," *Soil and Tillage Research*, vol. 83, no. 2, pp. 173–193, Sep. 2005, doi: 10.1016/j.still.2004.10.004.

[32]   V. M. Timofeev, A. W. Rogozinski, J. A. Hunter, and M. Douma, "A New Ground Resistivity Method for Engineering and Environmental Geophysics," in *Symposium on the Application of Geophysics to Engineering and Environmental Problems 1994*, Environment and Engineering Geophysical Society, Jan. 1994, pp. 701–715. doi: 10.4133/1.2922099.

[33]   O. Kuras, D. Beamish, P. I. Meldrum, and R. D. Ogilvy, "Fundamentals of the capacitive resistivity technique," *Geophysics*, vol. 71, no. 3, May 2006, doi: 10.1190/1.2194892.

[34]   R. Grard, "A quadrupolar array for measuring the complex permittivity of the ground: Application to Earth prospection and planetary exploration," *Measurement Science and Technology*, vol. 1, no. 3, pp. 295–301, 1990, doi: 10.1088/0957-0233/1/3/016.

[35]   O. Kuras, "The Capacitive Resistivity Technique for Electrical Imaging of the Shallow Subsurface," PhD thesis, 2002.

[36]   A. Tabbagh, S. Flageul, M. Abas, J. Thiesson, and F. Rejiba, "First in situ test of a new electrostatic resistivity meter," *Near Surface 2011 - 17th European Meeting of Environmental and Engineering Geophysics*. 2011. doi: 10.3997/2214-4609.20144370.

[37]   A. Przyklenk, A. Hördt, and T. Radić, "Capacitively coupled resistivity measurements to determine frequency-dependent electrical parameters in periglacial environment-theoretical considerations and first field tests," *Geophysical Journal International*, vol.

206, no. 2, pp. 1352–1365, Aug. 2016, doi: 10.1093/gji/ggw178.

[38] Z. Wang, S. Wang, G. Fang, and Q. Zhang, "Investigation on a Novel Capacitive Electrode for Geophysical Surveys," *Journal of Sensors*, vol. 2016. 2016. doi: 10.1155/2016/4209850.

[39] Q. Niu and Y. H. Wang, "Theoretical and experimental examinations of the capacitively coupled resistivity (line antenna) method," *Geophysics*, vol. 78, no. 4, pp. E189--E199, Jul. 2013, doi: 10.1190/GEO2012-0376.1.

[40] O. Kuras, D. Beamish, P. I. Meldrum, and R. D. Ogilvy, "Fundamentals of the capacitive resistivity technique," *https://doi.org/10.1190/1.2194892*, vol. 71, no. 3, May 2006, doi: 10.1190/1.2194892.

[41] J. L. DAVIS and A. P. ANNAN, "Ground-Penetrating Radar for High-Resolution Mapping of Soil and Rock Stratigraphy," *Geophysical Prospecting*, vol. 37, no. 5, pp. 531–551, Jul. 1989, doi: 10.1111/j.1365-2478.1989.tb02221.x.

[42] S. Pathirana, S. Lambot, M. Krishnapillai, M. Cheema, C. Smeaton, and L. Galagedara, "Ground-Penetrating Radar and Electromagnetic Induction: Challenges and Opportunities in Agriculture," *Remote Sensing*, vol. 15, no. 11, p. 2932, Jun. 2023, doi: 10.3390/rs15112932.

[43] A. Neal, "Ground-penetrating radar and its use in sedimentology: Principles, problems and progress," *Earth-Science Reviews*, vol. 66, no. 3–4, pp. 261–330, Aug. 2004, doi: 10.1016/j.earscirev.2004.01.004.

[44] A. Klotzsche, F. Jonard, M. C. Looms, J. van der Kruk, and J. A. Huisman, "Measuring Soil Water Content with Ground Penetrating Radar: A Decade of Progress," *Vadose Zone Journal*, vol. 17, no. 1, pp. 1–9, Jan. 2018, doi: 10.2136/vzj2018.03.0052.

[45] X. Liu, X. Dong, and D. I. Leskovar, "Ground penetrating radar for underground sensing in agriculture: A review," *International Agrophysics*, vol. 30, no. 4, pp. 533–543, Oct. 2016, doi: 10.1515/intag-2016-0010.

[46] H. M. Jol, "Ground Penetrating Radar Theory and Applications," *Ground Penetrating Radar Theory and Applications*, pp. 1–524, Dec. 2008, doi: 10.1016/b978-0-444-53348-7.x0001-4.

[47] F. Lombardi, B. Ortuani, A. Facchi, and M. Lualdi, "Assessing the Perspectives of Ground Penetrating Radar for Precision Farming," *Remote Sensing*, vol. 14, no. 23, p.

6066, Nov. 2022, doi: 10.3390/rs14236066.

[48] M. A. Hatch *et al.*, "The importance of including conductivity and dielectric permittivity information when processing low-frequency GPR and high-frequency EMI data sets," *Journal of Applied Geophysics*, vol. 96, pp. 77–86, 2013, doi: 10.1016/j.jappgeo.2013.06.007.

[49] J. A. Doolittle, F. E. Minzenmayer, S. W. Waltman, E. C. Benham, J. W. Tuttle, and S. D. Peaslee, "Ground-penetrating radar soil suitability map of the conterminous United States," *Geoderma*, vol. 141, no. 3–4, pp. 416–421, Oct. 2007, doi: 10.1016/j.geoderma.2007.05.015.

[50] K. Zajícová and T. Chuman, "Application of ground penetrating radar methods in soil studies: A review," *Geoderma*, vol. 343, pp. 116–129, Jun. 2019, doi: 10.1016/J.GEODERMA.2019.02.024.

[51] K. Heil and U. Schmidhalter, "The application of EM38: Determination of soil parameters, selection of soil sampling points and use in agriculture and archaeology," *Sensors (Switzerland)*, vol. 17, no. 11, Nov. 2017, doi: 10.3390/s17112540.

[52] ITU-R, "Nomenclature of the frequency and wavelengh bands used in telecommunications," Geneva, Switzerland, 2015. [Online]. Available: http://www.itu.int/ITU-R/go/patents/en

[53] J. D. McNeill, "Electromagnetic terrain conductivity measurement at low induction," 1980. Accessed: Jan. 25, 2022. [Online]. Available: http://www.geonics.com/html/technicalnotes.html

[54] A. TABBAGH, "What Is the Best Coil Orientation in the Slingram Electromagnetic Prospecting Method?," *Archaeometry*, vol. 28, no. 2, pp. 185–196, Aug. 1986, doi: 10.1111/j.1475-4754.1986.tb00386.x.

[55] J. D. McNeill, "Why Doesn't Geonics Limited Build a Muilti-Frequency EM31 or EM38?," 1996. http://www.geonics.com/html/technicalnotes.html (accessed Apr. 21, 2020).

[56] E. V. Balkov, D. I. Fadeev, Y. G. Karin, A. K. Manshtein, Y. A. Manshtein, and G. L. Panin, "A new approach to shallow-depth electromagnetic sounding," *Russian Geology and Geophysics*, vol. 58, no. 5, pp. 635–641, May 2017, doi: 10.1016/j.rgg.2017.04.004.

[57] E. Lück, R. Gebbers, J. Ruehlmann, and U. Spangenberg, "Electrical conductivity

mapping for precision farming," *Near Surface Geophysics*, vol. 7, no. 1, pp. 15–25, Feb. 2009, doi: 10.3997/1873-0604.2008031.

[58]   R. Gebbers, E. Lück, M. Dabas, and H. Domsch, "Comparison of instruments for geoelectrical soil mapping at the field scale," *Near Surface Geophysics*, vol. 7, no. 3, pp. 179–190, 2009, doi: 10.3997/1873-0604.2009011.

[59]   Geonics Limited Staff, "Geonics EM38-MK2 Ground Conductivity Meter," *Geonics Limited*. 2020. [Online]. Available: http://www.geonics.com/html/em38.html

[60]   "DUALEM." https://dualem.com/ (accessed Mar. 02, 2023).

[61]   I. J. Won, D. A. Keiswetter, G. R. A. Fields, and L. C. Sutton, "GEM-2: A New Multifrequency Electromagnetic Sensor," *Journal of Environmental and Engineering Geophysics*, vol. 1, no. 2, pp. 129–137, Aug. 1996, doi: 10.4133/jeeg1.2.129.

[62]   J. Guillemoteau and J. Tronicke, "Non-standard electromagnetic induction sensor configurations: Evaluating sensitivities and applicability," *Journal of Applied Geophysics*, vol. 118, pp. 15–23, 2015, doi: 10.1016/j.jappgeo.2015.04.008.

[63]   Y. A. Manstein, A. K. Manstein, E. Balkov, G. Panin, and A. Scozzari, "Non-invasive measurements for shallow depth soil exploration: Development and application of an electromagnetic induction instrument," in *Conference Record - IEEE Instrumentation and Measurement Technology Conference*, May 2015, pp. 1395–1399. doi: 10.1109/I2MTC.2015.7151479.

[64]   H. Huang and I. J. Won, "Real-time resistivity sounding using a hand-held broadband electromagnetic sensor," *Geophysics*, vol. 68, no. 4, pp. 1224–1231, Jul. 2003, doi: 10.1190/1.1598114.

[65]   D. Vasić, D. Ambruš, and V. Bilas, "Simple linear inversion of soil electromagnetic properties from analytical model of electromagnetic induction sensor," in *2014 IEEE Sensors Applications Symposium, SAS 2014 - Proceedings*, Feb. 2014, pp. 15–19. doi: 10.1109/SAS.2014.6798908.

[66]   D. Vasic, D. Ambrus, and V. Bilas, "Stochastic inversion of two-layer soil model parameters from electromagnetic induction data," in *SAS 2015 - 2015 IEEE Sensors Applications Symposium, Proceedings*, Apr. 2015, pp. 1–5. doi: 10.1109/SAS.2015.7133603.

[67]   J. Macnae and C. Adams, "Near-surface resistivity contrast mapping with a capacitive

sensor array and an inductive source," *Geophysics*, vol. 76, no. 2, pp. G13--G23, Mar. 2011, doi: 10.1190/1.3553480.

[68] H. Huang and D. C. Fraser, "Dielectric permittivity and resistivity mapping using high-frequency, helicopter-borne EM data," *Geophysics*, vol. 67, no. 3, pp. 727–738, 2002, doi: 10.1190/1.1484515.

[69] H. Huang and D. C. Fraser, "Mapping of the resistivity, susceptibility, and permittivity of the earth using a helicopter-borne electromagnetic system," *Geophysics*, vol. 66, no. 1, pp. 148–157, Jan. 2001, doi: 10.1190/1.1444889.

[70] J. H. Moran and K. S. Kunz, "BASIC THEORY OF INDUCTION LOGGING AND APPLICATION TO STUDY OF TWO-COIL SONDES," *GEOPHYSICS*, vol. 27, no. 6, pp. 829–858, Dec. 1962, doi: 10.1190/1.1439108.

[71] C. J. Weiss and G. A. Newman, "Electromagnetic induction in a fully 3-D anisotropic earth," *GEOPHYSICS*, vol. 67, no. 4, pp. 1104–1114, Jul. 2002, doi: 10.1190/1.1500371.

[72] D. C. Stewart, W. L. Anderson, T. P. Grover, and V. F. Labson, "Shallow subsurface mapping by electromagnetic sounding in the 300 kHz to 30 MHz range: model studies and prototype system assessment," *Geophysics*, vol. 59, no. 8, pp. 1201–1210, Aug. 1994, doi: 10.1190/1.1443678.

[73] A. TABBAGH, "Simultaneous Measurement of Electrical Conductivity and Dielectric Permittivity of Soils Using a Slingram Electromagnetic Device in Medium Frequency Range," *Archaeometry*, vol. 36, no. 1, pp. 159–170, Feb. 1994, doi: 10.1111/j.1475-4754.1994.tb01071.x.

[74] J. B. Sigman *et al.*, "High-Frequency Electromagnetic Induction Sensing of Nonmetallic Materials," *IEEE Transactions on Geoscience and Remote Sensing*, vol. 55, no. 9, pp. 5254–5263, Sep. 2017, doi: 10.1109/TGRS.2017.2704102.

[75] A. J. Peyton, "Electromagnetic induction tomography," in *Industrial Tomography: Systems and Applications*, Elsevier Inc., 2015, pp. 61–107. doi: 10.1016/B978-1-78242-118-4.00003-4.

[76] Z. Zakaria *et al.*, "Advancements in transmitters and sensors for biological tissue imaging in Magnetic Induction Tomography," *Sensors (Switzerland)*, vol. 12, no. 6, pp. 7126–7156, May 2012, doi: 10.3390/s120607126.

[77] D. Stewart, W. L. Anderson, T. P. Grover, and V. F. Labson, "New instrument and

inversion program for near-surface mapping: High-frequency EM sounding and profiling in the frequency range 300 kHz to 30 MHz," *1990 SEG Annual Meeting*, pp. 410–413, 1990, doi: 10.1190/1.1890215.

[78] P. Kessouri, S. Flageul, Q. Vitale, S. Buvat, F. Rejiba, and A. Tabbagh, "Medium-frequency electromagnetic device to measure electric conductivity and dielectric permittivity of soils," *Geophysics*, vol. 81, no. 1, pp. E1–E16, 2016, doi: 10.1190/GEO2014-0468.1.

[79] W. Frangos, A. Becker, and K. H. Lee, "High-frequency and very-high-frequency (HF & VHF) above-ground electromagnetic impedance measurements," *Journal of Environmental and Engineering Geophysics*, vol. 9, no. 2, Apr. 2004, doi: 10.4133/jeeg9.2.87.

[80] G. Beziuk, "Near surface geophysical surveys with a high frequency mutual impedance measuring system," *Acta Geophysica*, vol. 60, no. 1, pp. 140–156, Feb. 2012, doi: 10.2478/s11600-011-0064-7.

[81] D. R. Glaser, F. Shubitidze, and B. E. Barrowes, "Standoff High-Frequency Electromagnetic Induction Response of Unsaturated Sands: A Tank-Scale Feasibility Study," *Journal of Environmental and Engineering Geophysics*, vol. 27, no. 1, pp. 45–51, Apr. 2022, doi: 10.32389/JEEG21-030.

[82] D. R. Glaser, B. E. Barrowes, F. Shubitidze, and L. D. Slater, "Laboratory investigation of high-frequency electromagnetic induction measurements for macro-scale relaxation signatures," *Geophysical Journal International*, vol. 235, no. 2, pp. 1274–1291, Jul. 2023, doi: 10.1093/gji/ggad298.

[83] D. Goss, R. O. Mackin, E. Crescenzo, H. S. Tapp, and A. J. Peyton, "Understanding the coupling mechanisms in high frequency EMT," in *3rd World Congress on Industrial Process Tomography*, International Society for Industrial Process Tomography, 2003, pp. 364–369.

[84] D. Ambruš, D. Vasić, and V. Bilas, "Automatic compensation of primary field coupling for a frequency-domain electromagnetic induction sensor," in *2017 {IEEE} {International} {Instrumentation} and {Measurement} {Technology} {Conference} ({I}2MTC)*, May 2017, pp. 1–5. doi: 10.1109/I2MTC.2017.7969872.

[85] O. Kuras, "The Capacitive Resistivity Technique for Electrical Imaging of the shallow

subsurface," PhD thesis, 2002.

[86]  S. Flageul, M. Dabas, J. Thiesson, F. Rejiba, and A. Tabbagh, "First in situ tests of a new electrostatic resistivity meter," *Near Surface Geophysics*, vol. 11, no. 3, pp. 265–273, Jun. 2013, doi: 10.3997/1873-0604.2012063.

[87]  J. D. Jackson, *Classical Electrodynamics, 3rd Edition*. 1998.

[88]  T. P. Theodoulidis and E. E. Kriezis, *Eddy current canonical problems (with applications to nondestructive evaluation)*. Duluth, Georgia: Tech Science Press, 2006.

[89]  B. A. Auld and J. C. Moulder, "Review of advances in quantitative eddy current nondestructive evaluation," *Journal of Nondestructive Evaluation*, vol. 18, no. 1, pp. 3–36, Mar. 1999, doi: 10.1023/A:1021898520626/METRICS.

[90]  P. P. Silvester and D. Omeragic, "Sensitivity maps for metal detector design," *IEEE Transactions on Geoscience and Remote Sensing*, vol. 34, no. 3, pp. 788–792, May 1996, doi: 10.1109/36.499783.

[91]  J. D. McNeill, "Electromagnetic terrain conductivity measurement at low induction," 1980. http://www.geonics.com/html/technicalnotes.html (accessed Jan. 25, 2022).

[92]  "CST Studio Suite 3D EM simulation and analysis software." https://www.3ds.com/products-services/simulia/products/cst-studio-suite/ (accessed Jan. 25, 2022).

[93]  K. A. Sudduth, S. T. Drummond, and N. R. Kitchen, "Accuracy issues in electromagnetic induction sensing of soil electrical conductivity for precision agriculture," *Computers and Electronics in Agriculture*, vol. 31, no. 3, pp. 239–264, May 2001, doi: 10.1016/S0168-1699(00)00185-X.

[94]  D. A. Robinson, I. Lebron, S. M. Lesch, and P. Shouse, "Minimizing Drift in Electrical Conductivity Measurements in High Temperature Environments using the EM-38," *Soil Science Society of America Journal*, vol. 68, no. 2, pp. 339–345, Mar. 2004, doi: 10.2136/sssaj2004.3390.

[95]  D. Beamish, "Low induction number, ground conductivity meters: A correction procedure in the absence of magnetic effects," *Journal of Applied Geophysics*, vol. 75, no. 2, pp. 244–253, Oct. 2011, doi: 10.1016/j.jappgeo.2011.07.005.

[96]  A. S. Mat Su and V. I. Adamchuk, "Temporal and operation-induced instability of

apparent soil electrical conductivity measurements," *Frontiers in Soil Science*, vol. 3, p. 1137731, Apr. 2023, doi: 10.3389/fsoil.2023.1137731.

[97] M. Tazifor Tchantcho, E. Zimmermann, J. A. Huisman, M. Dick, A. Mester, and S. van Waasen, "Low-Pass Filters for a Temperature Drift Correction Method for Electromagnetic Induction Systems," *Sensors (Basel, Switzerland)*, vol. 23, no. 17, Sep. 2023, doi: 10.3390/s23177322.

[98] K. Heil and U. Schmidhalter, "Theory and guidelines for the application of the geophysical sensor em38," *Sensors (Switzerland)*, vol. 19, no. 19, p. 4293, Oct. 2019, doi: 10.3390/s19194293.

[99] E. R. Morris, "Height-above-ground effects on penetration depth and response of electromagnetic induction soil conductivity meters," *Computers and Electronics in Agriculture*, vol. 68, no. 2, pp. 150–156, Oct. 2009, doi: 10.1016/j.compag.2009.05.009.

[100] J. McNeill and M. Bosnar, "Application of dipole–dipole electromagnetic systems for geological depth sounding," 1999.

[101] A. Korsaeth, "Height above ground corrections of EM38 readings of soil apparent electrical conductivity," *Acta Agriculturae Scandinavica Section B: Soil and Plant Science*, vol. 56, no. 4, pp. 333–336, Dec. 2006, doi: 10.1080/09064710500325855.

[102] X. Tan *et al.*, "Simultaneous calibration and inversion algorithm for multiconfiguration electromagnetic induction data acquired at multiple elevations," *Geophysics*, vol. 84, no. 1, pp. EN1–EN14, Dec. 2019, doi: 10.1190/geo2018-0264.1.

[103] M. Tazifor Tchantcho, E. Zimmermann, J. A. Huisman, M. Dick, A. Mester, and S. van Waasen, "Low-Pass Filters for a Temperature Drift Correction Method for Electromagnetic Induction Systems," *Sensors (Basel, Switzerland)*, vol. 23, no. 17, p. 7322, Aug. 2023, doi: 10.3390/s23177322.

[104] A. Mester, E. Zimmermann, J. Van Der Kruk, H. Vereecken, and S. Van Waasen, "Development and drift-analysis of a modular electromagnetic induction system for shallow ground conductivity measurements," *Measurement Science and Technology*, vol. 25, no. 5, p. 055801, Apr. 2014, doi: 10.1088/0957-0233/25/5/055801.

[105] V. R. N. dos Santos and J. L. Porsani, "Comparing performance of instrumental drift correction by linear and quadratic adjusting in inductive electromagnetic data," *Journal of Applied Geophysics*, vol. 73, no. 1, pp. 1–7, Jan. 2011, doi:

10.1016/j.jappgeo.2010.10.004.

[106] R. Ma, A. McBratney, B. Whelan, B. Minasny, and M. Short, "Comparing temperature correction models for soil electrical conductivity measurement," *Precision Agriculture*, vol. 12, no. 1, pp. 55–66, Feb. 2011, doi: 10.1007/s11119-009-9156-7.

[107] P. De Smedt, S. Delefortrie, and F. Wyffels, "Identifying and removing micro-drift in ground-based electromagnetic induction data," *Journal of Applied Geophysics*, vol. 131, pp. 14–22, Aug. 2016, doi: 10.1016/j.jappgeo.2016.05.004.

[108] M. Tazifor, E. Zimmermann, J. A. Huisman, M. Dick, A. Mester, and S. Van Waasen, "Model-Based Correction of Temperature-Dependent Measurement Errors in Frequency Domain Electromagnetic Induction (FDEMI) Systems," *Sensors 2022, Vol. 22, Page 3882*, vol. 22, no. 10, p. 3882, May 2022, doi: 10.3390/S22103882.

[109] R. C. McKenzie, W. Chomistek, and N. F. Clark, "Conversion of electromagnetic inductance readings to saturated paste extract values in soils for different temperature, texture, and moisture conditions," *Canadian Journal of Soil Science*, vol. 69, no. 1, pp. 25–32, 1989, doi: 10.4141/cjss89-003.

[110] E. C. Brevik, T. E. Fenton, and R. Horton, "Effect of daily soil temperature fluctuations on soil electrical conductivity as measured with the Geonics® EM-38," *Precision Agriculture*, vol. 5, no. 2, pp. 145–152, Apr. 2004, doi: 10.1023/B:PRAG.0000022359.79184.92.

[111] J. Huang, B. Minasny, B. M. Whelan, A. B. McBratney, and J. Triantafilis, "Temperature-dependent hysteresis effects on EM induction instruments: An example of single-frequency multi-coil array instruments," *Computers and Electronics in Agriculture*, vol. 132, pp. 76–85, Jan. 2017, doi: 10.1016/j.compag.2016.11.013.

[112] B. J. Minsley, B. D. Smith, R. Hammack, J. I. Sams, and G. Veloski, "Calibration and filtering strategies for frequency domain electromagnetic data," *Journal of Applied Geophysics*, vol. 80, pp. 56–66, May 2012, doi: 10.1016/j.jappgeo.2012.01.008.

[113] S. Delefortrie, P. De Smedt, T. Saey, E. Van De Vijver, and M. Van Meirvenne, "An efficient calibration procedure for correction of drift in EMI survey data," *Journal of Applied Geophysics*, vol. 110, pp. 115–125, Nov. 2014, doi: 10.1016/j.jappgeo.2014.09.004.

[114] H. Abdu, D. A. Robinson, and S. B. Jones, "Comparing Bulk Soil Electrical Conductivity

Determination Using the DUALEM-1S and EM38-DD Electromagnetic Induction Instruments," *Soil Science Society of America Journal*, vol. 71, no. 1, pp. 189–196, Jan. 2007, doi: 10.2136/sssaj2005.0394.

[115] A. Besson, I. Cousin, A. Dorigny, M. Dabas, and D. King, "The temperature correction for the electrical resistivity measurements in undisturbed soil samples: Analysis of the existing conversion models and proposal of a new model," *Soil Science*, vol. 173, no. 10, pp. 707–720, Oct. 2008, doi: 10.1097/SS.0b013e318189397f.

[116] J. D. D. Rhoades, F. Chanduvi, and S. Lesch, "Soil salinity assessment. Methods and interpretation of electrical conductivity measurements. FAO Irrigation and Drainage paper 57," *FAO Irrigation and Drainage Paper*, p., 1999.

[117] M. K. Kazimierczuk, "High-Frequency Magnetic Components: Second Edition," *High-Frequency Magnetic Components: Second Edition*, pp. 1–729, Nov. 2013, doi: 10.1002/9781118717806.

[118] W. Boyes, *Instrumentation Reference Book*. 2010. doi: 10.1016/C2009-0-25186-5.

[119] H. Griffiths, W. Gough, S. Watson, and R. J. Williams, "Residual capacitive coupling and the measurement of permittivity in magnetic induction tomography," *Physiological Measurement*, vol. 28, no. 7, Jul. 2007, doi: 10.1088/0967-3334/28/7/S23.

[120] H. Y. Wei and A. J. Wilkinson, "Design of a sensor coil and measurement electronics for magnetic induction tomography," *IEEE Transactions on Instrumentation and Measurement*, vol. 60, no. 12, pp. 3853–3859, Dec. 2011, doi: 10.1109/TIM.2011.2147590.

[121] C. H. Riedel, M. Keppelen, S. Nani, and O. Dössel, "Capacitive effects and shielding in magnetic induction conductivity measurement," *Biomedizinische Technik*, vol. 48, no. s1, pp. 330–331, Oct. 2003, doi: 10.1515/bmte.2003.48.s1.330.

[122] M. D. O'Toole, L. A. Marsh, J. L. Davidson, Y. M. Tan, D. W. Armitage, and A. J. Peyton, "Non-contact multi-frequency magnetic induction spectroscopy system for industrial-scale bio-impedance measurement," *Measurement Science and Technology*, vol. 26, no. 3, p. 035102, Feb. 2015, doi: 10.1088/0957-0233/26/3/035102.

[123] C. G. Malmberg and A. A. Maryott, "Dielectric constants of aqueous solutions of dextrose and sucrose," *Journal of Research of the National Bureau of Standards*, vol. 45, no. 4, p. 299, 1950, doi: 10.6028/jres.045.030.

# Abbreviations

| | |
|---|---|
| **PSS** | Proximal Soil Sensing |
| **TDR** | Time-domain reflectometry |
| **WSN** | Wireless Sensor Network |
| **DC** | Direct Current |
| **AC** | Alternating Current |
| **ECa** | Apparent Electrical Conductivity |
| **GPR** | Ground Penetrating Radar |
| **CCR** | Capacitively Coupled Resistivity |
| **EMI** | Electromagnetic Induction |
| **VWC** | Volume Water Content |
| **LFEMI** | Low-Frequency Electromagnetic Induction |
| **TX** | Transmitter |
| **RX** | Receiver |
| **HFEMI** | High-Frequency Electromagnetic Induction |
| **DCR** | Direct Current Resistivity |
| **FEM** | Finite Element Method |
| **VNA** | Vector Network Analyzer |
| **PCB** | Printed Circuit Board |

# List of Figures

# List of tables

# Biography

**Dorijan Špikić** was born on December 31st, 1992, in Koprivnica, Croatia. He received his bachelor's and master's degrees in electrical engineering and information technology (electronic and computer engineering) in 2015 and 2017, respectively, from the University of Zagreb Faculty of Electrical Engineering and Computing.

He enrolled in a postgraduate study at the Faculty of Electrical Engineering and Computing in March 2018. He has been a teaching and research associate with the Department of Electronic Systems and Information Processing of the same Faculty since November 2017. He participated in the scientific project "PERUN - Enabling Inductive Metal Characterisation in Non-cooperative Soils" from November 2017 to March 2018. He was a research and teaching assistant in a project "MIMES – Models and Inverse Methods for Near Field Electromagnetic Sensors," funded by the Croatian Science Foundation, from March 2018 to August 2022. He was a senior researcher in the industrial research and innovation IRI project "SmartEC – Diagnostic system for eddy current testing" from November 2022 to August 2023. He is currently a senior researcher on a project "EMISArray – Novel EMI Sensor Arrays for Rapid Standoff Detection of Buried Explosive Hazards."

His professional and research activities include eddy current testing, electromagnetic induction soil sensing, electronic instrumentation, sensor systems, and embedded systems. He co-authors several journal and international conference papers in the mentioned research areas.

Dorijan Špikić is a member of the professional society IEEE Instrumentation and Measurement. He was a reviewer for the journals MDPI Sensors and Automatika and international conferences IEEE I2MTC. He is a teaching assistant in the Electrical Circuits, Electronics Systems, and Electronic Instrumentation courses, and he has supervised several bachelor's and master's theses at FER.

# List of publications

## Journal articles and review articles in CC journals

[1] **Špikić, Dorijan**; Švraka, Matija; Vasić, Darko. Effectiveness of electrostatic shielding in high-frequency electromagnetic induction soil sensing. // Sensors, 22 (2022), 8; 3000, 16 doi:10.3390/s22083000.

[2] Vasić, Darko; Rep, Ivan; **Špikić, Dorijan**; Kekelj, Matija. Model of Magnetically Shielded Ferrite-Cored Eddy Current Sensor. // Sensors, 22 (2022), 1;326, 20 doi:10.3390/s22010326.

## Scientific conference papers with international peer-review

[1] **Dorijan Špikić**, Matija Švraka and Darko Vasić, "Electromagnetic Induction Sensing of Soil Dielectric Permittivity and Electrical Conductivity from 10 MHz to 30 MHz," *2023 IEEE International Instrumentation and Measurement Technology Conference (I2MTC)*, Kuala Lumpur, Malaysia, 2023, pp. 1-5, doi: 10.1109/I2MTC53148.2023.10176087.

[2] **Dorijan Špikić**, Matija Švraka and Darko Vasić, "Contactless Sensing of Soil Electrical Conductivity Using High Frequency Electromagnetic Induction," *2022 IEEE Sensors*, Dallas, TX, USA, 2022, pp. 1-4, doi: 10.1109/SENSORS52175.2022.9967093.

[3] Ivan Rep, **Dorijan Špikić** and Darko Vasić, "Eddy Current Inversion of Lift-off, Conductivity and Permeability Relaxation," *2021 44th International Convention on Information, Communication and Electronic Technology (MIPRO)*, Opatija, Croatia, 2021, pp. 136-140, doi: 10.23919/MIPRO52101.2021.9597156.

[4] **Dorijan Špikić**, Darko Vasić, Davorin Ambruš, Ivan Rep and Vedran Bilas, "Towards high frequency electromagnetic induction sensing of soil apparent electrical conductivity," *2020 IEEE International Instrumentation and Measurement Technology Conference (I2MTC)*, Dubrovnik, Croatia, 2020, pp. 1-5, doi: 10.1109/I2MTC43012.2020.9128693

[5] **Dorijan Špikić**, Robert Tutić, Darko Vasić, Davorin Ambruš and Vedran Bilas, "Digital Eddy Current Probe for Tube Nondestructive Testing Using Binary Excitation," *2019 IEEE International Instrumentation and Measurement Technology Conference (I2MTC)*, Auckland, New Zealand, 2019, pp. 1-5, doi: 10.1109/I2MTC.2019.8827152.

[6] Ivana Čuljak, Davorin Ambruš, Marko Marušić, **Dorijan Špikić**, Darko Vasić and Vedran Bilas, "Eddy current probe for inspection of steel tubes based on rotating field principle," *2018 IEEE International Instrumentation and Measurement Technology Conference (I2MTC)*, Houston, TX, USA, 2018, pp. 1-6, doi: 10.1109/I2MTC.2018.8409601.

[7] Davorin. Ambruš, **Dorijan Špikić**, Darko Vasić and Vedran Bilas, "Sensitivity profile of compact inductive sensor for apparent electrical conductivity of topsoil," *2017 IEEE SENSORS*, Glasgow, UK, 2017, pp. 1-3, doi: 10.1109/ICSENS.2017.8234037.

# Životopis

**Dorijan Špikić** rođen je 31. prosinca 1992. u Koprivnici, Hrvatska. Diplomirao je i magistrirao elektrotehniku i informacijske tehnologije (elektroničko i računalno inženjerstvo) 2015. odnosno 2017. godine na Fakultetu elektrotehnike i računarstva Sveučilišta u Zagrebu.

Poslijediplomski studij na Fakultetu elektrotehnike i računarstva upisao je u ožujku 2018. Od studenog 2017. je asistent na Zavodu za elektroničke sustave i obradbu informacija istog Fakulteta. Sudjelovao je u znanstvenom projektu " PERUN - Enabling Inductive Metal Characterisation in Non-cooperative Soils. " od studenog 2017. do ožujka 2018. Bio je asistent na projektu "MIMES – Modeli i inverzne metode za elektromagnetske senzore u bliskom polju " financiran od Hrvatske zaklade za znanost, od ožujka 2018. do kolovoza 2022. Radio je kao iskusni istraživač na IRI projektu „SmartEC – Dijagnostički sustav za ispitivanje metodom vrtložnih struja" od studenog 2022. do kolovoza 2023. Trenutno radi kao iskusni istraživač na projektu "EMISarray – Napredni nizovi elektromagnetskih induktivnih senzora za brzu detekciju ukopanih eksplozivnih objekata sa sigurne udaljenosti."

Njegove stručne i istraživačke aktivnosti uključuju ispitivanje vrtložnim strujama, ispitivanje tla elektromagnetskom indukcijom, elektroničku instrumentaciju, senzorske sustave i ugradbene računalne sustave. Koautor je više radova u časopisima i međunarodnih skupova iz navedenih područja istraživanja.

Dorijan Špikić član je stručnog društva IEEE. Bio je recenzent za časopise MDPI Sensors i Automatika te međunarodne konferencije IEEE Instrumentation and Measurement. Asistent je na kolegijima Električni krugovi, Elektronički sustavi i Elektronička instrumentacija, a neposredno je mentorirao nekoliko završnih i diplomskih radova na FER-u.